TEMPERATE LAKES ON TITAN

A Dissertation

Presented in Partial Fulfillment of the Requirements for the

Degree Doctorate of Philosophy

with a

Major in Physics

in the

College of Graduate Studies

University of Idaho

by

Graham D. Vixie

May 2014

Major Professor: Jason Barnes, Ph.D.

AUTHORIZATION TO SUBMIT DISSERTATION

This dissertation of Graham Vixie, submitted for the degree of Doctorate of Philosophy with a Major in Physics and titled "Temperate Lakes on Titan," has been reviewed in final form. Permission, as indicated by the signatures and dates given below, is now granted to submit final copies to the College of Graduate Studies for approval.

Major Professor _____Date_____
Jason Barnes, Ph.D.

Committee Members _____Date_____
Simon Kattenhorn, Ph.D.

_____Date_____
Gwen Barnes, Ph.D.

_____Date_____
F. Marty Ytreberg, Ph.D.

_____Date_____
David Atkinson, Ph.D.

Department Administrator _____Date_____
Dave McIlroy, Ph.D.

Discipline's College Dean _____Date_____
Paul Joyce, Ph.D.

Final Approval and Acceptance by the College of Graduate Studies

_____Date_____
Jie Chen, Ph.D.

Abstract

For my Ph.D. dissertation, I investigate the relationship between lakes and climate on Titan. I first view Titan's surface at the visible wavelengths of the VIMS-VIS instrument and find two new atmospheric windows at 653 and 681 nm. Following up on observations of clouds around the 40°S latitude band, I surveyed the southern temperate latitudes finding two lake features. The total estimated volume of the larger of these lakes, Sionascaig Lacus, falls within the estimates of methane inventory in the clouds observed over this region. A survey of the northern mid-latitudes reveals three candidate features I reason to be lakes and would serve as interesting targets for future *Cassini* flybys. The existence of temperate lakes and lake candidates adds further constraints to Titan GCMs and adds to the complexity of Titan's polar lake asymmetry.

Acknowledgements

I would like to thank several people who helped on my journey to a Ph.D..

First I'd like to thank my parents, Doug and Marcy Vixie, for their unwavering support, showing me the importance of science, and matching my curiosity in all of my studies.

I'd like to thank my undergraduate professors Dr. Frederic Liebrand, Dr. Tom Ekkens, Dr. Tim Tiffin, and Dr. Jim Klein for encouraging my interests in physics, mathematics, and computer science. Thanks to my advisor Dr. Jason Barnes, for getting me involved with planetary science and guiding me into research and also to Dr. Simon Kattenhorn for his geologic influence.

My fellow grads and classmates: Casey Cook, Shannon MacKenzie, Alex Patthoff, Emily Martin, Matt Pendleton, Takashi Sasaki, Johnathon Ahlers, Jacob Turner, Ryan Souza, Paul Wilson, Brandon Fetroe, Jason Damazo, Jeffrey Hanson, Paul Lingas, Eric Brown, Stephanie Hatten, Andrea Hawkins-Daruud, and John Foster.

I'd also like to thank my friends for helping me along this path: Craig Saxby, Emily Ashley, Matt Chiang, David Anning, Philip Yang, Josephine Vo, and Thomas Wilson.

Dedication

To My Parents

Table of Contents

List of Tables

List of Figures

Chapter 1

Introduction

Dutch astronomer Christaan Huygens discovered Titan, the largest moon of Saturn, in 1655 following the discovery of the four largest Jovian satellites (Huygens, 1655). Giovanni Cassini published his findings of four more Saturnian satellites, giving them the labels Saturn I - V with Titan being Saturn IV. With the discoveries of additional moons, the numbering became dynamic to order each body by distance from Saturn. The modern names for the first discovered moons came from John Herschel in 1847. Cassini and Huygens would later lend their names to a joint National Aeronautics and Space Administration (NASA), European Space Agency (ESA), and Agenzia Spaziale Italiana (ASI) mission to the Saturnian system involving 126 flybys of Titan.

1.1 *Voyager* and *Hubble*

Voyager 1 in 1980 and *Voyager* 2 in 1981 each flew by Titan, *Voyager* 1 much closer, only to find a thick atmosphere obscuring the surface. Images from these spacecraft showed Titan's limb and haze being illuminated by the sun which, with radio occultation measurements revealing a nitrogen and methane atmosphere, temperature and pressure estimates, and mass constraints (Tyler et al., 1981), provided an argument for hydrocarbon seas. From these findings, Sagan & Dermott (1982) proposed a global ocean on Titan with depths in excess of 400m that could be detected by radar while others proposed the ocean's composition to be methane (Flasar, 1983) or ethane (Lunine et al., 1983).

The *Voyager* observation of methane in Titan's atmosphere combined with hydrocarbon seas were key to the hypothesis that Titan underwent a methane cycle analogous to Earth's hydrological cycle (Tyler et al., 1981; Lunine et al., 1983; Flasar, 1983; Eshleman et al., 1983; Toon et al., 1988). However, clouds were not detected until after *Voyager* with Earth-based telescopes utilizing adaptive optics which remove difficulties presented

by Earth's atmosphere (Griffith et al., 1998). The first clouds on Titan appeared at both low elevation and high southern latitude and were thought to be composed of methane (Thompson & Sagan, 1984; Griffith et al., 1998).

In 1995 the Hubble Space Telescope (HST) took a look at Titan in the near-IR at 940nm and 1080nm at a resolution of 295 km/pixel (Smith et al., 1996). HST detected definite albedo differences and possible variety in topography, which were first interpreted as possible continents and oceans following Sagan & Dermott (1982). However, Dermott & Sagan (1995) cited Titan's high orbital eccentricity as evidence for the hydrocarbon seas to be regional rather than global, otherwise Titan's orbit would be more circular. HST also identified Xanadu, the brightest albedo feature on Titan, in the equatorial region in addition to further strengthening the claim of liquid methane on the surface (Smith et al., 1996). Slight albedo variations were also observed from *Voyager* 1 data much later in retrospect (Richardson et al., 2004).

Clouds on Titan were thought to form by insolation on the summer hemisphere (Brown et al., 2002). Just prior to the arrival of *Cassini* in the Saturn system, Titan was closest to the summer solstice in the southern hemisphere. However, observations by Roe et al. (2002) revealed temperate latitude clouds around 40°S latitude, where before all clouds had been poleward of 70°S. The unexpected restriction to the 40°S band suggested either surficial control of cloud systems or seasonally dependent circulation. Surface features controlling the climate at this latitude band would require hydrocarbon lakes or outgassing events from cryovolcanoes (Roe et al., 2005b); however, none of the latter have been found to date. On the other hand, a seasonal dependence should show clouds near the north pole and presumably around 40°N moving into northern summer. Saturn, and by proxy Titan, revolves around the Sun about every 28 years, making understanding the effects of seasonal change a very long term goal.

1.2 *Cassini-Huygens*

The *Cassini-Huygens* spacecraft launched from Cape Canaveral in 1997 embarking on a seven-year voyage to Saturn. Two of the *Cassini-Huygens* mission objectives were to monitor Titan's atmosphere and any cloud movement and to characterize the surface following up on *Voyager* I and II, HST, and Earth-based observations.

Cassini uses instruments such as the Visual and Infrared Mapping Spectrometer (VIMS), a Synthetic Aperture RADAR (SAR), and the Imaging Science Subsystem (ISS) to achieve these goals. The year after arriving in the Saturn system, the *Huygens* probe descended onto Titan's surface, taking several atmospheric measurements and images on the way. The Descent Imager/Spectral Radiometer (DISR) resolved several elevated features, dark channels, and dune fields before landing (Tomasko et al., 2005). The *Huygens* landing made Titan the fourth ever extraterrestrial body with an imaged surface (after our Moon, Mars, and Venus), one of two moons to have a lander (after our own), and the farthest body from Earth to have a probe land on the surface.

The VIMS instrument has two cameras: a slit-scanning camera covering the visible wavelengths and a spot-scanning camera covering the near- and mid-infrared covering a range of 350-5100 nm (Brown et al., 2004). VIMS measures scattered, reflected, and emitted radiation from the atmosphere and surface of Titan and returns 352 wavelength channels over its wavelength range to help determine composition and surface structure. VIMS is especially useful for monitoring clouds and cloud systems as well as discriminating between surface chemical substrates.

SAR is a remote sensing instrument that sends out radio signals and produces scatterometry maps by timing and Doppler shift the return of the signal (Elachi et al., 2004). As the spacecraft flies over an area, RADAR scans to the sides where the signal is scattered back by a roughened surface. A shorter return time of a signal means the point of scatter is closer to the RADAR. A brighter signature on the map results from more return signal. SAR's 2.18 cm wavelength penetrates Titan's haze to get clear surface returns and can

achieve resolutions up to 200 m/pixel. A smooth surface, such the predicted hydrocarbon seas, would appear very dark due to the signal reflecting off of the surface or the depth of liquid attenuating the signal. In each case the signal does not return.

ISS has wide-angle and narrow-angle cameras, for taking pictures in a variation of detail, each with spectral filters covering visible and UV wavelengths (Porco et al., 2004). For Titan, ISS primarily uses the 938 nm methane window to image the surface.

DISR took image swaths through a fish-eye CCD to cover the Titan landscape aided by the rotation of the *Huygens* descent (Tomasko et al., 2002). The spectral radiometer covered the visible and near-IR wavelengths and measured the up and downward flux from 145 km to the surface.

From the earlier predictions of hydrocarbon seas, solar specular reflections should be simple to detect. Upon arrival, however, *Cassini* found none in the first flybys (Fussner, 2006). The ISS returned an image of an anomalous dark spot near the south pole of Titan in 2005 postulated to be lacustrine in nature. In 2006, SAR recorded a swath near the north pole identifying several liquid methane filled lakes, making Titan the only body other than Earth to have standing surface liquid (Stofan et al., 2006, 2007). A dark area in RADAR indicates a smooth area (i.e. specular reflection away from the receiver) or signal attenuation. In the case of the north polar dark spots, Stofan et al. (2007) suspected liquid due to the predicted existence of liquid hydrocarbons (Lorenz & Lunine, 2005; Elachi et al., 2005) and Global Circulation Models (GCMs) predicting the poles to be saturated with such a liquid (Rannou et al., 2006) combined with the interpretation that part of the RADAR signal had been reflected away from the spacecraft by the mirror-like liquid surface. Alternatively, the dark areas could be an organic layer covering the surface or a feature sloped away from the SAR look direction. SAR pictures of Earth's oceans show waves and turbulent structure, rather than observing the ocean floor, due in part to H_2O being highly absorbing at RADAR wavelengths. These lakes on Titan, however, showed no roughness at first, and thus appear black in the swath (Figure 1.1).

Cassini also contributed to the cloud monitoring campaign finding more clouds at the south pole on first arrival in 2004 (Figure 1.2). Shortly after Titan equinox in 2009, *Cassini* did not detect any non-polar clouds, weakening the insolation dominant hypothesis (Rodriguez et al., 2009). Further seasonal progression yielded variation in cloud location, including equatorial bursts of clouds and rain (Turtle et al., 2011b), supplying further constraints on thermal contrast and seasonal effects for GCMs favoring global circulation, rather than surface influence, for cloud distribution (Griffith et al., 2005; Roe et al., 2005b; Brown et al., 2010; Rodriguez et al., 2011; Turtle et al., 2011a).

An immediate follow-up with VIMS and ISS on the north polar lakes would have to wait – Titan was in northern winter and darkness shrouded the north pole. Returning to the south pole, however, VIMS and RADAR observed the same anomalous dark patch in 2008 (Figure 1.3). VIMS showed liquid ethane to be present there while RADAR recorded a specular reflection, confirming Ontario Lacus as a lake (Brown et al., 2008; Wye et al., 2009).

In 2009, VIMS recorded a striking specular reflection off of Jingpo Lacus in the north polar region at the 5 μm wavelength window (Stephan et al., 2010), shown in Figure 1.4. This marked the start of northern summer (Barnes et al., 2011a). Light in the northern polar regions and a partial clearing of the north polar hood (Le Mouélic et al., 2012a) allowed for follow-up coverage by VIMS and ISS, RADAR observed lakes, and new observations of many other lakes, leading to a realization of the asymmetry in lake placement on Titan. *Cassini* revealed that around 95% of Titan's lakes reside at or around the north pole while the south pole has only Ontario Lacus and scattered dry beds (Aharonson et al., 2009). Sand dunes populate the tropic latitudes (Lorenz et al., 2006) with a possible tropical lake (Griffith et al., 2012b). The temperate latitudes show very little contrast, appearing somewhat bland in comparison to the equator and poles.

During the northern winter, a polar hood and various other clouds composed of methane and ethane covered the north pole (Griffith et al., 2006), which suggested precipitation

as a filling mechanism. In 2012, a cloudburst at the equator brought spring showers, darkening several tropic regions (Turtle et al., 2011b; Barnes et al., 2013a). These albedo changes were short lived, however, as those same regions returned to their original albedos in subsequent flybys giving evidence of evaporation. This evaporation made Titan the only body other than Earth to have an active liquid exchange cycle between the surface and atmosphere. The static global distribution of clouds despite Titan's changing seasons complicated GCMs, further constraining methane humidity and convection.

Continued observation of the north pole by RADAR revealed no temporal variations in several of the lakes (Hayes et al., 2008). Retreating shorelines or complete dissipation of lakes would require evaporation or infiltration into a porous regolith, the latter implying a subsurface reservoir and liquid transport. The south pole, however, shows possible temporal variability in many lakes, sometimes with clouds present (Turtle et al., 2009; Hayes et al., 2011). Ephemeral lakes could then undergo evaporation, perhaps in tandem with infiltration, further supplying the clouds and methane cycle. Percolation via a subsurface reservoir, first suggested in 2008 and further explored in 2012, offered another lake filling mechanism, similar to aquifers on Earth (Hayes et al., 2008; Cornet et al., 2012a; Sotin et al., 2012). Assuming a similar local porosity, all basins below a certain elevation in the same area would be filled in a percolation scenario.

Evaporation rates also depend on the humidity and climate while directly affecting lake longevity. Altimetry across Ontario Lacus showed it to be shallow and low elevation (Hayes et al., 2011). Then, a comparison to the Etosha Pan in southwest Africa suggested Ontario was filled by a subsurface alkanifer (Cornet et al., 2012a). Over 3 years of observations, the north polar sea Ligeia Mare showed no shoreline change, counter to what was expected (Sotin et al., 2012). Meanwhile, the interpretation of VIMS' view of Ontario as well as models and lab experiments claimed the lake to have already undergone extensive evaporation, leading to the dominant ethane content, since ethane evaporates much slower than methane (Mitri et al., 2007; Brown et al., 2008; Cornet et al., 2012a; Luspay-Kuti

et al., 2014).

Barnes et al. (2011b) noticed a pattern of 5-μm-bright substrates appearing preferentially around the fringes of north polar lakes in VIMS data. A comparison between VIMS and RADAR near the north pole showed this 5 μm signature within empty basins, but often not near lake features appearing to have a connecting channel. Barnes et al. (2011b) then interpreted this substrate and dichotomy to represent an evaporite either by complete liquid evacuation or shoreline recession. MacKenzie et al. (2014) mapped the global distribution of 5 μm bright material on Titan to assess the plausibility of previously filled lakes and dry lake basins.

Considering that the northern lakes are thought to be composed mostly of methane (Sotin et al., 2012) while ethane may dominate Ontario Lacus (Cornet et al., 2012a; Luspay-Kuti et al., 2014), could there be a longer liquid cycle on Titan in contrast the shorter term methane cycle? One possible explanation is the global migration of liquid over Milankovich time cycles (Aharonson et al., 2009). This idea says that solar flux will vary slightly with the changing eccentricity and precession of Titan's orbit and cause more intense seasonal variations (Lora et al., 2014). If Titan is undergoing liquid migration, we may expect to find lakes, possibly small or relatively short-lived, between the poles, where the largest lakes and basins reside.

What controls where and when rain occurs on Titan? Where did all the observed lakes get their liquid from and if they are evaporating, how are they being replenished? Lakes at the poles complimented by cloud cover suggests a connection between the two. Following earlier observations of clouds near the 40°S latitude band, I survey the southern mid-latitudes for lakes to further constrain if the clouds are confined to certain latitude bands because of lacustrine features or if the clouds are generating temporary lakes. Although we have not seen cloud cover around 40°N, the progression of Titan's long seasons and little to no temporal variability in liquid bodies may provide latitudinal constraints on Titan's climate.

First, I investigate the relationship between temperate lakes and climate on Saturn's moon, Titan. The *Cassini* spacecraft has revealed a multitude of surface features on Titan using a suite of instruments on-board showing a very Earth-like moon. Equatorial sand seas, polar lakes, and cloud systems work in analog with Earth and Earth's climate. I first conduct a survey of the visible, near-, and mid-infrared wavelengths where Titan's methane-dominant atmosphere does not absorb the signal with the Visual and Infrared Mapping Spectrometer. I then characterize two south temperate latitude lakes on Titan with respect to other known lakes, nearby clouds, and the total methane inventory of Titan's clouds. Last, I survey the temperate latitudes as a whole to look for plausible lake candidates to validate scenarios for liquid migration over seasonal or glacial time scales as well as look for patterns in lake location.

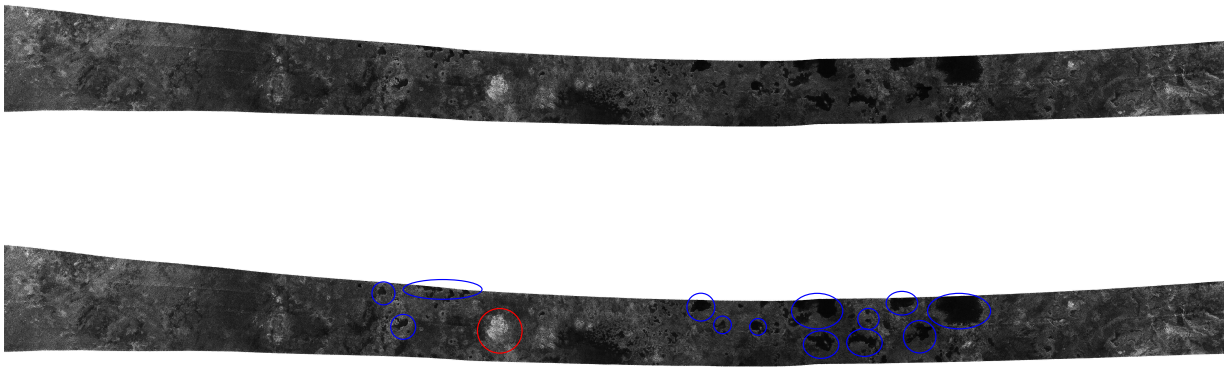

Figure 1.1: An early swath of Titan taken by the SAR instrument on-board *Cassini* during the 16th flyby. The figure shows part of Titan's north polar area, around ∼80°N. For scale, the narrowest portion of the swath measures about 120 km across. The dark features central to the swath, circled in blue, represent areas of specular reflection, signal attenuation, or very smooth surfaces. Stofan et al. (2007) interpreted these dark features to be lacustrine in nature, finding the first plausible lakes on Titan. The red circle shows a mountain in RADAR.

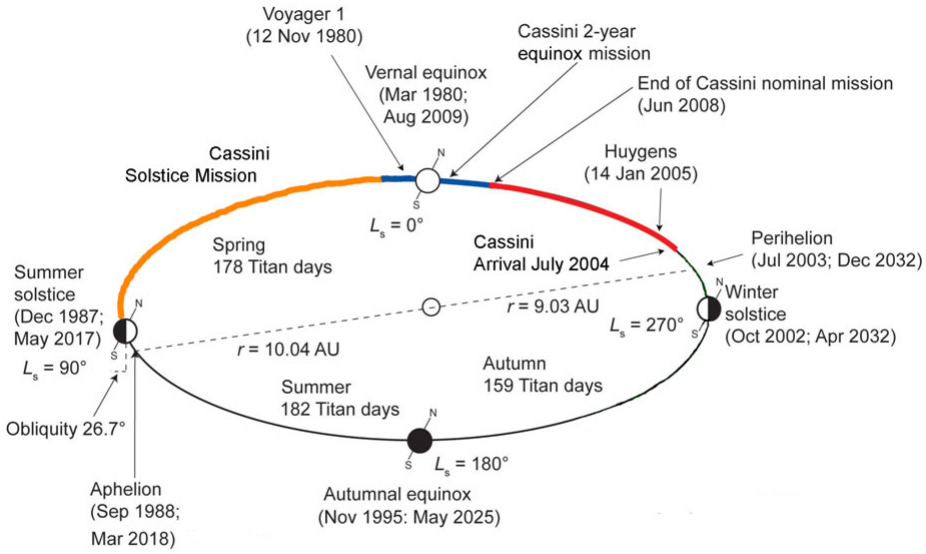

Figure 1.2: The orbit and seasonal progression of Titan during the *Cassini* nominal, Equinox, and Solstice missions. (Image Credit: Ralph Lorenz)

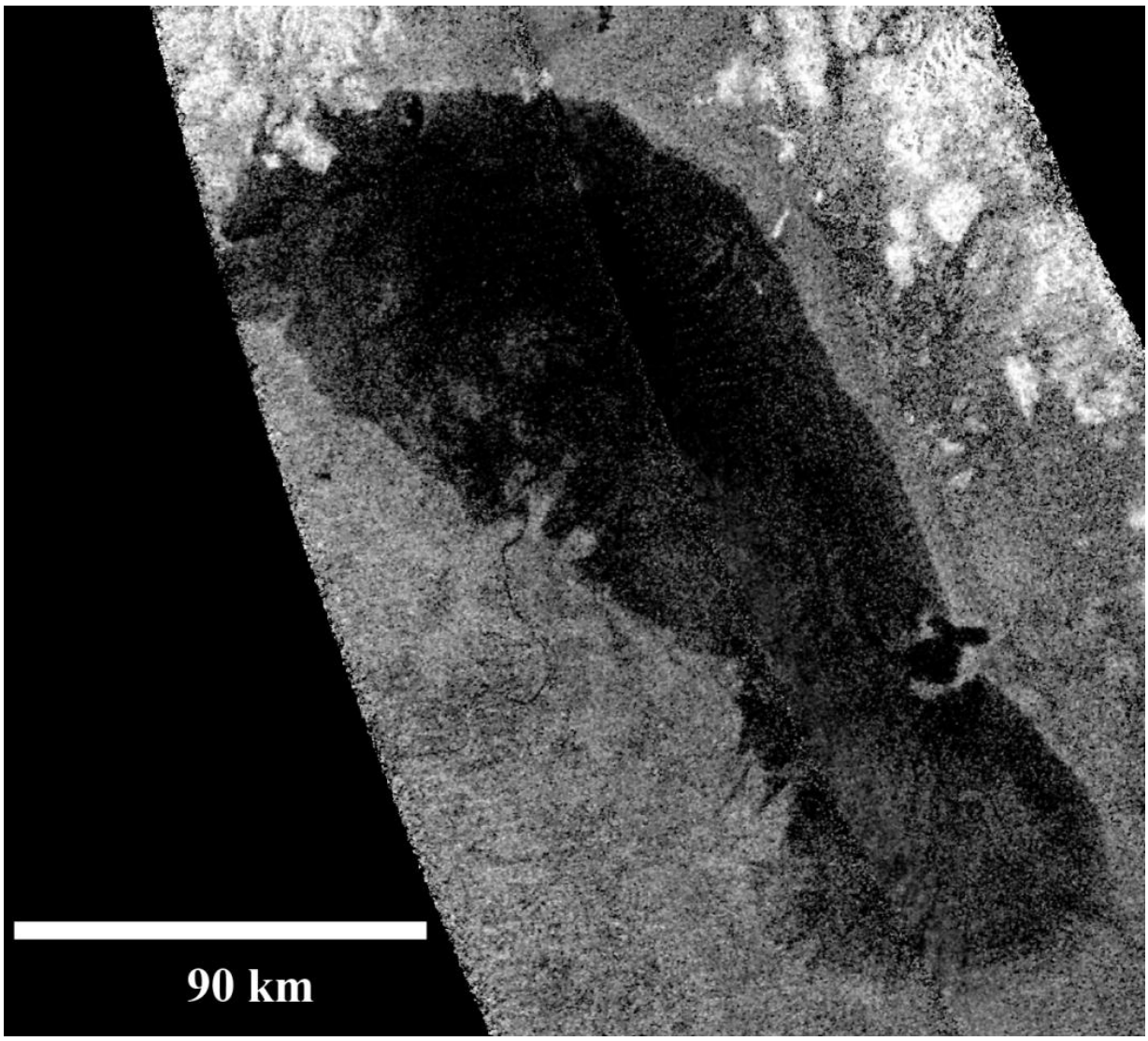

Figure 1.3: This is the SAR image of Ontario Lacus near Titan's south pole. The brightness in the image represents the roughness of the surface scattering the signal. SAR can penetrate ∼10 m into the subsurface; the gray pixels appearing within the bounds of the lake show the lake floor. Ontario also has a channel connected to its central-western shore.

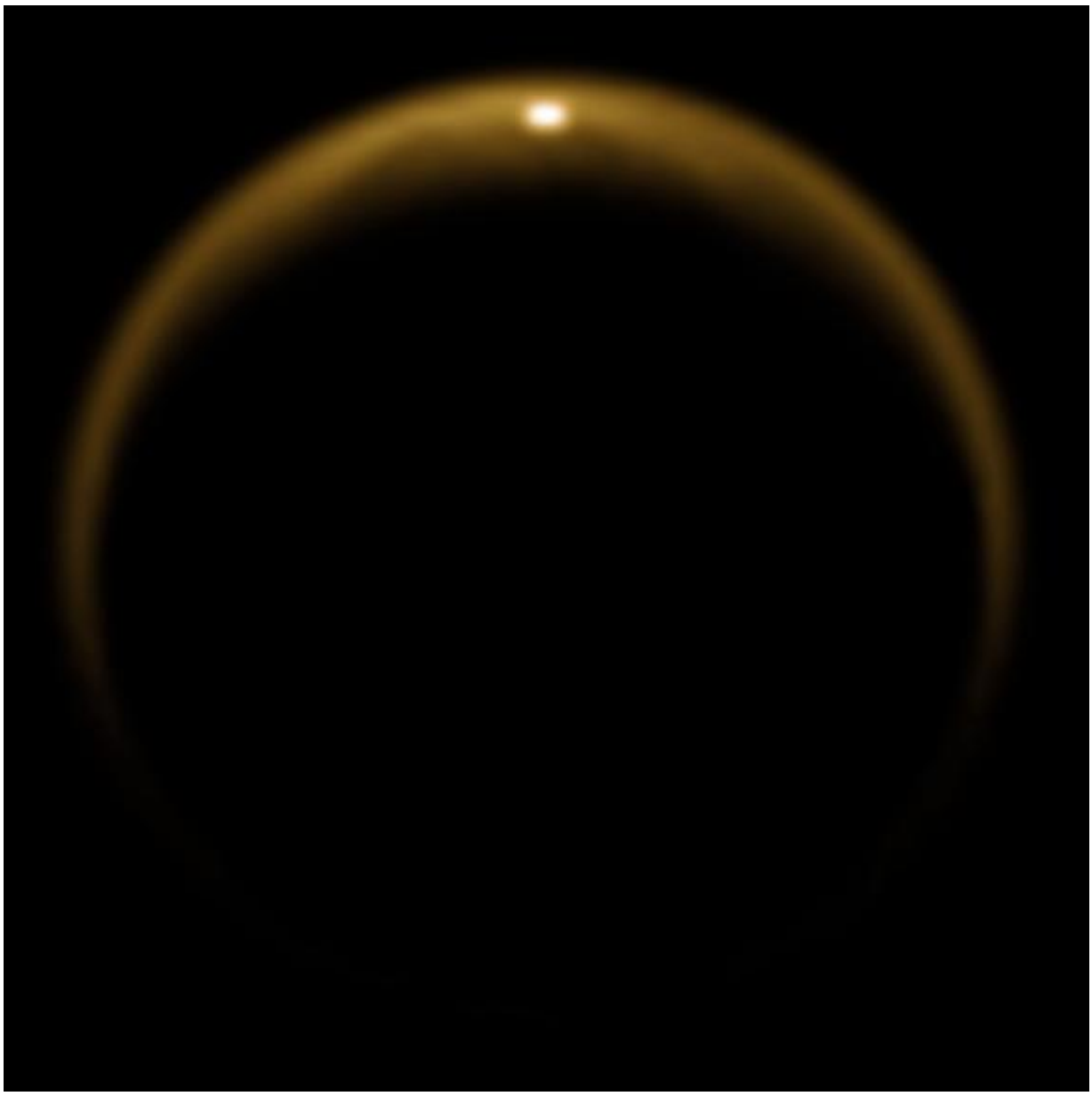

Figure 1.4: This VIMS image shows a specular reflection of the Sun off of Jingpo Lacus in Titan's north polar region in the 5 μm channel. The wavelength advantageously passes through much of Titan's atmosphere with minimal scattering contribution. A specular reflection also requires a mirror-like surface, shown here that Jingpo has no waves or surface roughness.

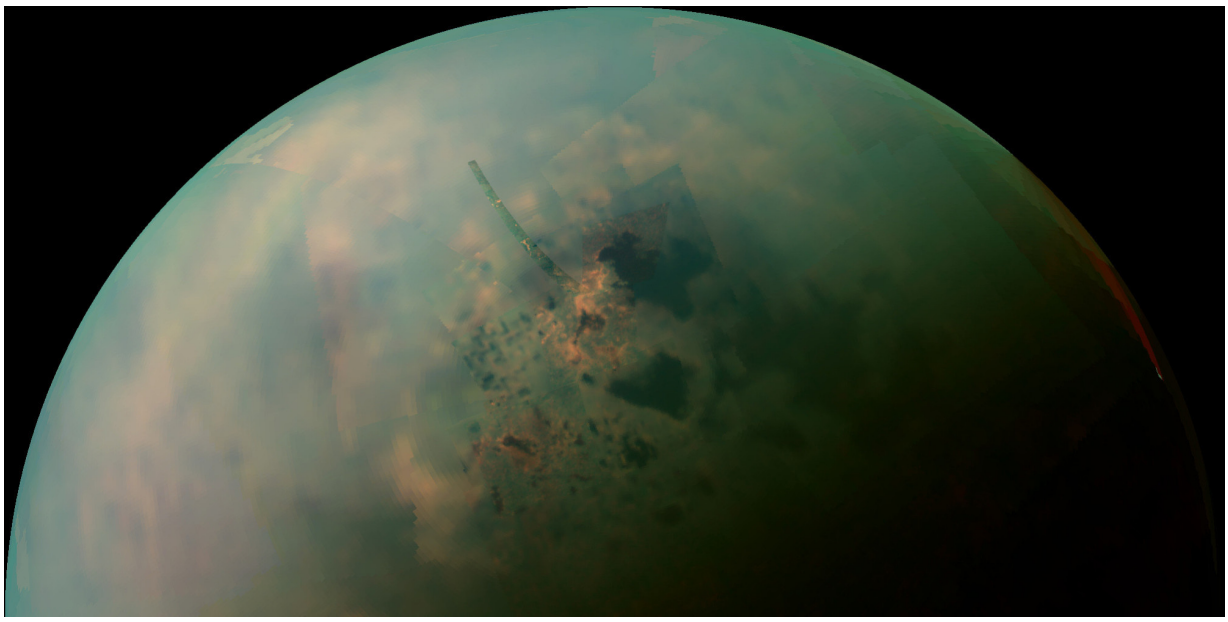

Figure 1.5: The north pole holds 95% of Titan's lakes, shown here as the darkest features in this VIMS image from T94. This false color composite applies blue to 1.28 μm, green to 2.01 μm, and red to the 4.8-5.2 μm channels. The larger lake bodies are comparable in scale to Lake Superior, USA/CAN.

Chapter 2

Mapping Titan's Surface Features within the Visible Spectrum via *Cassini* VIMS

Graham Vixie[1], Jason W. Barnes[1], Jacob Bow[1], Stéphane Le Mouélic[2], Sébastien Rodriguez[3], Robert H. Brown[4], Priscilla Cerroni[5], Federico Tosi[6], Bonnie Buratti[7], Christophe Sotin[7], Gianrico Filacchione[5], Fabrizio Capaccioni[5], Angioletta Coradini[6]

1. University of Idaho, Department of Physics,
P.O. Box 440903, Moscow, ID 83844-0903
2. Laboratorie de Planétologie et Géodynamique, CNRS UMR 6112,
2 rue de la Houssinière, Université de Nantes, 44300 Nantes, France
3. Laboratoire AIM, Université Paris Diderot - Paris 7/CNRS/CEA-Saclay,
DSM/IRFU/SAp, Gif sur Yvette, France
4. University of Arizona, Lunar and Planetary Laboratory,
1629 East University Blvd, Tucson, AZ, 85721-0092
5. Istituto di Astrofisica Spaziale e Fisica Cosmica, Sezione di Roma,
Via Fosso del Cavaliere 100, Tor Vergata, IT 00133 Roma, Italy
6. Istituto di Fisica dello Spazio Interplanetario, Via Fosso del Cavaliere 100,
IT 00133 Roma, Italy
7. California Institute of Technology/Jet Propulsion Laboratory,
4800 Oak Grove Drive, Pasadena CA, 91109

2012, Planetary and Space Science, Issue 60, Pages 52-61

Email address: gvixie@vandals.uidaho.edu

Abstract

Titan shows its surface through many methane windows in the 1-5μm region. Windows at shorter wavelengths also exist, polluted by scattering off of atmospheric haze that reduces the surface contrast. At visible wavelengths, the surface of Titan has been observed by Voyager I, the Hubble Space Telescope, and ground-based telescopes. We present here global surface mapping of Titan using the visible wavelength channels from *Cassini*'s Visual and Infrared Mapping Spectrometer (VIMS). We show global maps in each of the VIMS-V channels extending from 0.35 - 1.05 microns. We find methane windows at 0.637μm, 0.681μm, 0.754μm, 0.827μm, 0.937μm, and 1.046μm and apply an RGB color scheme to the 0.754, 0.827 and 0.937μm windows to search for surface albedo variations. Our results show that Titan appears gray at visible wavelengths; hence scattering albedo is a good approximation of the Bond albedo. Maps of this genre have already been made and published using the infrared channels of VIMS. Ours are the first global maps of Titan shortward of 0.938 microns. We compare the older IR maps to the new VIMS-V maps to constrain surface composition. For instance Tui Regio and Hotei Regio, referred to as 5-micron bright spots in previous papers, do not distinguish themselves at all at visible wavelengths. The distinction between the dune areas and the bright albedo spots, however, such as the difference between Xanadu and Senkyo, is easily discernible. We employ an empirically-derived algorithm to remove haze layers from Titan, revealing a better look at the surface contrast.

Keywords: Titan, Surface, Optical Wavelength, Visible Imaging, Cassini VIMS

2.1 Introduction

We present here findings from the *Cassini* spacecraft, which is on its second extended mission, via the Visual and Infrared Mapping Spectrometer (VIMS) instrument (Brown

et al., 2004). Much of Titan's surface has already been seen from RADAR and infrared wavelengths, but surface features have been sparsely identified in the visible spectrum. Methane windows do exist in the visible, albeit not as transparently as in the IR; using them, new constraints can be placed on the composition of Titan's surface.

The ability to view Titan's surface was pioneered near the beginning of the 1990's with the discovery of near-infrared methane windows by McKay et al. (1989a) and Griffith et al. (1991). Titan's surface was first seen in optical wavelengths by Voyager I as discussed by Richardson et al. (2004) using wavelengths ranging from 590 - 640 nm, and by Smith et al. (1996) using the window at 0.94μm. The Hubble Space Telescope (HST) also observed Titan's surface at 673 nm (Smith et al., 1996). Relative brightness maps of Titan were produced from the HST data by Smith et al. (1996) and with *Cassini*'s Imaging Science Subsystem (ISS) by Turtle et al. (2009, 2011a).

The VIMS visible channel measures optical spectra from 0.351μm - 1.05μm split up over 96 channels using a slit-scanning visible spectrometer (Capaccioni et al., 1998). We can then peruse each wavelength channel to identify which wavelengths can pierce through Titan's atmosphere to the surface. This has been done in infrared channels by Barnes et al. (2007), but comprehensive global maps have not previously been produced at wavelengths shortward of 0.938μm. Spectra of Titan in the visible range appear in Neff et al. (1984) and Lockwood et al. (1986) where each paper suggested visible windows. Neff et al. (1984) showed the albedo of Titan with high enough signal-to-noise that methane windows are visible. Karkoschka (1994) showed the first detailed visible spectrum of Titan that has high enough signal-to-noise to discriminate the edges of atmospheric windows. Methane windows are visible in this spectrum (Karkoschka (1994) Figure 3), but the specific wavelengths where the surface is visible cannot be delineated from these spatially-unresolved spectra. The methane absorption band peaks coming from lab measurements listed in Karkoschka (1994) Table 7 do not, by themselves, allow determination of where the surface is visible, either. Karkoschka (1994) is mainly focused on atmospheric spectral features.

Consequently, the work that we describe here is the first to show Titan's surface and monitor some heterogeneities shortward of 0.9 μm.

The goal of this study is to constrain surface composition by generating and analyzing a global map of Titan using methane windows in the optical spectrum. In Section 2 we produce a map using data from five of *Cassini*'s flybys: T8, T9, T31, T34, and rev9. For more information on the observations on these flybys, see Barnes et al. (2009b). These flybys were chosen to minimize variance in phase on the global map while maximizing area covered on Titan. We then combine the resulting data together at each wavelength to show surface features on Titan. The end product is a global scale, atmospherically uncorrected, 25-color map. The process of calibrating each individual cube of data and making the maps is outlined in detail in Barnes et al. (2007). The purpose of these maps is to provide another comparative point to the IR maps in hopes of further constraining surface composition and more accurately defining the surface features, which we do in Sections 3-5.

2.2 Processing of Imaging Observations

2.2.1 Mapping

Titan's surface is obscured by scattering and absorption by both haze and methane in the atmosphere in optical wavelengths. At most infrared wavelengths, Titan's atmospheric methane absorbs heavily, making the surface impossible to see. We use *Cassini* VIMS to scan Titan at all wavelengths to find certain windows where incident solar flux can pass through nearly unhindered and return a signal from the surface. We focus on certain optical wavelength windows where photons are not absorbed by the atmosphere.

We start the map-making process by selecting all observations where surface features are apparent. Next, we wrote software to place all data cubes from these observations on a single cylindrically projected map based on each cube's embedded latitude and longitude

information. We then found certain wavelengths where the surface of Titan becomes apparent by looking at these combined observations at every available wavelength. Figure 2.1 shows Titan at all the visible wavelength channels on the VIMS instrument. The three wavelengths showing the most surface features from observation are 0.754μm, 0.827μm, and 0.937μm. The final step was then to created a color composite by assigning each of these wavelengths a color and optimizing contrast in order to show surface variations. We assign the colors blue, green, and red, respectively, to define the RGB map. Figure 2.2 shows all identified optical wavelength methane windows at constant contrast. The flybys and individual observations were chosen to maximize longitudinal coverage and be close in phase. Information regarding each flyby used may be found in Table 1. We present then our global scale, atmospherically uncorrected RGB surface reflectivity map of Titan in Figure 2.3. This map can then be compared to other known IR maps (see Figure 2.4) to identify surface characteristics.

The 0.937μm reveals the most surface features out of the visible channels since the atmosphere absorbs the least at this wavelength. However, we use two other channels for several reasons. First, we are comparing the surface at different wavelengths and therefore wish to identify any anomaly that is limited to a certain wavelength(s). This is achieved through the creation of the color composite. Features that show more strongly in one (or two) of our primary colors are easier to constrain. Second, global maps of Titan have already been published in the 0.937μm wavelength courtesy of ISS. Finally, the more wavelength we can incorporate in to our map while still maintaining surface albedo variability, the greater coverage we have of the spectrum on Titan.

We can identify many familiar landmarks in Figure 2.3 such as Shangri-La, Xanadu, and the sideways "H" of Fensal and Aztlan. 5-micron bright regions like Tui Regio (Barnes et al., 2006) and Hotei Regio (Soderblom et al., 2009; Barnes et al., 2005) do not show strong contrast in the visible map like in the IR maps, as shown in Figure 2.4, nor do the Selk or Sinlap craters. These regions are all gray at shorter wavelengths. While the visible

color is orange, for clarification, we use the word "gray" to mean that the spectral response is flat and the reflectivity does not vary significantly with wavelength in the visible part of the spectrum.

The global views of Titan (orthographic projections) give an undistorted look at surface features (Figure 2.3 bottom). The dark lines that appear on the global maps are seams between the different flybys. The seams are present mostly due to differing phase angles between flybys, limb-darkening, and not being able to fully correct atmospheric effects. The solar incidence and emission angles change over the course of a single flyby as well. Figure 2.5 shows the change in these angles and pinpoints the locations of nadir points. At different phase angles, the flyby appears darker, lighter, smoother, or more noisy. The effect of changing phase angles will be discussed in Section 3. Special attention was paid to weaving the different flybys together, as we want the map to look as seamless as possible. The figure of merit used by Barnes et al. (2007) was changed to solely rely on the emission angle in an effort to minimize the seams between flybys.

Noise here is not instrument noise, but rather stripe noise in the VIMS-V instrument. At the end of each row of pixels in the slit scanner, there is a column shielded that measures dark current. The background measured by this dark stripe is actually only measured by a single pixel (the rest of the measurements are thrown away) then subtracted from all the other pixels. The problem here is sometimes a photon will get in and be measured by this pixel giving a higher value to the background. This is also the origin of the striping on the maps. The noise then does not come from the image or the haze, but rather the instrument itself.

Atmospheric scattering is what drives the different appearance as a function of observation geometry. As light from the Sun enters Titan's atmosphere, many possible paths emerge after the light encounters atmospheric haze particles. The light may (ideally) reflect from the surface and go directly to *Cassini*; more probably, however, the photons collides with haze particles and scatters. This greatly decreases the fraction of photons that suc-

cessfully travel to Titan's surface and back. Part of this indirect light, backscattered to the spacecraft by Titan's haze without reaching the surface, causes additive offsets that must be corrected (visible - Perry et al. (2005), IR - Rodriguez et al. (2006); Le Mouélic et al. (2008); Le Mouélic et al. (2012b)).

2.2.2 Haze Removal and Comparison

Owing to high optical depth, spherical geometry, and uncertainties in scattering properties, it is not presently possible to properly correct for the atmospheric conversion of incident solar flux (I/F) to albedo using radiative transfer. The work of Perry et al. (2005) on ISS data allow us to further our mapping algorithms by empirically compensating for some of the haze to enhance surface contrast. The purpose of this article is present maps, thus further analysis of atmospheric or haze corrections is beyond the scope of this paper. We did try simple subtraction and ratio based techniques, but our best results came using the ISS techniques directly.

Using the I/F maps in Figure 2.1 as our starting point, we created a haze-only map using nine wavelengths where our signal is almost completely absorbed and that showed no surface features whatsoever. The wavelengths used to make the haze map are 0.585μm, 0.599μm, 0.607μm, 0.622μm, 0.651μm, 0.659μm, 0.666μm, 0.709μm, and 0.878μm. Following the Perry et al. (2005) algorithm, we divided the original map (Figure 2.3) at each of the methane window wavelengths labeled in Figure 2.2 by the haze map to create a new, empirically haze-corrected map (Figure 2.2B). Using the same color/wavelength setup as the original, we created a new global RGB map (Figure 2.6). Trial and error by Perry et al. (2005) shows that a subtraction step yields lower-quality results. By compensating for wavelengths where our signal is nearly totally absorbed, we make surface features more visible. The resulting map has slightly more striping, but accounts for phase angle as to reduce the visibility of the seams between flybys. Most importantly, the new map shows an improved view of the surface features of Titan as well as reveals some new areas that

are barely or not at all visible without correction. Comparing Figures 2.3 and 2.6 show that the dark areas on Titan cover more area with some new areas appearing south of Shangri-La in the west, through the north of Tsegihi, and south of Belet in the east. The improved contrast of the map in Figure 2.6 makes the empirically-corrected visible maps much more useful than the uncorrected map (Figure 2.3).

Stephan et al. (2009) created a global albedo map of Titan using data collected from 2004-2008 by the ISS via a narrow band pass filter set at 0.938μm (Porco et al., 2004). The albedo differences were described in Turtle et al. (2009) as being compositionally related as opposed to topographical. This map was also refined using the same method listed in Perry et al. (2005) and is compared with Figure 2.6 in part in Section 4. The color scheme in Figure 2.6 helps to distinguish the surface reflectivity differences. As discussed later, there are some areas present in our visible map that are obscured by haze in the ISS 0.938μm map.

2.3 Spectroscopy

A spectral comparison between bright and dark surface albedos on Titan's surface tells us how much light at every wavelength channel in the VIMS instrument transmits or is absorbed going through the atmosphere. We chose areas of the same size, one bright and one dark region on Titan near each other so that we have similar phase angle at each location. The regions chosen were from the T8 flyby of Xanadu and Shangri-La and are boxes of uniform albedo along the same latitudinal lines. The longitude for Xanadu's region is 145°W to 140°W and Shangri-La's is 155°W to 150°W with the shared latitude region of 8°S to 12°S for a total of 20 pixels per box (Table 1). The plot in Figure 2.7 is a spectral ratio dividing Xanadu by Shangri-La. This spectral ratio shows the precise outlines of methane windows at 0.637μm, 0.681μm, 0.754μm, 0.827μm, 0.937μm, and 1.046μm. A spectrum similar to this was presented in Lemmon et al. (2002) by subtracting a dark

area spectrum from a bright area spectrum and the visible methane windows are resolved, albeit with low I/F. Lemmon et al. (2002)'s spectrum anticipates our Figure 2.7 which further resolves Titan's visible spectrum and constrains the wavelengths where surface features are visible. Light from Titan's surface may be seen within these wavelengths by any Earth-based telescope sporting Adaptive Optics, given the right filter. Voyager I resolved Titan's surface via a slight albedo difference (Richardson et al., 2004), though this was not recognized for 25 years after the flyby.

The phase angle, the angle from *Cassini* to Titan to the Sun, affects the spectra because of changing haze scattering properties. The spectrum in Figure 2.7 was taken from the T8 flyby which had an ingress phase angle of 21°. We compare this T8 spectrum to Tsegihi/Aztlan in Ta, T3, T10, and T12 to sample the effect of phase angle on surface contrast. The dates and phases of each flyby are listed in Table 1. Rannou et al. (2003) did a center-to-limb contrast variation previously at 673 nm by showing a greater relative contrast in bright and dark surface features the further the distance from the limb.

Figure 2.8 shows spectra from each flyby alongside each other for comparison. A value of 1 indicates that the regions of Tsegihi and Aztlan look the same at the given wavelength. The trend that we find here is that as phase angle increases, the systematic effects of haze increase and the baseline goes above 1, reducing the effective I/F of transmission peaks (i.e. inhibiting surface viewing).

The height of the intensity peak remains constant above the height of the baseline as phase increases. The spectrum for Ta compared to the spectrum for T12 has the baseline much closer to unity and shows less scattering; this suggests that low phase angles yield clearer results. Judging from the level of noise in the T12 flyby, there seems to be a phase angle at which the data become too noisy to be useful. The lower the phase angle is, the less scattering occurs and the better quality surface viewing is. When the phase angle is high, the lower I/F from limb darkening reduces the signal. Phase angles $< 30°$ minimize atmospheric factors and maximize surface contrast.

2.4 Comparison to the Infrared

We compare optical wavelength map in Figure 2.3 to the previous infrared map in Figure 2.4 to extend the region of spectral coverage. The optical map has less distinguished contrast within light and dark regions, whereas the infrared map described in Barnes et al. (2009b) has many different distinguishable spectral variations within the light and dark regions. Since Titan appears gray within the optical windows, the single scattering albedo (the ratio of scattering efficiency to total extinction efficiency) must be a good approximation of the Bond albedo. The 5-micron bright areas, Tui Regio and Hotei Regio, for instance, do not appear distinguished from the rest of Xanadu.

The Selk and Sinlap craters are not resolved on the visible map. This is not due to the wavelength directly; a surface feature of this type should not depend on the wavelength in which it is observed unless the feature is covered in some optically sensitive material. The reason these craters do not appear is because of the resolution of the slit scanner on *Cassini* combined with the extra atmospheric scatter from working in the visual wavelengths. The VIMS-V scans at low resolution in order to compile a global view of Titan; however, a crater at most appearing in two pixels (See Table 1) will still fail to be resolved because of the high amount of atmospheric scattering, even though the ejecta blankets are apparent.

All of the light and dark albedo features, first described by Porco et al. (2005), are the focus of the discussion for surface composition. The next step is to do a systematic comparison of spectral types between the map in the visible (Figures 2.3 and 2.6) to a well described IR map (Figure 2.4) based on Barnes et al. (2007). The type of material each color and shade refers to is described in the aforementioned paper and will not be discussed here. A systematic comparison of each spectral signature in the IR methane windows to composition types can be found in McCord et al. (2008).

2.4.1 Equatorial Zone

The equatorial zone bounded by 30° north and south of the equator is home to the greatest contrast on Titan's surface. VIMS-V can distinguish light and dark terrain, and the dark terrain is split into dark and light blue spectral types. The light colored (white) terrain is slightly brighter across Xanadu and Tsegihi (Figure 2.3) but is mostly uniform across Titan (Figure 2.6).

Dark

The dark regime covers the majority of Titan's equatorial region and corresponds to the vast sand seas littering Titan's surface (Barnes et al., 2007; Soderblom et al., 2007). The placement of the dark areas agree almost exactly with the dark brown spectral unit, giving us a good comparison standard. Although the resolution is coarser in the visible than in the IR, the boundaries between spectral types are sharper in the visible map in Figure 2.6.

The eastern sections of the equatorial area in each map do not agree as well in total surface features visible. Belet does not stand out as well in the visible map from being on a seam between flybys, thus making the emission angle higher, causing more haze and lower surface contrast. The section south of Adiri, however, is clearer in the visible. Just above the 30°S mark on the eastern end of the map, we can see the dark extend down into an open region not visible on the IR map. These new areas could be outlines of dune material.

Visible Light Blue

The light blue regime corresponds closely to the dark blue IR spectral unit but also covers additional area. In Figure 2.6, the light blue serves as the midway between the white and dark areas. The light blue in the visible matches all of the dark blue areas in the IR map but also extends to some other areas, most notably: northern Shangri-La in the west, northeast Senkyo in the center, and around the outer fringes of Adiri in the east.

VIMS dark blue areas are thought to be dirty water ice (Rodriguez et al., 2006; Le Mouélic et al., 2008; Soderblom et al., 2007; Barnes et al., 2007) or organic compounds (Clark et al., 2010). Figure 2.9 compares the water ice spectrum from Enceladus to a spectrum of the light blue (dark blue IR) spectral unit in northern Shangri-La, similar to Griffith et al. (2003). The overall reflectivity in Enceladus produces a much higher I/F since there is no atmosphere to contend with. However, the gray appearance and greater relative brightness of the light blue spectrum in the visible wavelengths is broadly consistent with water ice, but certainly does not rule out the many possible organic compounds.

Xanadu

While Xanadu stands out as a bright albedo feature in the IR, the difference between Xanadu and the rest of the bright terrain in the visible maps are not as striking. Xanadu appears a little brighter in Figure 2.3 than the rest of the bright terrain; also in Figure 2.6, Xanadu is distinguished from its surroundings.

2.4.2 Mid Latitude Zone

The mid latitude zone on Titan extends from 30° to 60° north and south. On the IR map, these regions are fuzzy and have nothing of real note except for the brighter albedo feature Tsegihi. In the visible, there is a new area south of Shangri-La in the west not visible on the IR map. The 5 μm bright features on the IR map are non-existent on the visible map; however, Tui Regio, south of Xanadu, can be described by its outline.

Tsegihi

Tsegihi is the second brightest large albedo feature in the IR. However, as seen in Figure 2.3, Tsegihi is the brightest albedo feature–even more so than Xanadu. This brightness of albedo may arise from the low phase angle of T9, the flyby comprising 90°W to roughly 20°E. In Figure 2.6, with the haze removed, Tsegihi appears, again, to be nothing of note

and instead shows some splotches of light blue spectral types in the north and west areas corresponding to some light brown areas on the IR map.

Blue White

This section is lighter in color than the light blue in the equatorial region and exists south of Shangri-La. In the IR, this section appears to be a group of 5-micron bright area with no real boundary. In the visible, however, we can make out a fringe between this blue white region, Tui Regio, and the surrounding area. This area in question is slightly larger than Shangri-La itself and has its southern boundary much more visible in Figure 2.6.

White

The greatest area of Titan is comprised of white (Figure 2.3) color corresponding to the equatorial bright spectral unit and many of the 5-micron bright areas of the IR map. This substrate covers the majority of Titan not occupied by the sand dunes.

2.5 Conclusion

The spectral albedo comparison of bright and dark surfaces on Titan confirms transmission peaks in the optical wavelengths. This gives targets to ground based observers with Active Optics telescopes and allows for the possibility of resolving the surface of Titan using visible spectrum filters from Earth (Lemmon et al., 2002). This would allow more frequent data acquisition from a moon so far away.

The visible spectrum mainly shows gray albedo changes for surface features on Titan. This serves as another constraint on surface composition to the IR maps published already. The main, larger features on Titan are distinguishable at visible wavelengths but the smaller features and the 5-micron bright areas are not. We attributed this to either the lower spatial resolution (the spatial sampling does not change) of VIMS-V or to the

inherent reflectivity of material on the surface that is apparent only in the IR, respectively. The improved surface contrast viewing Titan with some haze removed, however, proves useful for seeing the extent to which certain surface features reach.

Our transmission spectrum in Figure 2.7 is the major result from the visible wavelength observations for this paper. Knowing precisely where windows exist in the optical wavelengths can improve how spacecraft time is spent and what is targeted. If ground based observers can resolve the surface of Titan, then those observations can be used to pick out targets for *Cassini* or any other spacecraft that may visit the Saturn system in the future.

The surface of Titan, scanned over all the visible VIMS channels, appears gray in each individual wavelength. All the photons *Cassini* receives back have been scattered to some extent but not absorbed by the atmosphere. We can make good use of the scattering albedo then as an approximation for the Bond albedo.

The IR wavelengths provide more spectral features for understanding the surface composition; but optical maps help to exclude surface materials not active in visible wavelengths, and as such provide a useful complement to longer-wavelength studies. This paper's intent is to report on wavelengths *Cassini* already scans, rather than arrive at specific constraints.

2.6 Acknowledgements

The work done here was made possible by NASA, ESA, and the VIMS team. The authors also acknowledge funding from grant NNX09AP34G to JWB from the NASA Outer Planets Research program. P. Cerroni, F. Capaccioni, A. Coradini, G. Filacchione and F. Tosi acknowledge the support of ASI grant I/015/09/0.

Table 1

Flyby	Rev Number	Date	Subsolar Point	No. of Cubes	Phase Angle	Best Spatial Sampling (km)
N/A	rev9	2005 Jun 6	21.1°S 145°W	6	71°	109
T8	rev17	2005 Oct 28	19.6°S 139°W	18	21°	42
T9	rev19	2005 Dec 26	18.9°S 45°W	25	35°	2.9
T31	rev45	2007 May 28	12.0°S 156°E	11	22°	11
T34	rev48	2007 Jul 19	11.3°S 78°E	8	38°	8
Ta	revA	2004 Oct 26	23.2°S 165°W	1	9°	2.6
T3	rev3	2005 Feb 15	22.2°S 155°W	1	20°	7
T10	rev20	2006 Jan 15	18.7°S 127°W	1	28°	3.9
T12	rev22	2006 Mar 18	17.9°S 96°W	1	53°	7

Table 2.1: This table summarizes the *Cassini* observations used in this paper.

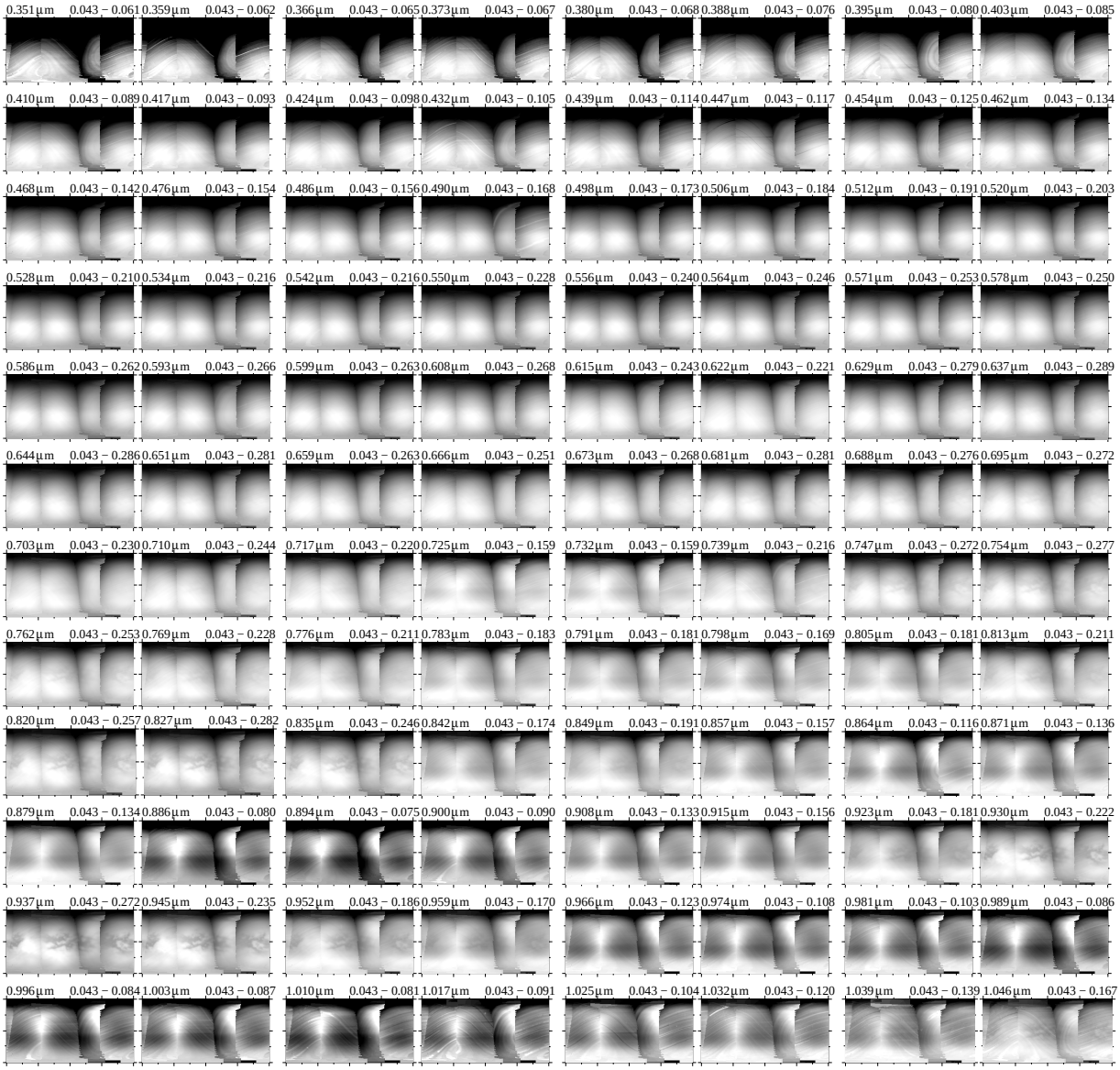

Figure 2.1: Here we show Titan globally at the entirety of the VIMS-VIS range. The top left window represents the beginning of the 96 optical wavelength channels, 0.35μm, with wavelength increasing incrementally moving to the right. A quick look over all of the different wavelengths in the figure above reveal that there are few that show the surface. Methane has fewer windows in the optical spectrum than it does in the infrared, and scattering is more prevalent, but we can still see distinctions on Titan's surface.

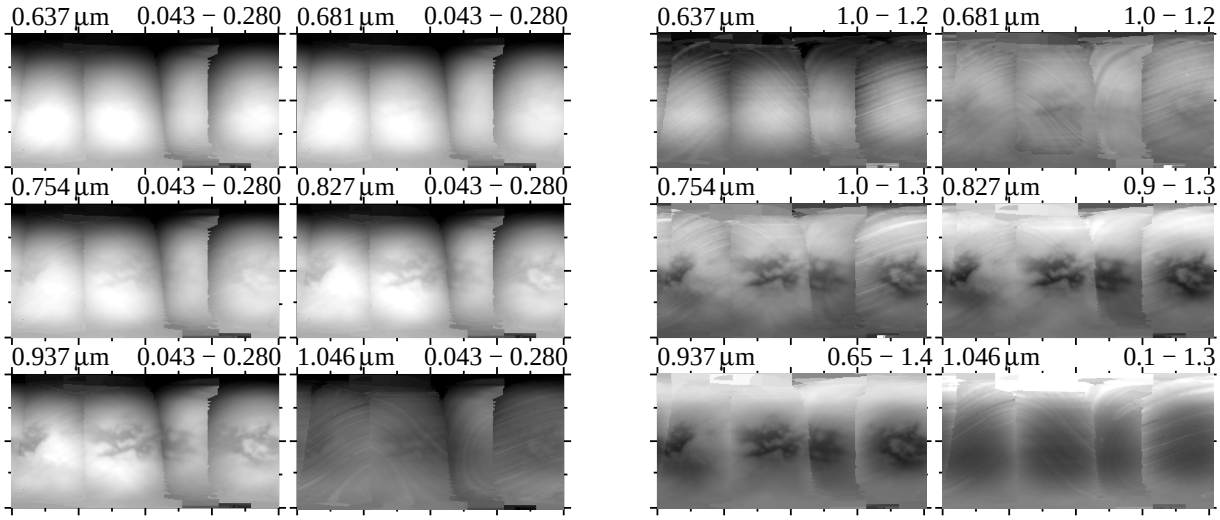

Figure 2.2: On the left are global I/F maps of Titan without atmospheric correction. The longitude convention has 0°W down the center of each Titan image. Wavelength and contrast are listed in the top left and top right, respectively, of each image. On the right are corrected maps, with the haze divided out according to the Perry et al. (2005) empirical algorithm described in the text. Contrast is constant in the left set of images and set to maximize surface feature distinction in the right.

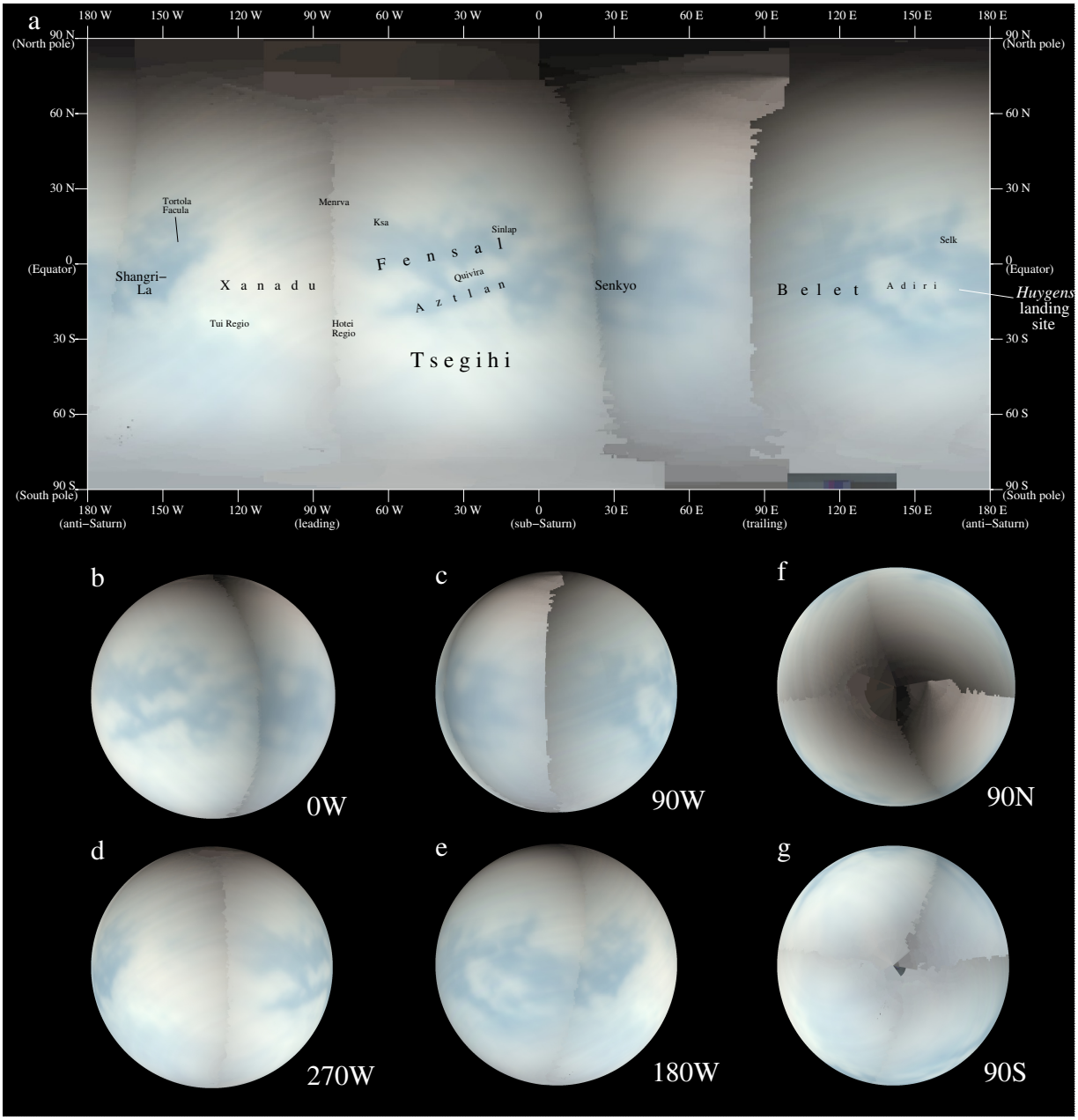

Figure 2.3: This atmospherically uncorrected I/F map of Titan uses VIMS coverage from T8, T9, T31, T34, and rev9 in cylindrical projection (a). The colors and wavelengths used to make this map are red at 0.937μm, green at 0.827μm, and blue at 0.754μm. Part a of the figure shows a simple cylindrical map of the five flybys sewn together. Parts b-g of the figure show the different faces of Titan in an orthographic projection. In comparison to infrared maps, our optical map shows less distinction between different wavelengths. However, note that the 5-micron bright spots do not stand out with the exception of Tui Regio.

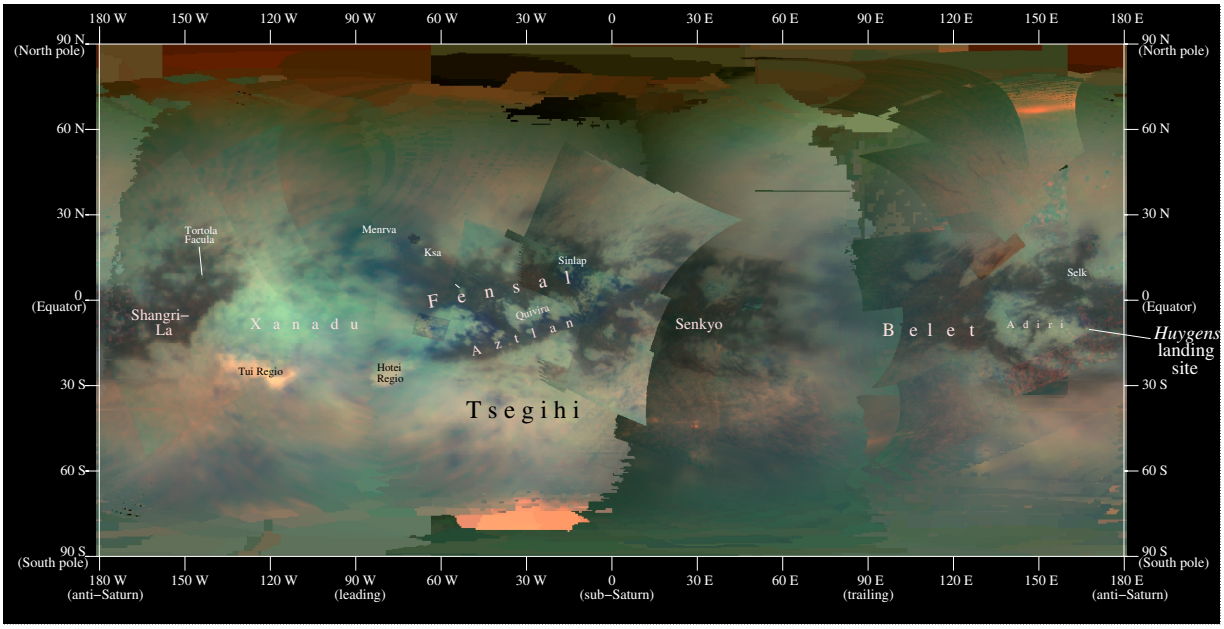

Figure 2.4: This figure represents the work of Barnes et al. (2009b) in mapping Titan using atmospheric windows in the infrared spectrum. The dark blue color on the optical wavelength map corresponds to the darkest green on the IR map. The bright orange color in the IR map represents the 5-micron active sites (bright orange features near the poles are clouds). Many differences can be seen comparing the infrared and visible maps. In particular, Tsegihi shows up bright in the optical wavelengths, just as bright as Xanadu. At 5μm, Tsegihi is actually brighter than Xanadu. At longer wavelengths Tsegihi is not as prominent and does not stand out from the rest of the area in the southern regions; but it does look different in the optical map.

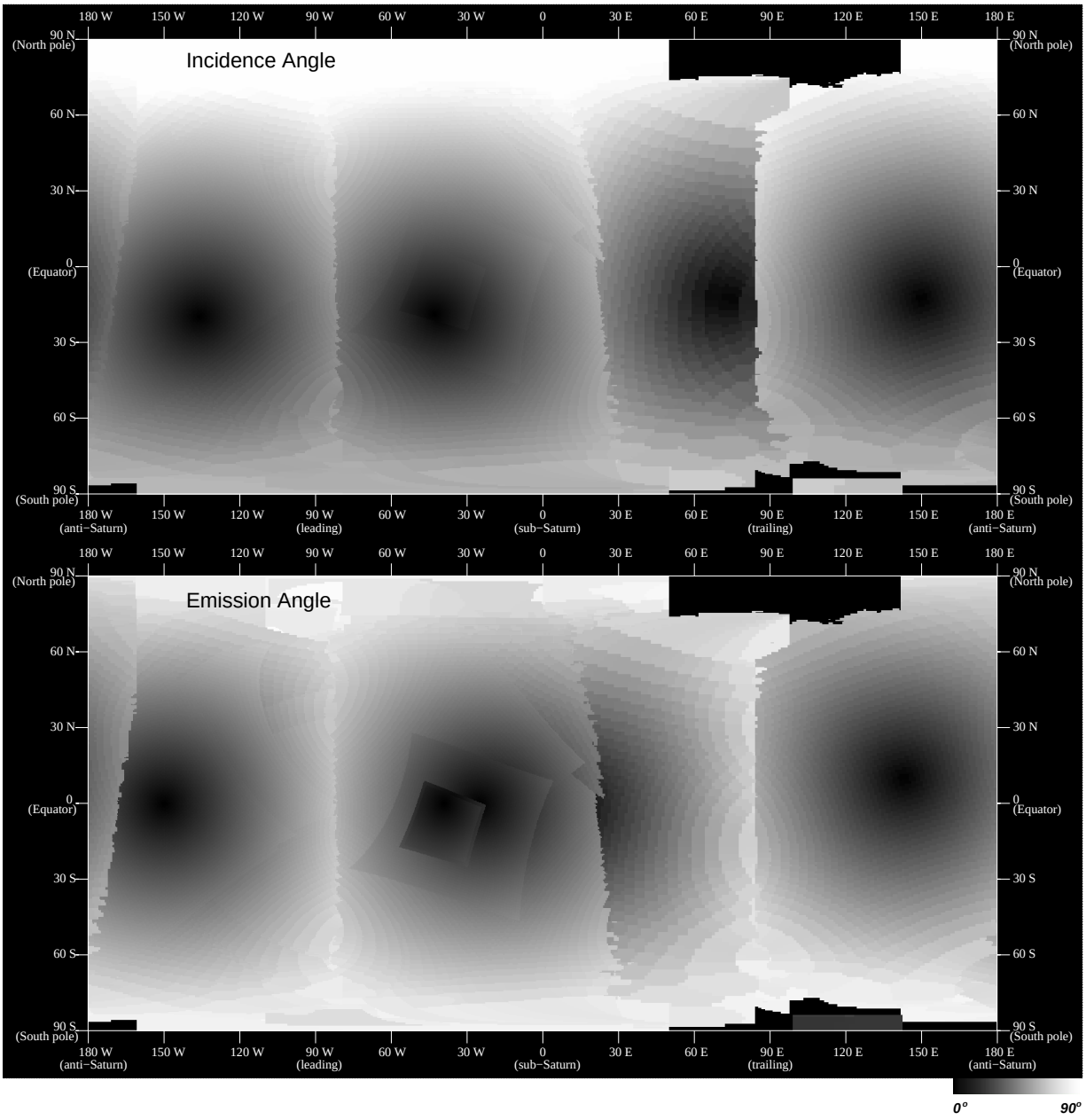

Figure 2.5: The top map represents the incidence angle as it changes over each flyby. The bottom map represents the emission angle. The angles, in both cases, increase towards the center of a flyby, then starts to drops off. These maps identify the nadir points where the signal-to-noise ratio is the greatest in relation to the resolution in Figures 2.3 and 2.6.

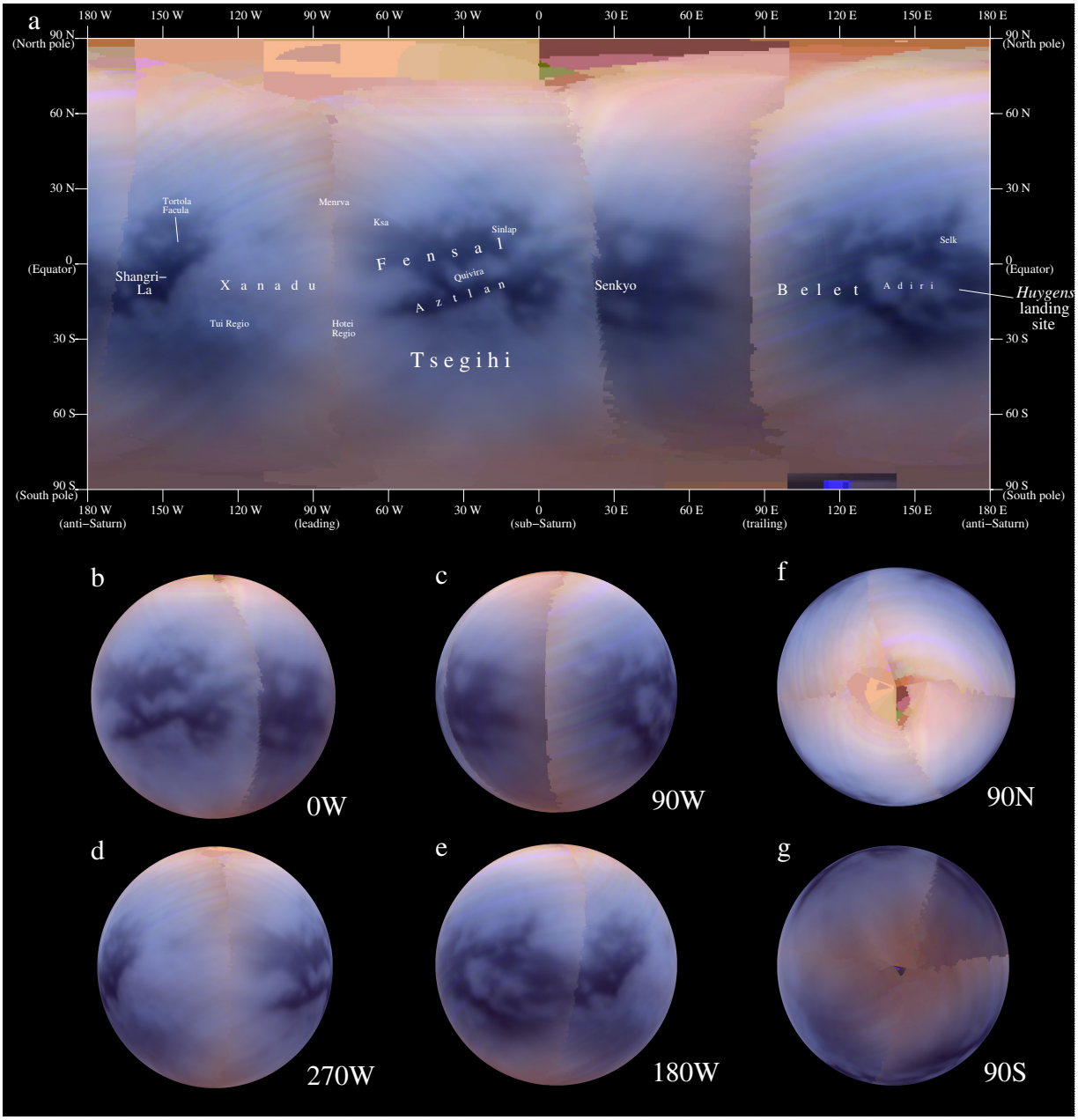

Figure 2.6: This is a corrected global map of Titan, using the same color/wavelength scheme as Figure 2.3, created using an algorithm to divide the haze out of the picture. In doing so, the surface features of Titan become more pronounced. Removing some of the haze also brings out the striping effects that are inherent to the VIMS-V system. When compared to Figure 2.3, we can see new areas emerge, such as the section south of Shangri-La in the west.

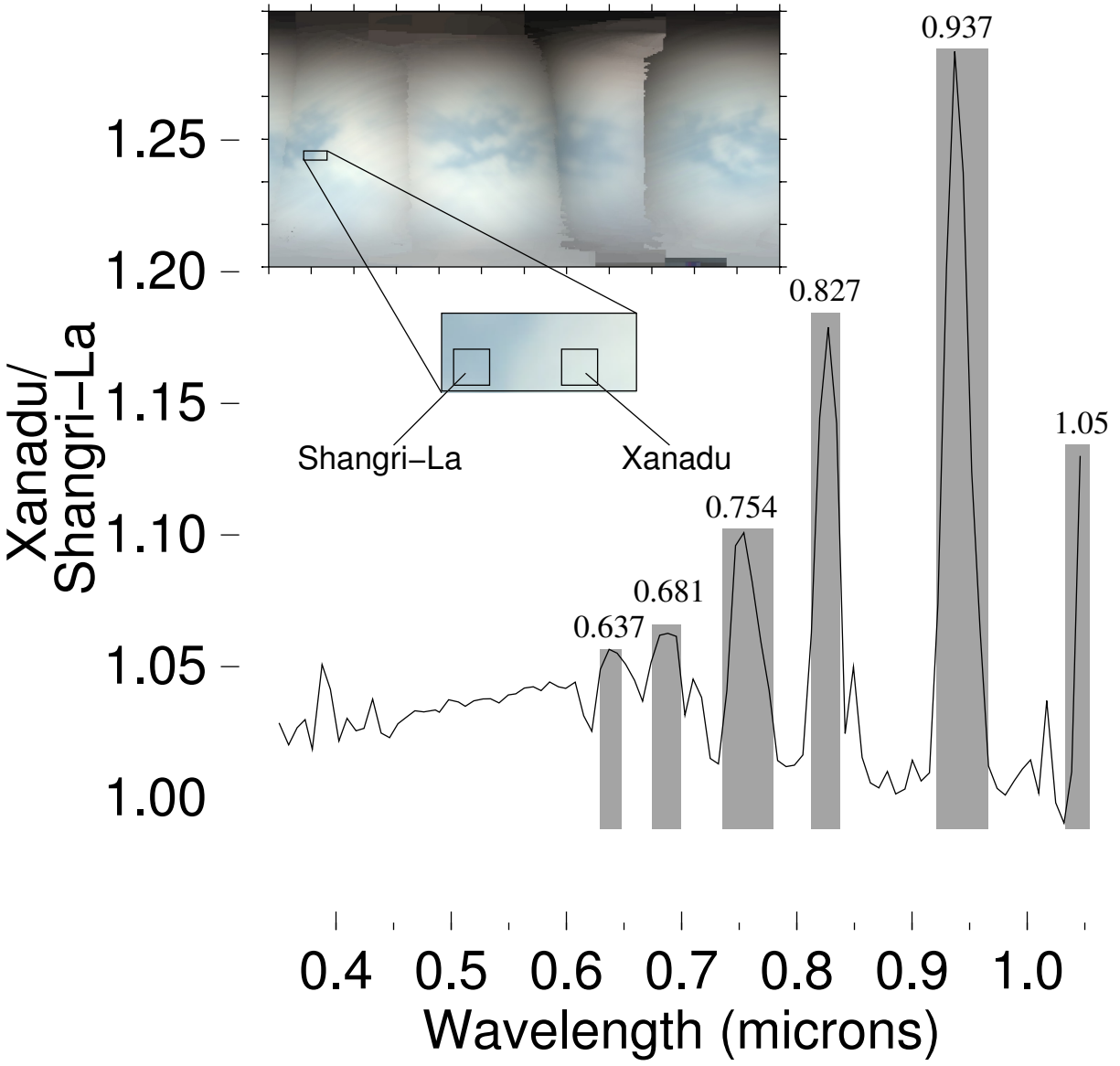

Figure 2.7: A spectral ratio graph, created using the T8 flyby, depicting the detected flux from a bright area relative to that in a dark area. It represents the average value of Xanadu divided by Shangri-La versus wavelength in microns with optical wavelength windows labeled and the range of the windows boxed. At wavelengths with strong atmospheric absorption, the flux coming from Xanadu and that from Shangri-La are about the same, barring a small difference owing to different haze reflection resulting from view geometry. Within spectral windows, where there is little or no methane absorption, the much higher surface reflectivity of Xanadu results in higher ratios. The ratio for longer-wavelength windows is progressively higher than that for shorter-wavelength windows because the ratio is less affected by scattering off of haze particles. Windows exist at 0.637, 0.681, 0.754, 0.827, 0.937, and 1.05 microns.

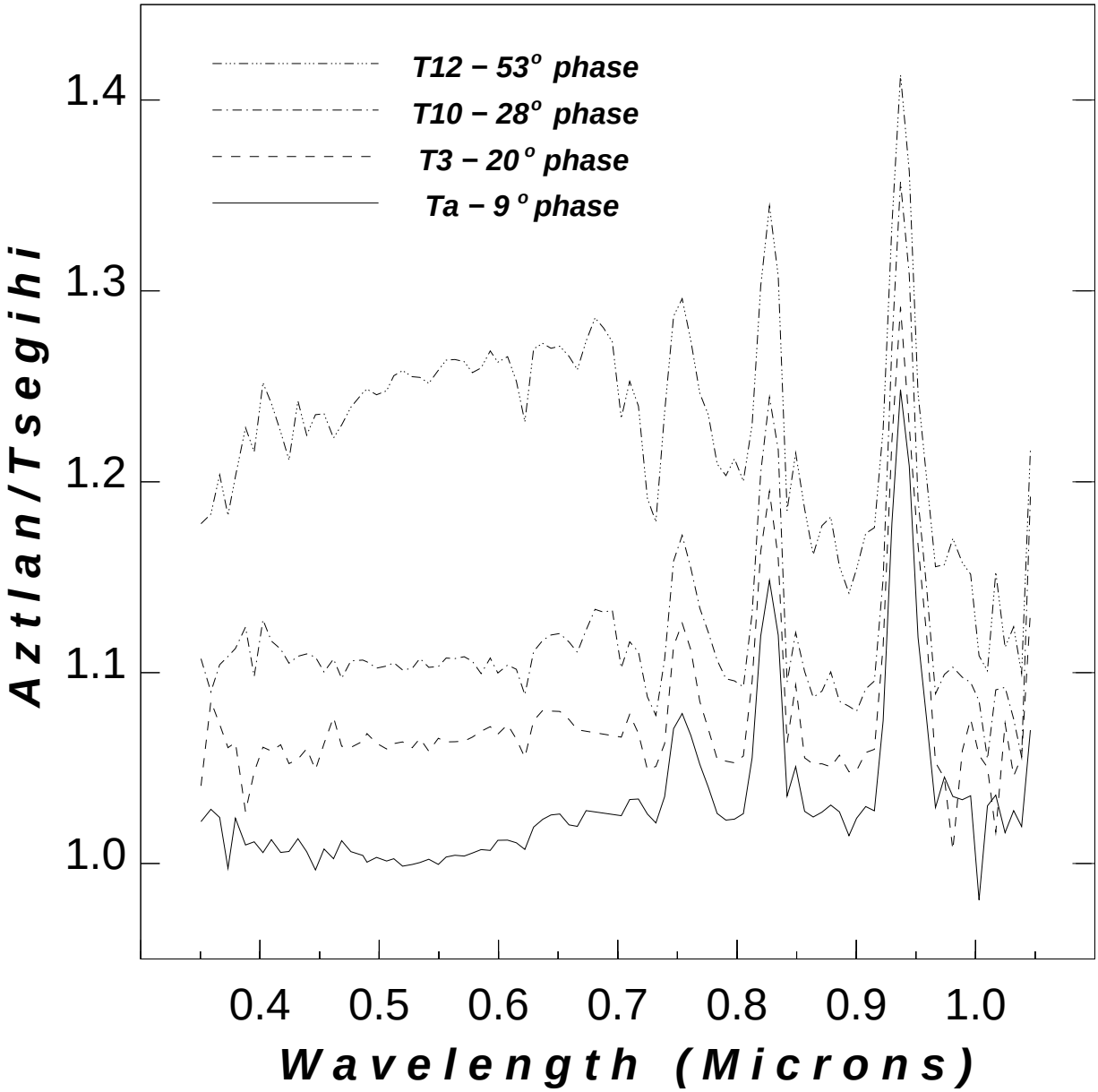

Figure 2.8: The four lines above are spectral ratios from the same region as Figure 2.7, T8 but at different phase angles, increasing from Ta to T12 by flyby number. The x-axis is wavelength in microns and the y-axis is albedo difference taken by dividing Xanadu by Shangri-La. As the phase angle goes up, the amount of striping noise in the spectrum goes up as is apparent by the rising and delinearization of the baseline. The height of each intensity peak remains unchanged above the baseline with increasing phase. The contribution from atmospheric scattering becomes more obvious in the plot of T12 in that lower wavelengths scatter more, raising the baseline.

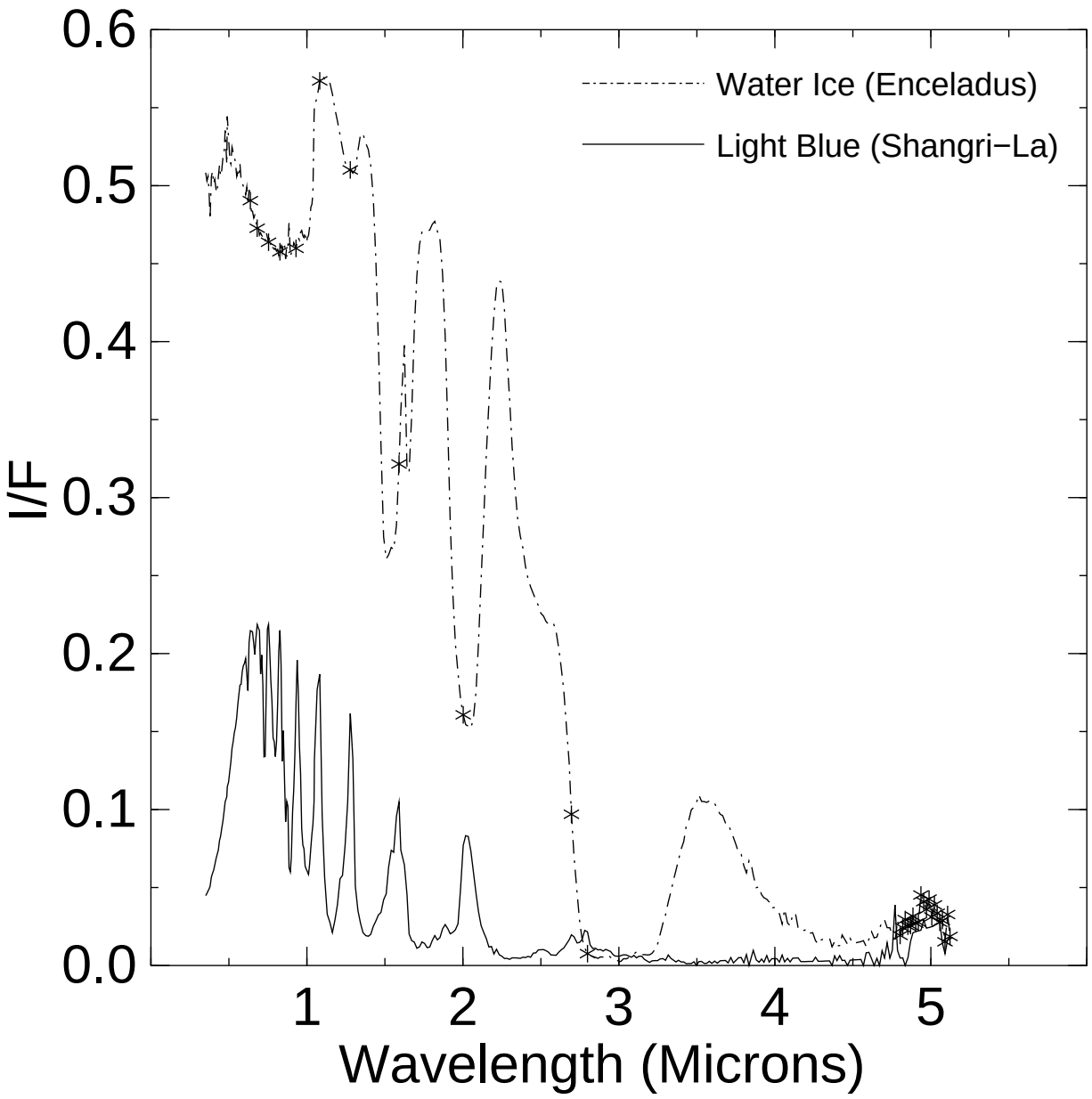

Figure 2.9: A comparison between water ice (for reference) and the visible light blue spectral type taken from northern Shangri-La. The stars in the Enceladus line represent the atmospheric windows in both the visible and IR. The overall gray appearance and greater relative brightness compared to the IR in the visible wavelengths in the Titan spectrum is broadly consistent with water ice, and also with various organic materials. Inversions from minima to maxima in these graphs imply wavelengths where a signal may be transmitted without being absorbed.

Chapter 3

Two Temperate Lakes on Titan

Graham Vixie[1], Jason W. Barnes[1], Brian Jackson[2], Sébastien Rodriguez[3], Stéphane Le Mouélic[4], Christophe Sotin[5], Paul Wilson[6]

1. University of Idaho, Department of Physics, 875 Perimeter Drive MS0903, Moscow, ID 83844-0903, USA

2. Department of Terrestrial Magnetism, Carnegie Institution of Washington, 5241 Broad Branch Road, NW, Washington, DC 20015-1305, USA

3. Laboratoire AIM, Université Paris Diderot - Paris 7/CNRS/CEA-Saclay, DSM/IRFU/SAp, Gif sur Yvette, France

4. Laboratoire Planétologie et Géodynamique de Nantes LPGN/CNRS UMR6112, Université de Nantes, Nantes, France

5. California Institute of Technology/Jet Propulsion Laboratory, 4800 Oak Grove Drive, Pasadena CA, 91109

6. Energyneering Solutions, 15820 Barclay Drive, Sisters, OR 97759, USA

Submitted to *Icarus* in March 2014.

Presented in 2012, at Titan Through Time; Unlocking Titan's Past, Present and Future, Editors: V. Cottini, C. Nixon, & R. Lorenz, Abstract #32

Email address: gvixie@vandals.uidaho.edu

Abstract

We have discovered two temperate lakes on Titan using *Cassini*'s Visual and Infrared

Mapping Spectrometer (VIMS). The lakes, named Sionascaig Lacus and Urmia Lacus, are located near 82°E, 41°S. Clouds were observed near this location on the T66 flyby and this latitude band showed many clouds during southern summer. The presence of lakes at the mid-latitudes indicates that surface liquid can accumulate and remain stable away from Titan's poles. We use three key characteristics to determine that these surface feature are lakes: morphology, albedo, and specular reflection. We first identified a lake surface by looking for possible shorelines with lacustrine morphology. Then, we applied an atmospheric correction that empirically solves for the surface albedo. Finally, we look for a specular reflection of the sky in a potential lake. Identifying lakes in the temperate region of Titan has implications for formation mechanisms such as clouds and rainfall or, in low elevation areas, percolation and subsurface flow. Our techniques can be applied to areas of Titan that lack RADAR coverage to search for mid- and low-latitude lakes in the future.

Keywords: Titan, Hydrology, Atmospheric

3.1 Introduction

Titan's atmosphere obscures the surface for the majority of visible-infrared wavelengths at which *Cassini* observes. In the methane windows where surface features are visible, scattering off of atmospheric haze particles can dilute the pure surface signal, reducing contrast and smearing out fine-resolution imaging. Scattering in the atmosphere also leads to ambiguities in the spectrum because the returned signal represents a superposition of atmospheric and surface contributions.

Lorenz (1994) surmised that lakes (as opposed to expansive oceans) may exist across the surface of Titan. The T16 *Cassini* RADAR synthetic aperture radar (SAR) swath over the north pole revealed many lakes, both dry and liquid-filled (Stofan et al., 2007).

The first south-polar lake observed on Titan was Ontario Lacus by the Imaging Science Subsystem (ISS) and VIMS (Brown et al., 2008; Turtle et al., 2009; Barnes et al., 2009a; Hayes et al., 2010; Cornet et al., 2012a,b). As *Cassini* continues to observe Titan, we have come to know that filled lakes on Titan are concentrated at the poles (Hayes et al., 2008), while all of the observed deserts and dunes are near the equator (Lorenz et al., 2006; Lorenz & Radebaugh, 2009; Le Gall et al., 2011, 2012; Rodriguez et al., 2013).

Boundary conditions on global circulation imply that volatiles build up at the poles (Tokano, 2009). Mitri et al. (2007) points to methane as being the transient liquid present in lakes. However, Stofan et al. (2007) states that liquid methane is thermodynamically stable anywhere on the surface of Titan. Clouds have been seen to concentrate around the 40°S latitude mark (Griffith et al., 2005; Roe et al., 2005b; Brown et al., 2010; Rodriguez et al., 2009, 2011; Turtle et al., 2011a) whereas no persistent surface liquids have been previously identified equatorward of 70°S or 53°N latitude. Rainfall has been shown to modify Titan's surface reflectance (Turtle et al., 2011b; Barnes et al., 2013a), and recent observations suggest that equatorial lakes may also exist (Griffith et al., 2012b).

Approximating a full atmospheric transfer function would allow correction of past, present, and future flyby data to reveal true surface albedos. The very first classical, numerical, high-fidelity radiative transfer models developed for Titan were by McKay et al. (1989b); Griffith et al. (1991) and Rannou et al. (1995) using Voyager and ground-based data analysis. During the two following decades, those teams and others continued to improve their models with a multitude of publications occurring right after *Cassini*'s arrival at Saturn and the Huygens landing (Rannou et al., 1997, 1999, 2000, 2003, 2010, 2012; Young et al., 2002; Cours et al., 2010, 2011; Bellucci et al., 2009; Coustenis et al., 2006; de Bergh et al., 2012; Hirtzig et al., 2013; Griffith et al., 2003, 2012a,b; Ádámkovics et al., 2004, 2007, 2009, 2010; Tomasko et al., 2005, 2008a,b; Keller et al., 2008; Schröder & Keller, 2008, 2009). Some alternative approaches were also developed, including a first-order scattering model (Rodriguez et al., 2006), empirical corrections for atmospheric

contribution and surface photometry (Cornet et al., 2012a; Le Mouélic et al., 2012b), and a 3D spherical Monte-Carlo modeling accounting only for haze scattering (Vincendon & Langevin, 2010). Each new increasingly efficient and complex model creates synthetic spectra to be compared with ground-based and *Cassini* data to explore unresolved or unknown regions of interest on Titan. Numerical radiative transfer models are powerful tools for Titan research, but they often are burdened with poorly constrained inputs and can require very long computation times.

Radiative transfer models can identify true surface albedo and characterize liquid regions with confidence, which have very low albedo in the infrared (Griffith et al., 2012b).

In this paper, we show and analyze high-quality observations from *Cassini* VIMS over the south mid-latitudes during the T66 flyby (*Cassini* Rev125, the spacecraft's 124th revolution around Saturn, January 28, 2010). We then construct a simple radiative transfer model for Titan using data from several Titan flybys and fit for surface albedos. The results of the model are then used to present evidence for two filled lakes near 40°S. This discovery shows that liquids can accumulate in the temperate regions, even in very localized areas, allowing us to place constraints on Titan's hydrological cycle. This work, unfortunately, cannot demonstrate that these features are long-lived.

3.2 Observations

The T66 flyby of Titan on January 28, 2010 at 22:28 UTC was a high-altitude (7487 km at closest approach) pass with ISS as the prime instrument at closest approach and VIMS riding along. There have been relatively few flybys of Titan with higher altitudes at closest approach (e.g. T9 - 10409 km, T66 - 7487 km, T67 - 7437 km, T72 - 8175 km, T73 - 7921 km, T75 - 10053 km, T78 - 5821 km, T80 - 29,415 km, and T81 - 31,131 km). Such flybys allow *Cassini* to attain greater coverage but results in coarser spatial resolution; however, the exposure time does not need to be reduced to very low values, which degrades the

signal-to-noise ratio.

VIMS performed high (3.7 km/pixel) and moderate (16 km/pixel) spatial sampling centered around Polaznik Macula, a dark feature at 79.6°E, 41.1°S originally named from ISS imaging. Additionally at closest approach, VIMS took one shorter and one longer exposure time cube. The cubes covering the Polaznik Macula area are listed with their characteristics in Table 3.6 in time order during approach. All of the relevant angles are recorded from as close to closest approach as coverage permits in the south-east portion of Polaznik. As *Cassini* neared closest approach, the values for emission and phase angles showed more variance than incidence angles, which changed more slowly due to Titan's slow rotation.

Figure 3.1 shows the global location of Polaznik Macula. The southeastern portion of Polaznik (located at 81.7°E, 41.4°S) stands out in VIMS, appearing to have a lower measured incident radiation over flux ($\frac{I}{F}$) than nearby features. Figure 3.2 shows an infrared color composite of the Polaznik Macula area, outlined in red, in contrast to its surroundings. The initial hypothesis is that this south-eastern area, outlined in dark blue in Figure 3.2, may represent a lake currently filled with liquid, now named Sionascaig Lacus. No RADAR SAR observations of the Polaznik Macula area currently exist; were such observations to be acquired, they would be of use to help to test the lacustrine hypothesis.

A second area just past the upper right boundary of the darkened area (also outlined in dark blue) shows a similar contrast to the lower right area and is also hypothesized to be a filled lake, now named Urmia Lacus. The other areas outlined in light blue show slightly brighter surface reflectivities and may be candidates for lakes, though they remain unconfirmed. The potentiality of the outlined areas to be filled lakes will be discussed in Section 4.

3.2.1 Atmospheric Correction and Surface Albedo Retrieval

We have implemented a partial, analytical, single-scattering atmospheric correction in order to derive surface albedo from measured $\frac{I}{F}$ in the VIMS 5 μm spectral region. We fit the model with a Levenberg-Marquardt least-squares minimization algorithm, upgraded from that in Barnes et al. (2009a). We define $\frac{I}{F}$ to be the total measured upward intensity divided by the incident solar flux. We make the assumption that contribution from photons scattered multiple times by the atmosphere is negligible – a good approximation at 5 microns (Rodriguez et al., 2006; Brown et al., 2008). The contributions to $\frac{I}{F}$ that we do consider are:

1. radiation reflected from the surface, wholly unscattered on its trip down through the atmosphere or back up,

2. radiation scattered upward by the atmosphere before reaching the surface, and

3. radiation scattered by the atmosphere downward into the surface, then reflected back upward by the surface and unscattered on its passage out of the atmosphere.

We calculate effective $\frac{I}{F}$ using the following equation:

$$\frac{I}{F} = A\Phi_s(i,e,\varphi)e^{-\tau(\alpha(i)+\alpha(e))} \tag{3.1}$$

$$+ \frac{\tilde{\omega}_0 p(\hat{\Omega}_0,\hat{\Omega})}{4\pi}\frac{\alpha(e)}{\alpha(i)+\alpha(e)}(1-e^{-\tau(\alpha(i)+\alpha(e))}) \tag{3.2}$$

$$+ A\frac{\tilde{\omega}_0}{4\pi}e^{-\tau\alpha(e)}\int_{\Omega'_+}\Phi_s(i,e,\varphi)\frac{\alpha(\theta')}{\alpha(i)-\alpha(\theta')}p(\hat{\Omega},\hat{\Omega}')(e^{-\tau\alpha(\theta')}-e^{-\tau\alpha(i)})\mathrm{d}\Omega'. \tag{3.3}$$

A is the surface albedo. $\Phi_s(i,e,\varphi)$ is the average surface phase function in terms of incidence, emission, and phase angles. τ is the total atmospheric extinction optical depth (scattering + absorption). $\alpha(i)$ is the incident airmass, 1 / cosine of the solar incident angle for the plane parallel case. Otherwise this is the number of normal atmospheres

traversed by the signal on the way down. $\alpha(e)$ is the emission airmass, 1 / cosine of the solar emission angle for the plane parallel case. Otherwise this is the number of normal atmospheres traversed by the signal on the way out. $\tilde{\omega}_0$ is the average single scattering albedo of atmosphere, given $\tilde{\omega}_0 = \frac{\int \tilde{\omega}_0 \mathrm{dz}}{\int \mathrm{dz}}$ where z is altitude. This effectively determines the relative importance of scattering and absorption. $\mathrm{p}(\hat{\Omega}_0, \hat{\Omega})$ is the average haze phase function for scattering from direction $\hat{\Omega}_0$ into $\hat{\Omega}$, defined as above. $\mathrm{d}\Omega$ is the solid angle in direction $\hat{\Omega}$, given by $cos(\theta)\mathrm{d}\phi\mathrm{d}\theta$, where θ and ϕ are the zenith and azimuthal angles, respectively.

This model improves on the work done by Rodriguez et al. (2006); Barnes et al. (2009a); Le Mouélic et al. (2012b); Sotin et al. (2012) by adding one additional scattering mode.

The objective is to look at the effective $\frac{I}{F}$ in areas of interest over a variety of phase angles on many different flybys to fit a curve for the unknown parameters in our empirical radiative transfer model, specifically the surface albedo, A. We fit our model using VIMS observations at different observing geometries, i, e, and φ, to measure the unknown parameters τ and $\tilde{\omega}_0$, as well as the surface albedo. The average surface phase function is calculated based on a Lambertian surface while the incident and emission airmasses are calculated based on an "orange rind" atmospheric model from Barnes et al. (2009a).

Our empirical approach assumes that the albedos of visually similar areas are constant, and fits for the albedo of each designated feature substrate type. We create masks over surface features on Titan by manually outlining regions that we assume to have the same albedos. The masks were made by manually outlining areas of interest in Titan flybys where the region was seen by VIMS. We categorize three different mask types from 595 data cubes in the T38, T64-70, and T72 flybys: bright albedo, which covers equatorially bright regions outlined in Barnes et al. (2007); dune albedo, which correlates to the dark brown areas in Barnes et al. (2007), Soderblom et al. (2007), Barnes et al. (2008), and Rodriguez et al. (2013); and lake albedo. Although the dune fields are known to not be the darkest albedo, we use this region for masking because VIMS has extensive coverage

of these areas.

Figure 3.3 shows the raw $\frac{I}{F}$ data points with our best-fit model over plotted. The raw data presented in each plot represent every pixel covered by our masks of each region. The mask coverage in the bright and dunes regions includes a wide range of viewing geometries, allowing for a much more accurate fit of the model. Lake observations have suffered because previously identified lakes exist at high latitudes, meaning VIMS coverage has been at high incidence angles. Each plot shows the large range of $\frac{I}{F}$ for a given incidence and emission angle, which in turn lends a great visual measure for the goodness of fit for the model. The reduced χ^2 value for our plots is 4.72, most likely due to our assumption that all bright and dune pixels are exactly the same albedo, which in turn increases variance. The bright and dune regions tend to decrease in $\frac{I}{F}$ with increasing incidence angle but stay somewhat constant with emission; changes in emission affect the dune region slightly more. The emission angle drives an increase in the lake region $\frac{I}{F}$ most noticeably above the 60° mark. There is also a subtle decrease in the $\frac{I}{F}$ at high emission and high incidence angles as pointed out by arrows in Figure 3.3c and d. All data points also vary in phase (not shown) which may explain some outliers in the plots. The phase in the best-fit model is the angle between each incidence and emission angle pair for each point, calculated by the model.

The haze phase function, $p(\hat{\Omega}_0, \hat{\Omega})$, is interpolated from a tabular look up based on Tomasko et al. (2008b)'s Table 1b, 5166 nm column. In the process of solving for surface albedo, we fix a minimum number of variables at their best-fit values based on the empirical $\frac{I}{F}$. The 5 micron value of $\tilde{\omega}_0$ calculated by our model under many different initial conditions is consistently within up to ∼23% of 1.0 (meaning that our empirical fit matches the Tomasko phase function). Thus the surface albedos listed in Table 3.6 were found using a fixed $\tilde{\omega}_0$ of 1.0. Our best fit 5 micron value for τ (0.042 ± 0.002) gives a 91% 2-way transmission $(1 - 2\tau)$ close to the one estimated by Sotin et al. (2012) using VIMS observations of solar occultations.

We can then apply our model to any VIMS cube, using the best-fit values for τ and $\tilde{\omega}_0$ along with any cube's observed $\frac{I}{F}$, incidence angle, emission angle, and phase angle to solve for the surface albedo of each pixel making the hypothesis that the atmospheric properties have not changed during the interval of observations. Next, we classify features based on observed boundaries and the model's value for each surface feature type (*i.e.*, bright, dune, or lake). We use this method on the T66 flyby, specifically the area shown in Figure 3.2, to classify our candidate lake features.

3.3 Interpretation

3.3.1 Sionascaig and Urmia

We explore three lines of inquiry to evaluate the lake hypothesis for Sionascaig Lacus and Urmia Lacus: morphology, surface albedo, and specular reflection.

Morphology

The morphology of a large surface feature can be judged to be lacustrine or non-lacustrine by comparing it to other known and verified lakes on Titan, such as Ontario Lacus (Barnes et al., 2009a; Wall et al., 2010; Cornet et al., 2012a). The boundary of the bright dark disparity around each candidate feature is continuous, lobate, and relatively similar to previously identified VIMS, RADAR, and ISS lakes. Comparisons to Ontario Lacus can be made looking at Figures 3 and 6 from Barnes et al. (2009a), Figure 1 from Wall et al. (2010), and Figures 1 and 4 from Cornet et al. (2012a). The boundaries of the features outlined in dark blue in Figure 3.2 are consistent with these comparisons for shoreline in the VIMS data. The substrate dichotomy between dark and non-dark is similar to VIMS observations of Kraken Mare and Ligeia Mare as well as other nothern lakes as seen in Figures 4, 7, and 10 from Sotin et al. (2012). The lobate boundaries are akin to VIMS 5 micron observations of those north polar lakes that do not exhibit evaporite around their

shorelines seen in Figures 1 and 2D, F of Barnes et al. (2011b). Unfortunately, no future RADAR flybys are planned for the Polaznik Macula area in the Solstice mission, so a greater spatial sampling analysis of morphology here is unlikely.

Albedo

Liquid hydrocarbon surfaces have a very low albedo in the infrared as liquid methane and ethane are strong absorbers in this wavelength window (Clark et al., 2010). This study is not aiming to infer anything about the composition of the lakes as the spectra are too noisy for analysis in this regard, but only to extract the albedo at one wavelength– enough to be diagnostic for the presence of liquids. The surface albedo can be read off of an empirically atmospherically corrected map generated by our single-scattering model to compare the albedo to that for known bodies of liquid. The model, as described in the previous section, reports surface albedos within the dark blue areas of Figure 3.2 of 0.0070-0.0081 at 5 microns. Specifically, the surface albedo of Sionascaig Lacus is 0.0070 and Urmia Lacus is 0.0081. These values are consistent with those measured albedos for Kraken Mare (0.0114) and Ligeia Mare (0.0050-0.0089) by our model. These values for Kraken Mare and Ligeia Mare are lower than described in Sotin et al. (2012) but remain consistent because the additional scattering modes accounted for in our model lower the albedo by subtracting the contributions from haze scattering. Our value for lake albedo is also lower but within the error bars of Griffith et al. (2012b)'s 5 micron lake albedo of 0.02 ± 0.01. The central area in Polaznik Macula, northwest of Sionascaig Lacus, has a 5 micron albedo of 0.0150, similar to that of the dunes but lower than the dune albedo for 1.08 microns of 0.03-0.08 in Griffith et al. (2012b), and lower still than the ISS solid surface dark albedo of 0.05 from McCord et al. (2008). The bright region surrounding Polaznik Macula has a 5 micron surface albedo of 0.0298. Figure 3.4 shows the areas of Polaznik Macula from T66, including Sionascaig Lacus and Urmia Lacus, labeled by their albedos at 5 microns.

Specular Reflection

Our final test to evaluate whether these features are lakes is the observation of a specular reflection. Specifically, we are looking for illumination of the lake by the sky and not by the Sun (Figure 3.5). The albedo, in this case, of the lake in question is a measure of the specular reflectivity. A specular reflection should produce a higher $\frac{I}{F}$ value than the non-specular surface albedo expected for a liquid feature on Titan. Equation term 3.3 accounts for the contribution of such a specular reflection from the sky.

The $\frac{I}{F}$ should increase as VIMS views Polaznik Macula from increasing emission angles according to calculations by Soderblom et al. (2012). This increase can be seen when comparing model $\frac{I}{F}$ predictions with and without Equation part 3.3 in Figure 3.6. From this figure, the difference in $\frac{I}{F}$ is most apparent when the emission angle exceeds 60°. Only two of the observations that we have of Polaznik Macula were acquired with emission angles in this range, and unfortunately, these observations are coarse-resolution (Table 3.6).

If lake candidates indeed exhibit this specular reflection, then the model should report a specular reflectivity of 1. However, in our analysis, the model reports a reflectivity of 0.44 ± 0.13 for Kraken Mare and Ligeia Mare at 5 microns, leaving the interpretation somewhat ambiguous even in the case of these large seas. Since our model returns a specular reflectivity below 1, our specular reflection test is inconsistent with both a lake interpretation and that of a solid surface at Kraken and Ligeia. Since we have already seen specular reflections of the sun in Kraken Mare (Stephan et al., 2010), our results may indicate surface roughness (waves), floating non-specular material (pond scum), or suspended sediments.

Present data for Polaznik Macula are as yet insufficient for such a test as views of this area in flybys other than T66 are at a global scale. Working in the 2 micron window or a flyby over the Polaznik Macula area where the temperate lakes are near the terminator would provide more atmospheric illumination and could potentially disambiguate these results. However, programming the model to correct the 2 micron window is beyond the

scope of this paper, and as such, we leave it for future work.

3.3.2 Other Candidates

Finding two lakes in the mid-southern-latitudes inspires a search for more lakes that may exist in this temperate latitude band. We surveyed the mid-southern-latitudes for lacustrine morphology and low albedo surface features across *Cassini* flybys Ta through T72 (the Prime mission through Equinox) and found 10 other candidates. As coverage is at a coarser resolution in the mid-latitudes than at the equator and poles, candidates spanning more than a single pixel are rare.

Seven of the 10 candidates are distinct temperate dark surface features exhibiting possible lacustrine morphology with our model. Evaluating these features we find that the measured surface albedo is higher than what is expected for lake (black arrows in Figure 3.7) in each case. The features from T70 are located near 142°E, 42°S while the features from T76 are located at 12°E, 36°S. The remaining two candidate features can be found in T58 and are located near 27°E, 44°S and 59°E, 46°S. A very plausible explanation could simply be that the sampling is too coarse and that the potential lake feature only exists in a few pixels or is even smaller than one pixel. In this case, the average $\frac{I}{F}$ as calibrated from *Cassini* for each pixel may be higher than that for a potential lake endmember. That is to say, at lower resolution there may be a geographic mixing between lake and surface albedo, resulting in a higher averaged albedo. Confirmation of pixel-scale lakes with VIMS is outside the scope of this study, but may be possible in the future by comparison with RADAR coverage, for example.

The other 3 cases having low albedo exhibit no morphology that would suggest liquid surface features (white arrows in Figure 3.7). In this case, the ground may be covered by some low albedo spectral element, may be damp, or the sampling resolution may be too coarse. Turtle et al. (2011b) shows an example of transient liquid darkening the surface after a precipitation event. If the low albedo feature is present in several flybys, then an

explanation may be similar to the tropical lake proposed in Griffith et al. (2012b) and would require further analysis and comparison.

The Griffith et al. (2012b) observation of possible tropical lakes provides a good test for our analysis approach. Figure 3.8 shows two subfigures of VIMS data cube CM_1567239055_1 from Griffith et al. (2012b), shown side by side with other depictions of the same data cube at the same wavelengths. The comparison uses a different contrast stretch in order to better define the morphology of surface features present as per our first test. As the stretch becomes more moderate between Figure 3.8b and Figure 3.8c, the "dark oval" (Griffith et al., 2012b) area becomes less distinct. The abatement of the "dark oval" is more apparent at 2 microns (as seen in the comparison of Figure 3.8e and Figure 3.8f) than at 1.3 microns. Figure 3.9 shows the area in the 5 micron wavelength after correction by our model using VIMS data taken from the T35 flyby of Titan; the 5 micron data were not used by Griffith et al. (2012b). Running our atmospheric correction on the lacustrine candidate area described in Griffith et al. (2012b) yields a surface albedo value of 0.0090 on the single darkest pixel in the area, which is consistent with the rest of Titan's lakes. However, the values of the surface albedo in the rest of the "dark oval" area are much higher, ranging from 0.0107 to 0.0167 with an average near 0.0137, which more closely matches the dune region surface albedo. This surface feature also does not exhibit any lacustrine morphology: lack of a distinct shoreline boundary when viewed at 5 microns is similar to the areas pointed to by white arrows in Figure 3.7.

We caution, though, that we are not able to rule out the presence of surface liquid in the "dark oval" in the Griffith et al. (2012b) with our methodology. We note that this candidate does not possess our first or second characteristics. Hence, we would not yet consider the "dark oval" to be a lake with present data. In particular, lacustrine interdunes of the sort sometimes seen within longitudinal sand seas on Earth would not be resolved by current VIMS data and thus cannot be ruled out.

3.4 Discussion

While we cannot determine the longevity of these temperate lakes without viewing Polaznik Macula in additional flybys, we can make rough estimates and comment on the sources and impact of these lakes and the implication of their presence at those latitudes on Titan's global climatology. In the T66 flyby, which we used to identify the lakes, clouds are visible nearby to the southeast and southwest of Polaznik Macula. Throughout Titan's cloud history, clouds are both predicted and observed in southern mid-latitudes during summer, some even specifically around 40°S (Roe et al., 2005b; Rodriguez et al., 2009, 2011; Brown et al., 2010). Some clouds have recently been observed around 40°N as well after equinox (Rodriguez et al., 2011; Turtle et al., 2011a). The presence of clouds around Polaznik Macula (41.1°S) suggests at least the possibility that the area could be either a source or a sink for the moisture in the 40°S clouds.

While only the features outlined in blue in Figure 3.2 are filled with liquid, the areas outlined in light blue are dark enough to suggest wetting. Specifically the light blue area in the western-most area of Polaznik Macula may be an analog to a muddy or marsh-like feature having a surface albedo of 0.0080, though there is no morphological evidence to support the claim. Barnes et al. (2009a) saw similar dark deposits associated with Ontario Lacus, and suggested that they were mudflats. The other light blue areas, though of low albedo, span too few pixels from which to conclude anything definitively.

The surface area of Sionascaig Lacus can be estimated from Figure 3.2 to be on the order of $\sim$5000 km^2. Assuming that the slope of Sionascaig's lakebed is similar to the slope of Ontario Lacus (Hayes et al., 2010, 2011), then Sionascaig Lacus would have a volume of 920 km^3 with a max depth of 390 m for a slope of 2.7×10^{-3} and 170 km^3 with a max depth of 70 m for a slope of 5×10^{-4}. We prefer a more shallow slope with a lesser maximum depth. We argue that this is the case due to similarity between Sionascaig Lacus and Ontario Lacus with analogy to the shallow slopes seen in Google satellite images of San Francisco Bay as the water's opacity does not obscure the ground for the preponderance of

the bay (visual analog only). An alternative to shallow slopes may be that the relatively brighter albedo artifacts seen by VIMS within Sionascaig's boundary (Figure 3.2) are suspended particles in the liquid. We then use the smaller volume estimate for Sionascaig Lacus and 453.4 $\frac{\text{kg}}{\text{m}^3}$ for the density of liquid methane to estimate the total methane mass to be 7.8×10^{13} kg. Griffith et al. (2005) estimates the total cloud mass for the area bounded by 37°S to 40°S and 0°W to 200°W to be on the order of $10^{10} - 10^{14}$ kg, with varying conditions. A possible transport-process for lake liquids on Titan, in addition to rainfall, is percolation or subsurface flow in low-elevation terrain and/or from a high alkanifer (Hayes et al., 2008; Cornet et al., 2012a). A larger liquid volume in the lake than in the clouds would be supportive of a subsurface alkanifer. The alkanifer hypothesis is also supported by Sotin et al. (2012).

If we assume that Sionascaig is a methane-dominant lake, then we can use the evaporation rate of methane on Titan and the resulting rate of change in lake surface level (Mitri et al., 2007) to compare the total methane mass of the lake to that in the methane inventory of the 40°S clouds from Griffith et al. (2005). Next, we consider the evaporation rate of a methane-dominant lake to be $0.3 - 5.0 \times 10^3$ $\frac{\text{kg}}{\text{m}^2\text{yr}}$ (Mitri et al., 2007), assuming that it is similar to that at the north pole. A methane-dominant lake (with methane mole fraction ≥ 0.95) the size of Sionascaig Lacus would be expected to evaporate in 3-4 years, assuming no replenishing sources. An ethane-dominant lake (with mole fractions of methane - 0.35, ethane - 0.60, nitrogen 0.05) would have an evaporation rate of 1.5×10^3 $\frac{\text{kg}}{\text{m}^2\text{yr}}$ and would evaporate in $\sim$10 years under similar conditions. Mitri et al. (2007) also expects lake surface levels to change by $0.3 - 10$ $\frac{\text{m}}{\text{yr}}$ along with shoreline recessions of hundreds of meters to tens of kilometers. If we consider the Polaznik Macula area to be the exhibited shoreline recession of Sionascaig Lacus, on the order of $\sim$150 km, then the recession process would require <2 years for methane and $\sim$5 assuming an ethane-dominant composition to reach the current status. If, upon later observation, Sionascaig Lacus has exhibited either no shoreline change similar to Ligeia Mare (Sotin et al., 2012) or no (Cornet et al.,

2012b) or minimal shoreline recession similar to Ontario Lacus (Hayes et al., 2011; Turtle et al., 2011c), then the lake's liquid must necessarily be supplemented by another source, or dominated by ethane.

Lorenz et al. (2013) provides a global topographic map of Titan that extrapolates known elevations into areas not yet observed by RADAR. This paper places Sionascaig Lacus in a relative topographic low: around -500 m according to Lorenz et al. (2013), Figure 3.

Although filled lakes absorb heavily in all of VIMS, ISS, and RADAR wavelengths, the average topography of a lake area can be extrapolated through correlation of RADAR Digital Terrain Models (DTMs). Hayes et al. (2013) find that lake levels are similar in elevation over a large distance, supporting the alkanifer hypothesis. We can also determine relative topography by comparison of RADAR imagery to VIMS or ISS data. This method is accurate for regions closer to existing RADAR coverage. We could more accurately determine the relative elevation of the Sionascaig Lacus area with a RADAR pass over Polaznik Macula by looking at the surrounding altimetry and identifying any channels nearby to suggest drainage. In addition to altimetry, SAR coverage of the area could be a strong complement to the VIMS coverage in the morphological identification of these temperate lacustrine features.

3.5 Conclusion

Sionascaig Lacus and Urmia Lacus are two newly discovered lakes within the temperate latitudes of Titan. Both surface features are resolved, appear dark, continous, and lobate (lacustrine morphology) in VIMS, and our best-fit model places their surface albedos at 0.0070 and 0.0081, respectively, similar to confirmed seas such as Kraken Mare and Ligeia Mare. Our single-scattering model numerically reports best-fit values for surface albedo, allowing for identification of lakes on Titan lacking RADAR coverage. Unfortunately, we

cannot rule out these features being transient.

The majority of the known lakes and seas on Titan are located near the poles. Lakes have been suggested in the tropical zone by Griffith et al. (2012b), but that candidate does not meet the criteria applied in our survey. Clouds have been recorded accumulating in the southern mid-latitudes (Griffith et al., 2005; Roe et al., 2005b; Brown et al., 2010; Rodriguez et al., 2009, 2011; Turtle et al., 2011c) and areas near 20-30° S latitude have been darkened by rainfall but later brightened after evaporation (Turtle et al., 2011b; Barnes et al., 2013a). Stable temperate lakes would affect total rainfall, liquid accumulation, evaporation rates, and infiltration. Topographic lows may also allow percolation from subsurface reservoirs (Hayes et al., 2008; Cornet et al., 2012a). Our interpretations of Titan's hydrologic cycle are constrained further with the inclusion of non-transient temperate lakes such as Sionascaig Lacus and Urmia Lacus. With additional VIMS and RADAR coverage, Sionascaig Lacus would make a great candidate for future studies regarding lake filling, evaporation rates, and stability.

The discovery of potential lakes outside of the polar areas suggests that the mid-latitudes would be good targets for several instruments on *Cassini*. Although VIMS has complete global coverage of Titan, the majority of the mid-latitudes have only been imaged at a very coarse resolution with the one exception being T66, studied here. The mid-latitudes look "bland" and, when combined with coarse sampling resolution, smeared, and cause lacustrine candidates to often span less than a single pixel. As the Solstice tour continues, the improvement of the survey of mid-latitudes will be interesting for the discovery of new lacustrine candidates and for the monitoring of the potential shoreline evolution of Sionascaig Lacus and Urmia Lacus. The cross referencing of areas, if coverage exists, between VIMS, ISS, and RADAR could help to disambiguate the nature of these surface features.

3.6 Acknowledgements

The author acknowledges funding by grant #NNX09AP34G to JWB from the NASA Outer Planets Research Program.

VIMS Cube	Best Spatial Sampling (km)	Range (km)	Incidence(°)	Emission(°)	Phase(°)	Exposure Time (ms)
CM_1643417608_1	16.5	32672	45	46	39.5	120
CM_1643416678_1	14.0	27745	46	41	43	120
CM_1643414307_1	8.24	15802	48	46	38	120
CM_1643413825_1	7.13	13616	51	46	38	120
CM_1643413339_1	5.81	11588	51	44	39	120
CM_1643412870_1	4.82	9881	52	36	41.5	120
CM_1643412398_1	4.00	8530	49	22	50	120
CM_1643411921_1	3.74	7691	50	17.5	59.5	140
CM_1643411254_1	3.82	7637	51	31	82.5	40
CM_1643411453_1	3.66	7509	51	23	74.5	120

Table 3.1: Characteristics of Relevant T66 VIMS Cubes: These cubes from the T66 flyby form the composite image (Figure 3.2) in which we outline Sionascaig Lacus and Urmia Lacus. The cubes are listed in order of approach as seen from the best spatial resolution and range columns. All of the relevant angles are recorded from either in Sionascaig Lacus or as close as the cube covers to that area. As *Cassini* flies by at closest approach, the values for emission and phase show more variance than incidence.

Parameters	Model Result (error)
τ	0.0428 ($\pm$0.002)
$\tilde{\omega}_0$	1.0 (fixed)
Bright Region	0.0322 ($\pm$0.0005)
Lake Region	0.01
Dune Region	0.0158 ($\pm$0.0005)

Table 3.2: This table lists the free parameters being best-fit by the model run at 5 microns along with their results and error where available. Each region entry represents a surface albedo value for the respective substrate.

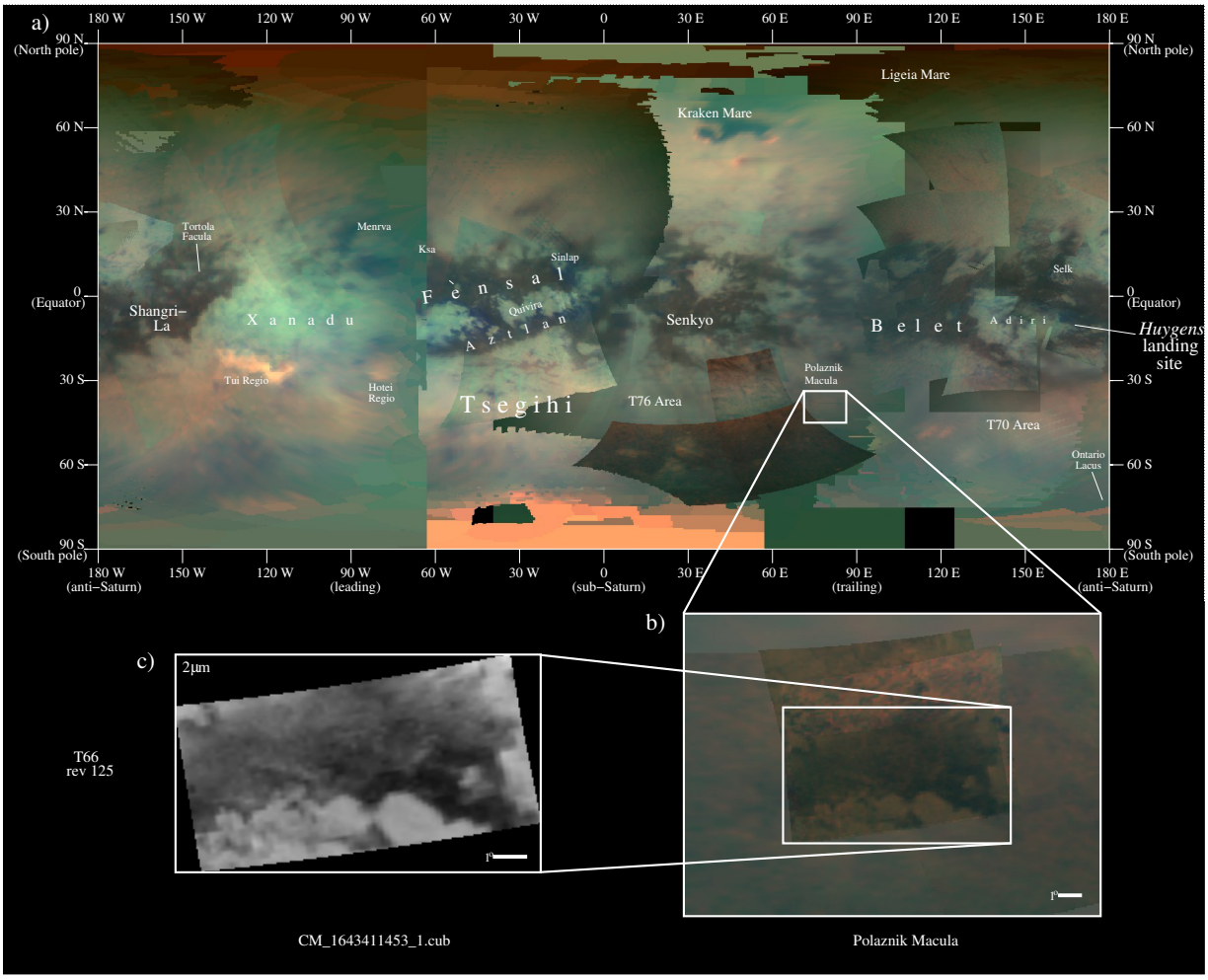

Figure 3.1: This cylindrically projected global map is annotated with several points of interest and significant features of Titan's surface. The false color composite (a at top) uses 1.28 μm as blue, 2.00 μm as green, and 4.8-5.2 μm as red. Fewer images were chosen to minimize the number of seams while maximizing global coverage rather than simply using all of the highest resolution cubes available. Polaznik Macula is of particular interest here and the area has been enlarged in subfigures (b) and (c). The first enlarged composite image in subfigure (b), using the same wavelength combination as (a), is part of the T66 (Rev25) flyby of Titan by the *Cassini* spacecraft, built from the cubes listed in Table 3.6. Another box is drawn around the macula itself and enlarged again to show a single 2 micron image in subfigure (c) from T66, emphasizing the contrast of the features within.

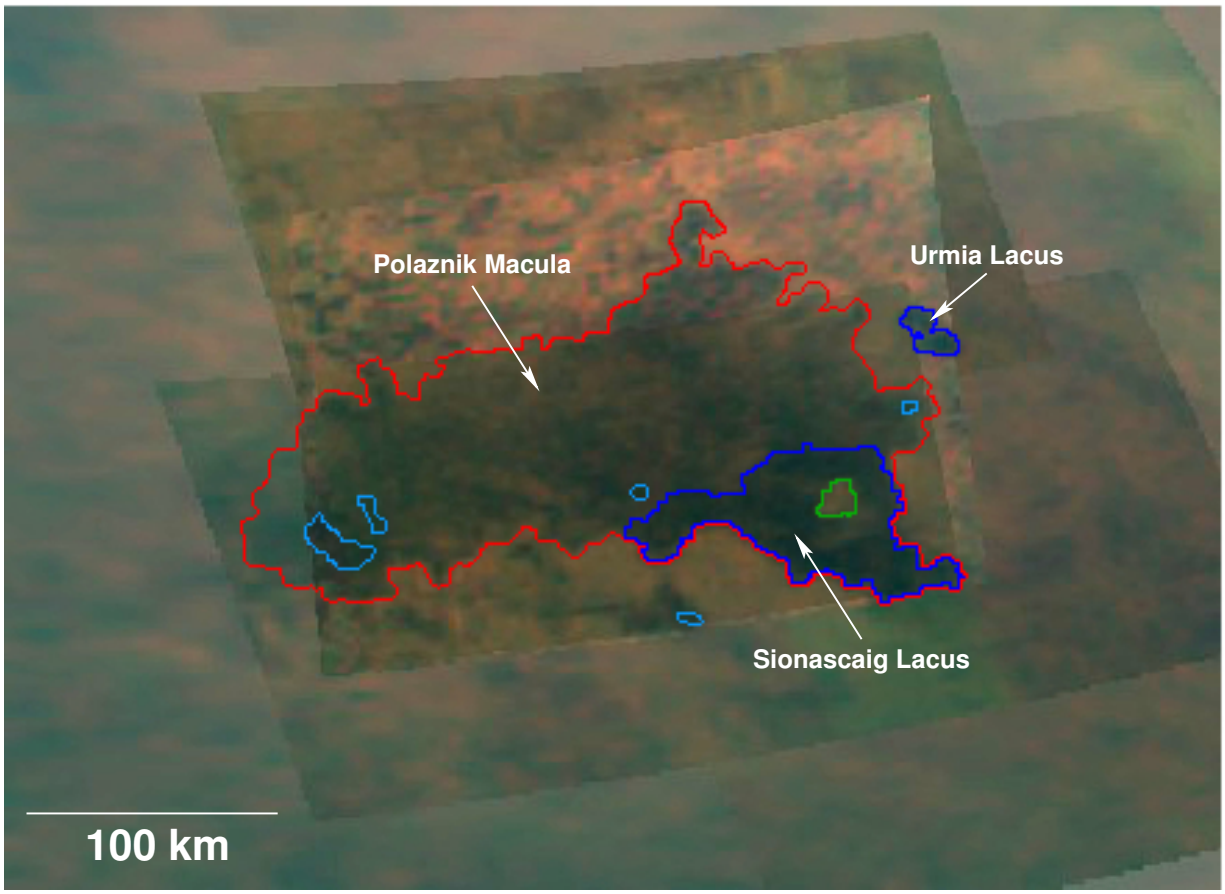

Figure 3.2: Polaznik Macula is the large, dark area central to the figure outlined in red. The dark blue encircled areas represent the new lakes positively identified in the T66 flyby via observed lake-like morphology and surface albedo less than 0.010 (the criterion determined from the well known liquid-filled Kraken Mare and Ligeia Mare). The light blue areas represent lake candidates still under scrutiny, as they have surface albedos less than 0.010 but lack definite lacustrine morphology. The green circle marks an island within Sionascaig Lacus.

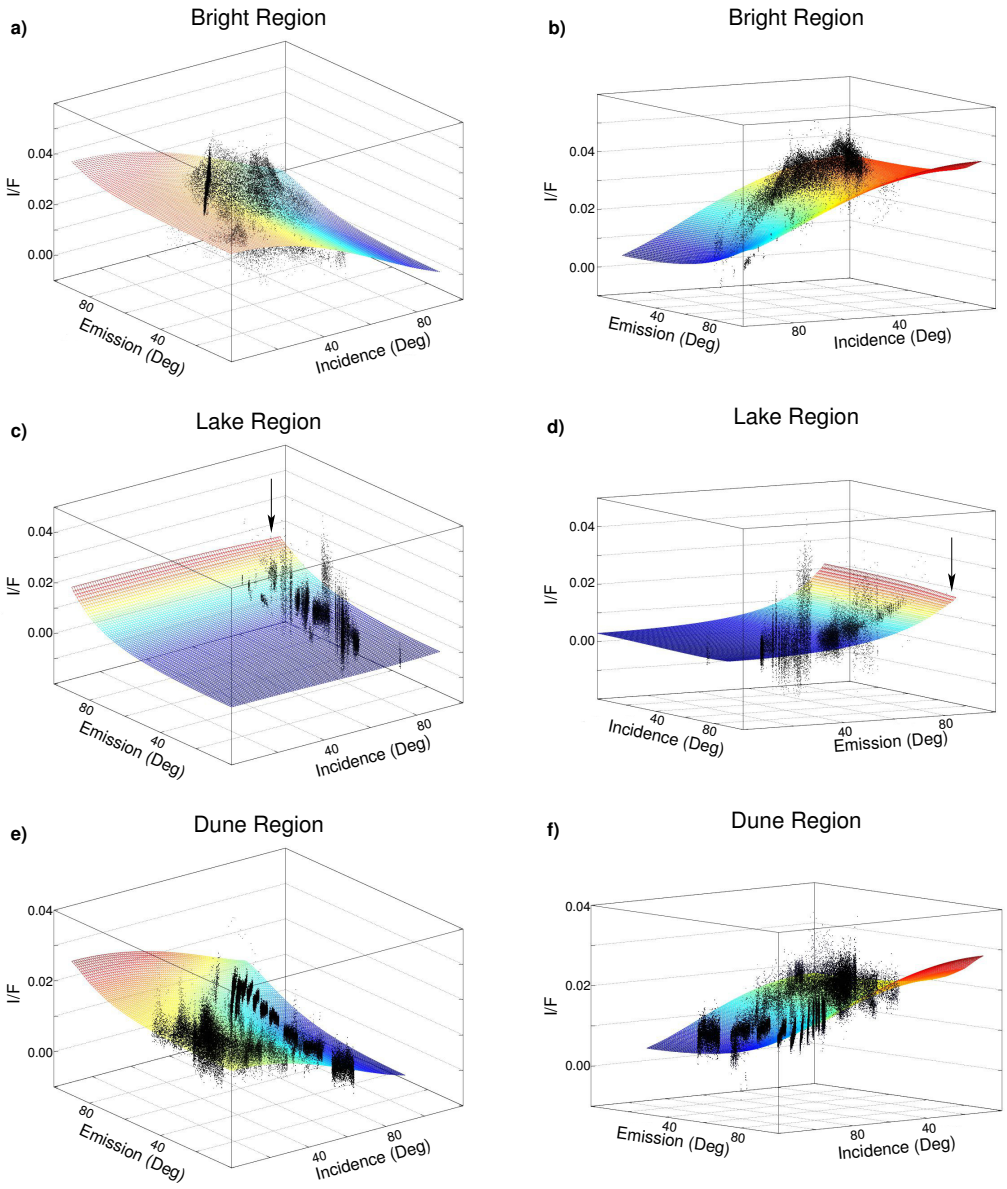

Figure 3.3: The six subfigures above show our model plotted along with the raw data for the areas covered by our masks from the VIMS dataset with $\frac{I}{F}$ versus incidence and emission angles. The phase values for the model are calculated to be the average of the sum of incidence and emission as to imitate the raw data's phase values. Each row presents different views of the same 3D plot. (a) and (b) represent the equatorial bright regions for which *Cassini* has a wide range of viewing geometries. This inclusive coverage allows for a very good model fit in the bright region. Parts (c) and (d) show the lake region. VIMS coverage of lake areas is somewhat limited in terms of viewing geometries as most of the raw data is at high incidence. The arrow indicates a subtle decrease in $\frac{I}{F}$ at high incidence. (e) and (f) quantitatively describe the dunes region which also has a very wide range of viewing geometries in VIMS allowing for a reasonable fit.

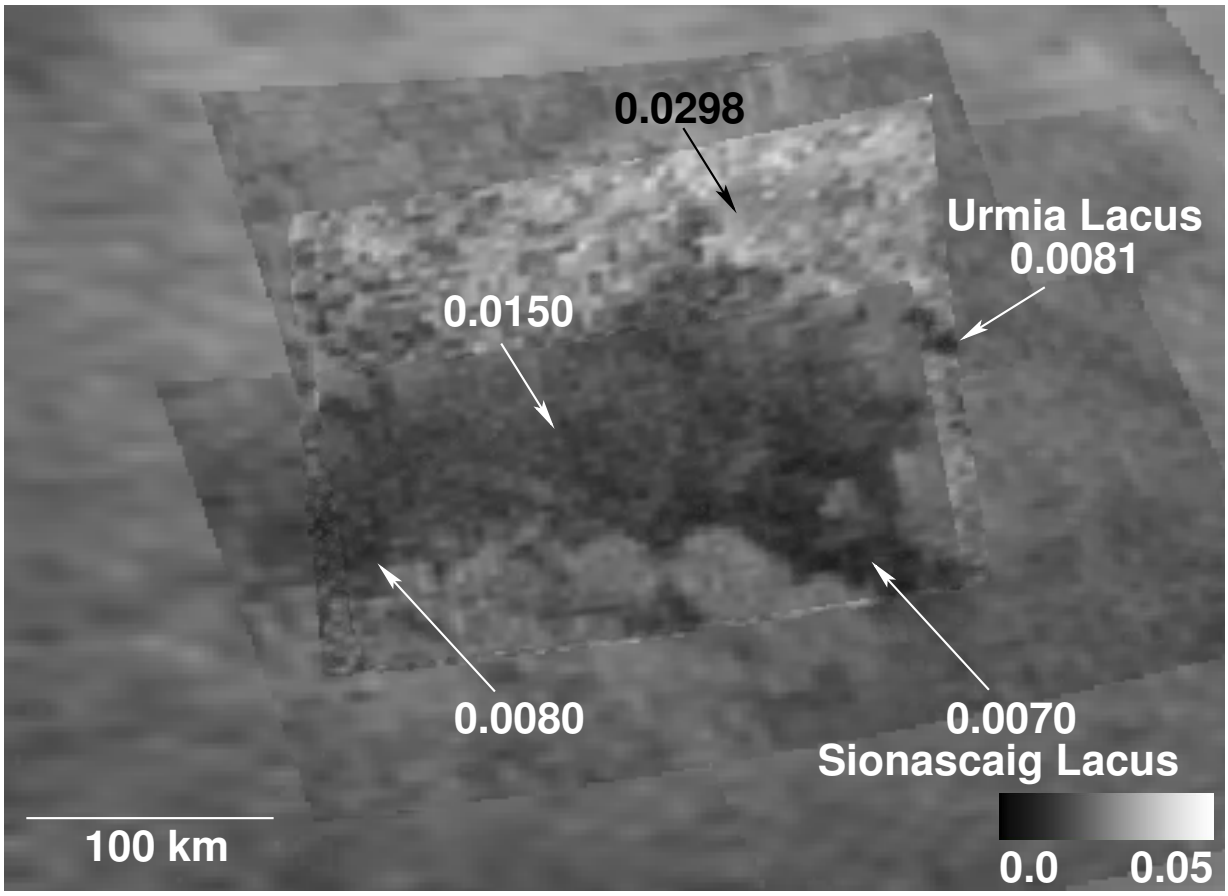

Figure 3.4: This figure shows the surface albedos of the different regions considered in this paper. Our model was run on this composite cube from T66 to empirically solve for the surface albedos, fixing the other free parameters of our model, previously determined over test regions (τ and $\tilde{\omega}_0$). The northern bright region has a value of 0.0298 $\pm$ 0.0005. The central area of Polaznik Macula has a surface albedo similar to dunes at 0.0150 $\pm$ 0.0005. The two lake areas as well as an area in the west showing no lacustrine morphology all show low surface albedo values similar to Ligeia Mare and Kraken Mare between 0.0070 and 0.0081. The area in the west could plausibly get its low albedo from wet ground.

Figure 3.5: This photograph, taken in flight overland east of Hudson Bay, QC, CAN, shows specular reflections of the sky in several lakes. The dark areas are land; the bright areas are the lakes. This is the kind of specular reflection that we are looking for in Titan's lakes, rather than a direct reflection of the Sun on the liquid as in Stephan et al. (2010).

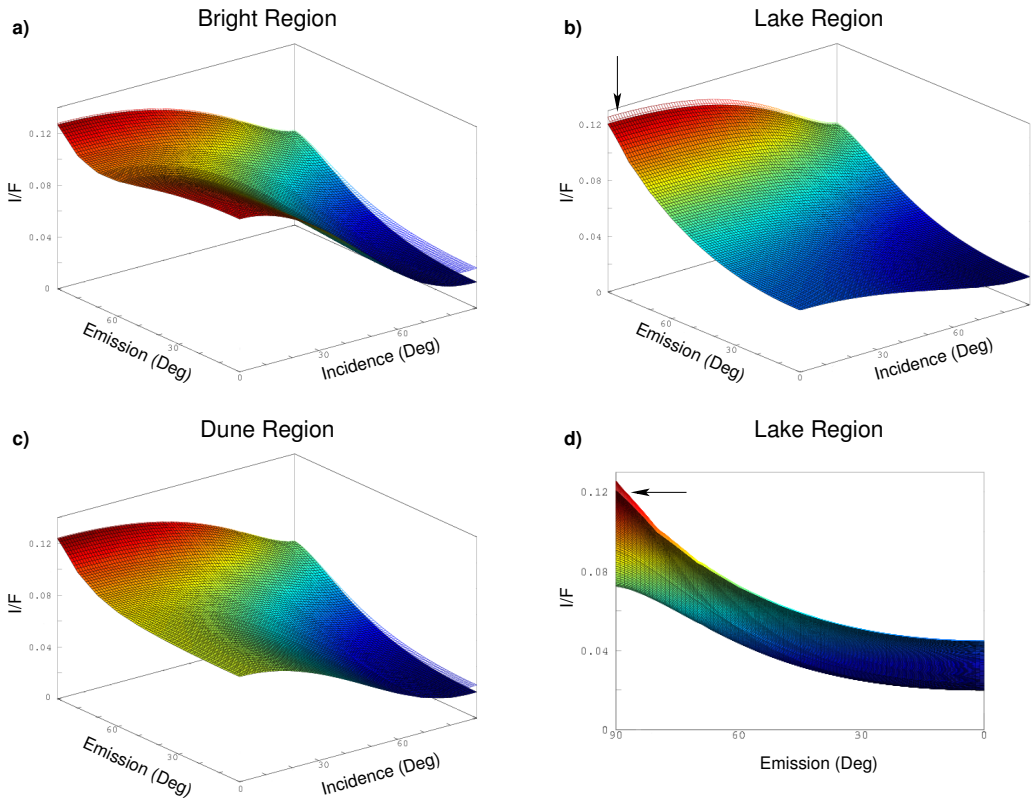

Figure 3.6: The solid color surface plot in each subfigure represents our model's prediction of $\frac{I}{F}$ as a function of the incidence and emission angles with only Equation terms 3.1 and 3.2. The clear mesh plots in each subfigure represent our model with the addition of Equation term 3.3, the sky illumination of the surface. The addition of this final term results in an increased brightness in each terrain type. Plots (a) and (c) show little change in surface albedo except at high incidence and low emission where there is much sky brightening. Plot (b) shows an incidence-independent increase in surface albedo at higher emission pointed to by the arrow. Plot (d) reveals that the lake surface albedo change is most noticeable as emission exceeds 60°, also shown with an arrow. This increase is indicative of a specular reflection of the sky as seen in Figure 3.5, but the effect is very subtle at 5 microns.

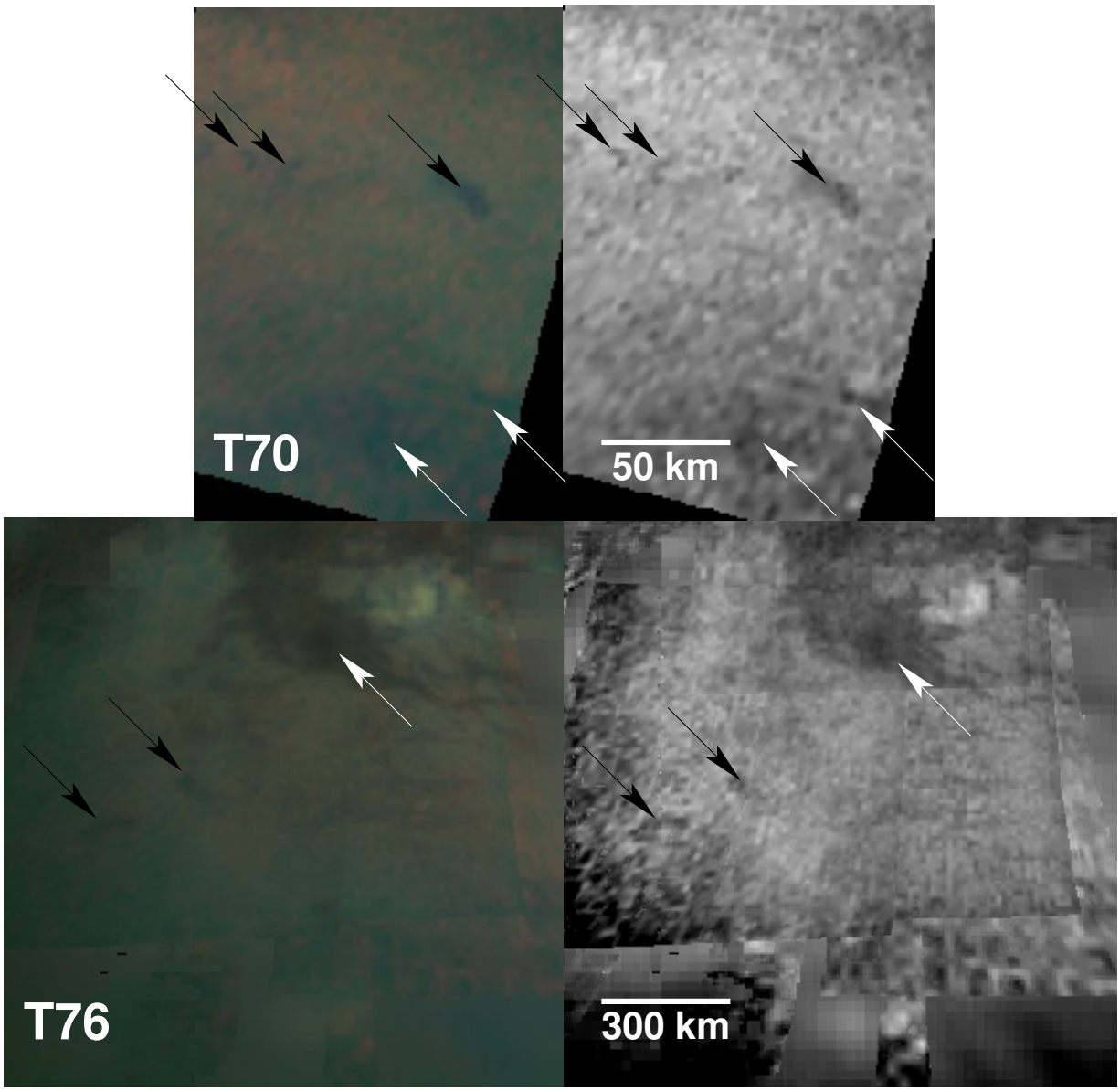

Figure 3.7: Two sets of images here from T70 and T76 show our 3-color mosaic outlined in Figure 3.1 on the left and the same area in the 5 micron window on the right. Surface features may exhibit lacustrine morphology but have an albedo that is too high, possibly due to coarse sampling resolution. The black arrows here point to surface features whose morphology is suggestive of a shoreline and small, enclosed lake but upon atmospheric correction yield a surface albedo similar to dunes and dark albedo lowlands. White arrows point to dark surface regions that have low albedo consistent with Kraken and Ligeia Mare but give no evidence of shoreline or other lacustrine morphologies. The albedo maps are not shown as the area coverage per pixel for the lake candidates is sufficiently small to not yield meaningful values.

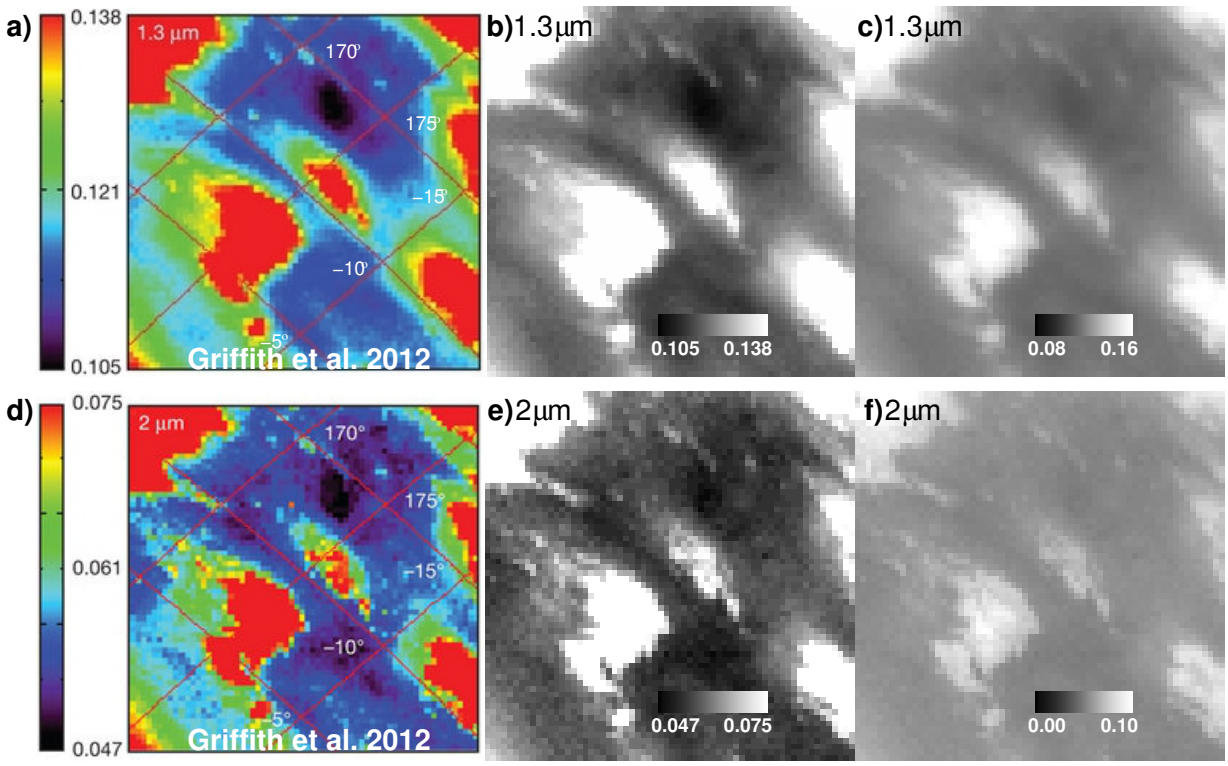

Figure 3.8: This figure shows the area of interest from Griffith et al. (2012b) in varying contrasts. The two strips above show VIMS cube CM_1567239055_1 from the T35 flyby at 1.3 (Top, a, b, c) and 2.0 (Bottom, d, e, f) microns. Parts (a) and (d) show modified versions of subfigures (a) and (d) from Griffith et al. (2012b), Figure 2. Parts (a)-(c) all display the 1.3 micron channel with part (c) having different contrast limits. Part (b) shows the area at the same contrast stretch as part (a) but without colorization. Many features are bled out in this stretch, so part (c) shows the area with a more moderate stretch. The "dark oval" feature from Griffith et al. (2012b) noticeably abates as the rest of the surface features within CM_1567239055_1 become more defined. For further comparison, parts (d)-(f) show the 2.01 micron channel with part (f) differing in contrast. Part (e) again shows the same stretch as part (d) but without colorization. Part (f) has a more moderate stretch and shows the abatement of the "dark oval" to a slightly darker, featureless area.

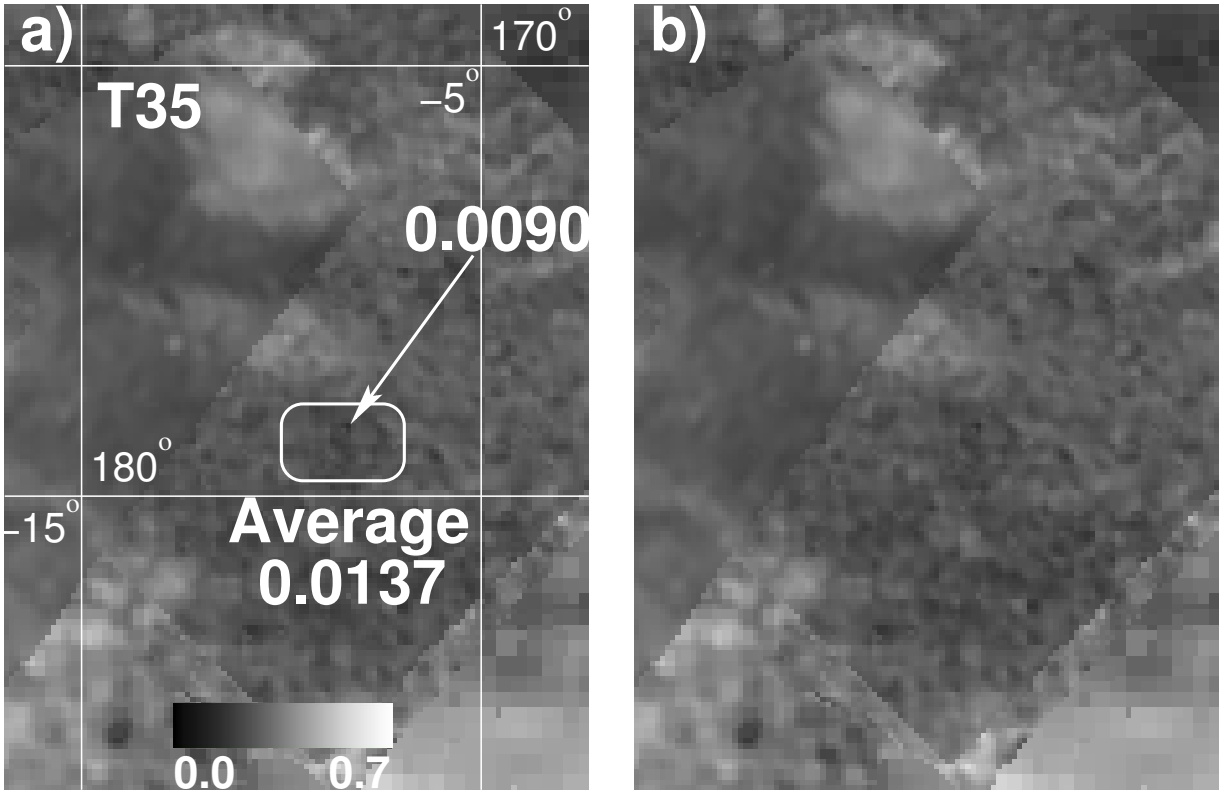

Figure 3.9: The figures above show the area around 14°S 173°W, designated in Griffith et al. (2012b) as "the dark oval," at 5 microns as processed by our model. (a) shows an annotated version of (b), each covering the same area. The single darkest pixel in the enclosed region has an albedo of 0.0090 and is consistent with lacustrine albedo. However, the average albedo of the area is 0.0137 (from a range of 0.0107 to 0.0167), which is a closer match to dune albedo. There is no well-defined lacustrine morphology when viewed in this area at 5 microns.

Chapter 4

Northern Temperate Lake Candidates on Titan

Graham Vixie[1], Jason W. Barnes[1], Shannon MacKenzie[1],
Sébastien Rodriguez[2], Christophe Sotin[3]

1. University of Idaho, Department of Physics,
P.O. Box 440903, Moscow, ID 83844-0903
2. Laboratoire AIM, Université Paris Diderot - Paris 7/CNRS/CEA-Saclay,
DSM/IRFU/SAp, Gif sur Yvette, France
3. California Institute of Technology/Jet Propulsion Laboratory,
4800 Oak Grove Drive, Pasadena CA, 91109

Presented in 2014, at the Lunar and Planetary Science Conference,
Volume 45, Abstract #2572

Email address: gvixie@vandals.uidaho.edu

Abstract

Titan's northern temperate latitudes have several small lake candidates. These lakes could have implications for climate and provide topographic constraints on Titan. The colloquially named "blandlands" of Titan may only be bland because of the spatial sampling at which they were previously viewed, as we identify several lake candidates of various lacustrine morphologies in VIMS (Visual and Infrared Mapping Spectrometer) with some RADAR coverage in this area. We find three regions that have candidates we conclude are probably lakes; three regions with possible, but inconclusive results; and one region not

showing convincing lacustrine features. The presence of lakes in both temperate zones on Titan is consistent with a global liquid transport and imply potential global populations of smaller, unresolved liquid bodies.

Keywords: Titan, Lakes, Cassini VIMS

4.1 Introduction

The largest moon of Saturn is home to many bodies of standing surface liquids (Hayes et al., 2011; Griffith et al., 2012b) and an active liquid exchange cycle between the atmosphere and ground (Tyler et al., 1981; Atreya et al., 2006; Sotin et al., 2012). These lakes and precipitation systems interact with Titan's global circulation at their relative latitudes.

Initial observations of clouds on Titan found them only near the south pole, predominantly south of 70°S latitude (Griffith et al., 1998; Roe et al., 2002). Roe et al. (2005a) then reported clouds around the 40°S latitude band, introducing the possibility of seasonal changes driving the global circulation of clouds. Global Circulation Models (GCMs) then predicted regular polar clouds along with sporadic 40° clouds in the summer hemisphere (Rannou et al., 2006). As Titan shifted to northern summer, the lack of clouds around 40°N combined with equatorial cloud events with rain, as evidenced by temporary albedo changes (Turtle et al., 2011b,c; Barnes et al., 2013a), provide constraints for GCMs (Rodriguez et al., 2009, 2011).

Although the majority of the lakes on Titan are located at and around its north pole (Aharonson et al., 2009), lakes have been identified in the southern polar (Brown et al., 2008), equatorial (Griffith et al., 2012b), and temperate (Vixie et al., 2014) latitudes. The presence of lakes globally presents interesting questions as to formation and filling mechanisms. The temperate latitudes show low contrast compared to equatorial and polar regions, appearing somewhat bland. The equatorial region is dominated by deserts filled

with longitudinal dunes and hills (Lorenz et al., 2006; Radebaugh et al., 2008; Rodriguez et al., 2014).

To date, no north polar lakes on Titan have shown temporal variability. Observed changes in location, shoreline retreat, or complete evacuation of lakes would imply some mechanism of liquid removal, the most likely being evaporation and infiltration, which also infers subsurface transport in a porous regolith (Hayes et al., 2008). Many south polar lakes, however, showed variation in RADAR (Synthetic Aperture Radar) (Hayes et al., 2011) as well as ISS (Imaging Science Subsystem) (Turtle et al., 2009, 2011c) with the presence of cloud systems nearby. Ephemeral lakes on Titan could therefore be temporarily filled by rainfall followed by evacuation. Many filled or partially filled north polar lakes sometimes exhibit 5 μm bright material, observed by VIMS (Brown et al., 2004), around the fringe and in the basins of dry lakebeds, interpreted to be evaporitic deposits (Barnes et al., 2011b). A global survey of this 5 μm spectral unit grants plausibility to paleolake basins near the equator (MacKenzie et al., 2014).

The presence of lakes and dry lakebeds at most latitudes would be supportive of liquid migration, either by evaporation and precipitation or infiltration and percolation, a local presence of rain or percolation for steady state lakes, or major long term climate changes. Aharonson et al. (2009) suggests the migration of liquids over Milankovich timescales from the south to the north. Hayes et al. (2008) and Cornet et al. (2012a) suggest percolation as a lake filling mechanism with the possibility of an underground reservoir.

This work presents a comprehensive survey of the northern temperate latitudes of Titan in search of plausible lacustrine candidates using VIMS data. First we present our lake candidates and discuss their locations and morphologies. Next, we use a single-scattering approximation radiative transfer model to look at surface albedos in and around the features of interest and compare those to the previously identified north polar lakes. We conclude with a discussion of our results' implications for Titan's climate and liquid bodies.

4.2 Lake Candidates

Our 16 candidates, found between 41°N and 72°N, exhibit plausible lacustrine morphology, including distinct, lobate or semi-lobate boundaries in addition to low relative surface brightness; low absolute (where applicable) or relative surface albedos; and being distinguishable in the majority of wavelengths where Titan's methane-dominant atmosphere does not absorb and the surface is distinguishable. Many of the candidates are spatially very small or narrow as viewed by VIMS, so morphological arguments are not strong enough on their own. We present evidence to suggest that these regions of interest could be lacustrine in nature. All lake candidates are also very small in the resolution and pixel count (in at least one dimension) leading to a mixing of surficial substrates within a single pixel causing the albedo to be higher than expected in many cases. We discuss this pixel smearing further in the next section.

4.2.1 North Dilmun

The first candidates are from T69, *Cassini*'s 69th close flyby of Titan (June 5, 2010), and can be found in the North Dilmun region located in the northern mid-latitudes above the Huygens landing site. Figure 4.1 shows each candidate annotated by a black arrow in composite images at six infrared wavelengths where the surface is distinguishable. Ligeia Mare, one of Titan's largest seas, is visible in the northwest region of each image and offers a relative comparison for brightness for each of our candidates.

Feature A is a small, triangular two body system possibly connected by a small channel around 50°N, 179°W. This feature is very distinct, especially at 2 and 5 microns, and has a low $\frac{I}{F}$ relative to its surroundings. There are two clouds visible at all wavelengths just north of A as well, possibly a sign of persistent lake infilling via precipitation.

Feature B is an elongated, latitudinally thin dark feature at 72°N, 179°W, which intrudes into the polar region, but was included by proximity. C and D are clusters of small,

disjointed dark features. T69 offers the best resolution for these features.

4.2.2 Virgae

The next candidates are a proximal set of dark virgae as viewed by VIMS found around 44°N, 115°W north of Adiri and the Huygens landing site. The International Astronomical Union defines a virga to be a streak or stripe of color. These virgae are 200 - 600 km in length, spaced 200 - 400 km apart, and are relatively dark to their immediate surroundings. Figure 4.2 shows a composite image from the T79 flyby at various wavelengths where the surface is visible through Titan's nitrogen-methane dominated atmosphere. These features also appear in VIMS in T26, T28, T31, and T69 (candidate D in Figure 4.1). The locations of each lake candidate are: 41.3°N, 111.5°W; 50°N, 107.1°W; 45.7°N, 124.3°W; 49.8°N, 126.6°W; and 50.5°N, 134.2°W. Best discernible in the 2 micron window, the morphology of these virgae could suggest channels if they are depressions, except that they are too large to be fluvial features. The T30 Synthetic Aperture RADAR (SAR) flyby crosses over a portion of the central area of interest showing bright, distinct boundaries around an average to darker center for two of the VIMS dark virgae covered by the swath. Without any topographical information, we cannot say if this implies an embankment. However, these candidates not appearing RADAR dark implies these features are most likely not lakes unless they are either very shallow or mudflats.

4.2.3 Other Candidates

The remaining candidates are found in various locations and are shown in Figure 4.3. This figure again shows the regions of interest, each their own column, to show the persistence of the candidates in the windows. All features pointed out in this figure also display some level of lobate boundary around an interior of low $\frac{I}{F}$.

The first feature, located at 44.0°N, 10.3°E, from T52 shows up most distinctly in the 5 micron window. The proximity of "Remora" to Kraken Mare (seen to the NE of the

image) offers a beneficial comparison for brightness as the feature appears darker than the closest portion of Kraken. Kraken Mare's decreasing brightness at northern latitudes is both an effect of increasing emission angle and the terminator.

The central column of Figure 4.3 shows the second feature, located at 46°N, 66°W, from the T23 flyby. The proximity of "Noctua" to the dune fields and Minerva crater, which appear to the southwest of the feature, may indicate a dry or shallow feature rather than a currently filled lake or simply an extension of the dunes. The encroaching terminator here may artificially lower the albedo results we derive later on. Both VIMS and ISS lack quality resolution coverage in the leading hemisphere.

The third pair of features, from the T90 flyby, intrude somewhat into the polar region, but are not enclosed in the preponderance of north polar lakes. The "Pair," located at 75.6°N, 116.6°W and 72.6°N, 106°W, are the least spatially resolved of our set, yet still show low $\frac{I}{F}$ and exhibit a semi-lobate boundary. Although no homogeneous pixel exists within the candidates, we have a follow up flyby in T97 showing the "Pair" to be lakes by comparison to the multitude of liquid bodies in the same image.

Lastly, we identify two more candidates from T97, located at 52°N, 131°W and 42.6°N, 130°W. The northern of the two shows low $\frac{I}{F}$ and lobate morphology with a claw-like shape. The southern candidate has a wishbone-like morphology and bears similarity to the virgae seen in our T79 image. Both candidates (hereinafter referred to as the "Claw" and the "Wishbone") have low $\frac{I}{F}$ with the Claw being slightly darker than the Wishbone as shown in Figure 4.4.

4.2.4 Comparison to Known Lakes

We analyze our 16 candidates by comparison to smaller lakes with heterogeneous, model-derived surface albedos as well as larger known liquid bodies. Our first control lake, Hammar Lacus from T76, exists just south of Kraken Mare at 48.7°N, 48.4°E (Figure 4.5). Hammar Lacus shares similar characteristics to our lake candidates and spans one pixel

latitudinally; we show this control at several of Titan's methane windows. Müggel Lacus from T93, located at 83.9°N, 161°E, presents as another good control found near the north pole (MacKenzie et al., 2014). Figure 4.5 shows this lake, best viewed at 2 and 5 microns, has many areas either representative of islands or mudflats (as VIMS only penetrates a few microns into the surface). In addition, we consider Ligeia Mare as it appears in our T69 image, Kraken Mare from T52 and T76, Kivu Lacus and Punga Mare from T93, and the two lakes from our T90 image. The next section describes our correction and methods used for each of these control lakes.

4.3 Window Corrections

For the current study we use the same method as in Vixie et al. (2014) applied to more wavelength windows. Our radiative transfer model uses the single-scattering assumption to consider photons approaching Titan and either 1) pass through the atmosphere unhindered and reflect off the Lambertian surface before collection by *Cassini*, 2) scatter once in the atmosphere without ever interacting with the surface, or 3) scatter in atmosphere then reflect off of the surface. All atmospheric based calculations use an orange-rind model from Barnes et al. (2009a).

We now consider the 2 and 5 micron wavelength windows for correction and empirically solve for the surface albedo for each candidate. We mask regions that we assume to have the same albedo and organize them into 2° incidence angle by 2° emission angle bins, then separate the bins by regions we label as bright, similar to the equatorial bright region (Barnes et al., 2007; Langhans et al., 2012); lake, which comprises all dark regions of previously identified lakes and seas (Stofan et al., 2007; Paillou et al., 2008; Barnes et al., 2009a; Wall et al., 2010; Stephan et al., 2010; Cornet et al., 2012a); and dune, representing the equatorial dark brown dune fields (Lorenz et al., 2006; Barnes et al., 2007; Soderblom et al., 2007; Rodriguez et al., 2014). The opacity, τ, has a fixed value between our best fit

and the appropriate value from Barnes et al. (2013b) for each wavelength. The atmospheric single-scattering albedo, $\tilde{\omega}$, has a fixed, best-fit value. At each of these wavelengths, the $\frac{I}{F}$ is a function of at least incidence, emission, and phase (despite only be plotted in three dimensions) and does not well quantify the best fit.

We observe a smaller than anticipated effect when varying phase angle, shown in Figure 4.6. The phase angle changes very little over a single flyby. The phase angle does not change the surface phase function in our Lambertian assumption, but does affect the atmospheric phase function. However, a 5 micron wavelength decreases the atmospheric contribution, leading to a smaller contribution from phase change. The left hand column shows our empirical model fit at 5 microns for each of our three regions with all phases allowed. Each plot has the raw $\frac{I}{F}$ versus incidence and emission as a scatterplot with our model as the fitted surface. The column on the right shows the same data but restricts the phase between 23° and 43° before making the fit. The resulting differences between the plots in the left and right columns for each region are either very subtle or insignificant.

Our best-fit χ^2 value grows several orders of magnitude when restricting the phase without any real noticeable difference in the fit surface. We conclude that either our data set is too limited, or that the phase difference is not as consequential to our model as previously thought (Vixie et al., 2014). A better comparison could be made with $\geq$ 100 data points having the same phase angle within a given region. With present data, restricting the phase to a single value or bin leaves an insufficient number of points ($\leq$3).

The 5 micron correction case has very little contribution from atmospheric effects (Baines et al., 2005; Barnes et al., 2005), allowing for surface albedo derivation and comparison. At 2 microns, however, the atmospheric influence for *Cassini* increases. Thus atmospheric scattering will apply to a larger fraction of $\frac{I}{F}$ in the 2 micron VIMS images, resulting in higher $\frac{I}{F}$ in the corrected images compared to the originals. The corrections for each region at each wavelength can be found in Table 4.2 along with the values of τ and $\tilde{\omega}$ used for each wavelength. The middle section shows the model-derived surface albedo

for each candidate; the bottom section shows the albedos for the control lakes. Looking at the albedos for the control lakes shows variation by flyby of the same feature. Kraken Mare, for example, has several different possible values, either due to changing viewing geometry, a limitation within the model, a terminator effect, or some combination of the three. The 2 micron corrections are particularly inconsistent in control lake albedo, likely due to shortcomings of the single-scattering approximation.

4.3.1 Candidate Analysis

Next, we compare the model-derived surface albedos in Table 4.2 between each candidate and the control lakes. We then evaluate each candidate for lake plausibility.

Starting with T23, both the 2 and 5 micron surface albedos are higher than expected, but agree with the higher end estimates of the control lake surface albedos. The 2 micron correction shows a potential darking of "Noctua" by the nearby terminator, seen in the central column of Figure 4.3, judging from the very dark areas surrounding Minerva crater. Also in the 2 micron correction is a dark area immediately west of "Noctua" plausibly representing an extension of the same substrate material around Minerva, though we do not expect dunes at 46°N (Radebaugh et al., 2008). However, Radebaugh et al. (2012) gives evidence for lakes and dunes to co-exist based on Huygens measured methane humidity and emboldened by equatorial rainfall. We label this candidate as plausible, but ambiguous.

"Remora" also exhibits a higher than expected surface albedo. Fortuitously, Kraken Mare appears in the same image (also Figure 4.3) and has similar surface albedo values to "Remora." The southern portion of Kraken appears possibly covered by a faint cloud or otherwise have an artificially raised surface albedo due to the atmosphere, which is more easily seen in the 5 micron image where the high albedo region intrudes somewhat into the southern part of Kraken, making the values for the northern part of Kraken more realistic. Since the model-derived surface albedos match for "Remora" and the northern part of Kraken at both 2 and 5 microns, we think that this candidate is likely a lake and

would benefit from a follow-up observation.

Candidates A and B in the T69 image (Figure 4.1) have albedos in the range of similar characteristic control lakes, around 0.028 at 5 microns, while C presents a much higher 0.042. Ligeia Mare in the northwest of this region may have an artificially lowered albedo due to its proximity to the terminator, similar to the T23 analysis. Considering both the 2 and 5 micron values, we think A and B are likely lakes while C is likely not. We'll leave the analysis of D with the T79 virgae discussion due to higher spatial resolution of this same area in that flyby (Figure 4.2).

Both corrections yield low albedos for the T79 virgae, but because of the RADAR cross-over showing no dark/smooth area in the center of the features, we do not think that these candidates are lakes. If any liquid exists in these features, either the depth is very shallow or the ground is wet, akin to a mudflat or a bog. Both of these scenarios would show a low $\frac{I}{F}$ signal for VIMS, as penetration only occurs in the top several microns of the surface, but normal to RADAR. Once again, we think these virgae are probably not lakes.

The "Claw" in T97 (Figure 4.4) yields a low model-derived surface albedo at both 2 and 5 microns while the "Wishbone" is only low at 2 microns. The "Wishbone" bears a resemblance to the T79 Virgae both in $\frac{I}{F}$ and morphology; however, the slightly higher albedo leads us to think the "Wishbone" is probably not liquid filled for their similarity to the T79 case. The "Claw" appears darker in the 2 micron corrections than all of our control lakes, which again could represent favorable viewing geometry or model-generated over-correction or limitation. However, the 5 micron model-derived albedo falls between the bifurcation of the control lake values, thus we think the "Claw" is plausibly liquid-filled or wetted.

Many candidate observations only exist on the subpixel scale or consist of very few pixels. This results in a spectral mixing of multiple substrate types within a given pixel (Combe et al., 2007). Though the reported value of a pixel may be much higher than what

we consider to be lake-like with our model, if the value is lower than the surrounding, similar terrain we can plausibly say a dark portion of a given pixel may be driving the value down across a feature of interest. While this is by no means conclusive for surface albedo, we maintain a feature's candidacy until the possibility of a higher spatial sampling encounter later in the *Cassini* mission.

4.4 Discussion

Figure 4.8 shows a global map of Titan showing the locations of each of our 16 candidates. We ranked each of our candidates by colored circles based on their model-derived albedos and comparison with our control lakes. From this compilation, we do not see any longitudinal dependence on where candidates or lakes are in the mid-latitudes. The leading hemisphere exists at lower resolution in VIMS data making the temperate latitudes somewhat devoid of candidates. This scenario is expanded to all temperate latitudes at a lesser extent due to low contrast when compared to the equator and pole regions (with a few exceptions). That is to say, more candidates may exist below current VIMS resolution data though we have noted all candidates above $\sim$140 km in diameter, based on our largest positive candidate.

The north-south liquid asymmetry on Titan is an ongoing topic of research. Aharonson et al. (2009) suggests that liquid migrates from the south pole to the north over Milankovich timescales. Hayes et al. (2008) and Cornet et al. (2012a) outline the possible existence of an underground reservoir that could percolate up in basins and other low topographic regions.

This study finds further evidence for lake at many latitudes rather than exclusively the polar regions (Hayes et al., 2008), though northern temperate lakes are not farfetched given Kraken Mare's southern portion extending south of 60°N. Dry, intermittent, and filled lakes across latitudes support a filling mechanism such as local precipitation or percolation via

subsurface reservoirs in low topography areas.

Large scale migration would entail the majority of the liquid moving between the south and north poles, but probably not all at once. Lakebeds at various temperate latitudes imply that liquid may stop over along the way, either by precipitation and subsequent evaporation or by infiltration and percolation. The existence of lakes at multiple latitudes does not necessarily imply liquid migration, but is consistent with such a hypothesis.

If these temperate lakes are the result of local precipitation or percolation, then migration could still be taking place. However, the local topographic implications are independent of such long-term movement. Previously, we have seen liquid darkening a surface and evaporating shortly thereafter without requiring a topographic low (Turtle et al., 2011b; Barnes et al., 2013a; Lorenz et al., 2013). However, if a liquid feature proves to be consistent over multiple flybys, we can constrain, even if very locally, the topography of that area. Lorenz et al. (2013) places all of our northern candidates at an average topography, similar to that of Kraken Mare's southern extension.

Increased shoreline recession in one hemisphere would be supportive of migration away from the more evaporitive hemisphere. Sotin et al. (2012) demonstrated that while we might expect shoreline recession in the north since the rains (and clouds) have disappeared there, two images of Ligeia Mare taken 3 years apart show none. Ontario Lacus, however, shows only minor shoreline recession (Hayes et al., 2011; Turtle et al., 2011c) or is possibly a remnant lake having previously undergone extensive evaporation (Cornet et al., 2012a; Luspay-Kuti et al., 2014). However, the wet northern summer and dry southern winter have just ended, providing an opportunity for *Cassini* to look for cloud migration and monitor the south pole for infilling.

4.5 Conclusion

We present three candidates as probable lake regions that would benefit from future observations, three regions that warrant further study, and one region that appears dark to VIMS and ISS, but not to RADAR. A more sophisticated radiative transfer model could also better classify the ambiguous result candidates. Following the trend of numerous north pole lakes compared to the south, we find more plausible lake candidates in the northern hemisphere than the southern.

The "bland" northern temperate latitudes on Titan may host several lakes or evidence of past lakes. A lacustrine presence in the southern mid-latitudes (Vixie et al., 2014) and, as shown in this work, across to the northern temperate regions may be indicative of a large scale liquid migration across Titan or, more simply, be evidence of precipitation and/or percolation in each area with localized basins or low topography. The locations of the lake candidates suggest no longitudinal dependence, however. The low spatial sampling along much of the temperate latitudes inhibits a more in-depth study of the regions of interest there, but the current data gives enough to identify interesting targets for future flybys.

Looking at the relative brightness of dark regions that only fill a single pixel compared to their surroundings provides a method of determining if a region of interest or feature is indeed dark, but does not provide enough context to say if the region or feature has a sufficiently low albedo to be liquid. However, the use of this method with previously identified filled or intermittent lakes allows the determination of lake candidacy to be made.

Cloud activity in the temperate latitudes may be indicative of ephemeral lakes or a resupply of existing lakes. Candidate temporal variability in future flybys would suggest evaporation or infiltration without replenishment, and conjectures a shallow lake or a wetted surface. Candidate longevity would point to precipitation or percolation, which infers a local elevation either of the basin or of a subsurface reservoir. Exploration of the blandlands may not reveal any large scale features, but may show a multitude of smaller

ones. Patterns in lake location, formation, and dissipation would also shed more light on Titan's lake asymmetry.

4.6 Acknowledgments

The work done here was made possible by NASA and the VIMS team. The authors also acknowledge funding from the NASA Outer Planets Research program and an Idaho EPSCoR Graduate Research Fellowship.

	Flyby	Date	Integration Time (ms)	Resolution (km/pix)	Incidence Angle (°)	Emission Angle (°)	Phase Angle (°)
Lake Candidates	T23 Candidate	Jan 13, 2007	320	71	73.8	39.7	109.7
	T52 Candidate	Apr 4, 2009	120	90	64.8	47.6	109.3
	T69 A	June 5, 2010	120	20	65.2	50.0	28.3
	T69 B	June 5, 2010	120	28.2	76.0	68.0	29.0
	T69 C	June 5, 2010	120	21.6	66.1	52.0	28.5
	T79 Virgae	Dec 13, 2011	280	30-41	44-55	53-56	20-21
	T97 The Claw	Jan 1, 2014	120	9.1	48.0	11.8	51.4
	T97 The Wishbone	Jan 1, 2014	120	8.9	46.0	22.8	52.0
Control Lakes	T52 South Kraken Mare	Apr 4, 2009	120	64-90	56-76	40-53	109
	T69 Ligeia Mare	June 5, 2010	120	67	74.2	77.3	30.6
	T76 Hammar Lacus	May 8, 2011	140	17.2	41.8	38.2	42.1
	T76 South Kraken Mare	May 8, 2011	140	18.3	52.8	66.1	41.9
	T93 Müggel Lacus	July 26, 2013	300	9.9	65.0	28.8	87.0
	T93 Kivu Lacus	July 26, 2013	300	6.0	69.3	19.4	85.2
	T93 Punga Mare	July 26, 2013	300	5.8	73.0	17.6	84.5
	T97 Pair	Jan 1, 2014	120	13.8	64.9	12.3	52.9

Table 4.1: Table of observations for used cubes.

	Flyby	2μm Corrected Surface Albedo	5μm Corrected Surface Albedo
Model	τ	0.185 ± 0.002	0.08 ± 0.01
Values	$\tilde{\omega}$	5.7 ± 0.1	1.0 (fixed)
Lake	T23 Candidate	0.09 - 0.11	0.025 - 0.033
Candidates	T52 Candidate	0.35 - 0.38	0.030 - 0.040
	T69 A	0.27 - 0.30	0.028 - 0.037
	T69 B	N/A	0.027 - 0.028
	T69 C	0.34 - 0.35	0.041 - 0.044
	T79 Virgae	0.19 - 0.21	0.026 - 0.037
	T97 Claw	0.16 - 0.17	0.023 - 0.030
	T97 Wishbone	0.18 - 0.19	0.035 - 0.040
Control	T52 South Kraken Mare	0.44 - 0.48	0.045 - 0.053
Lakes	T52 North Kraken Mare	0.34 - 0.38	0.030 - 0.039
	T69 Ligeia Mare	N/A	0.005 - 0.015
	T76 Hammar Lacus	0.20 - 0.21	0.042 - 0.047
	T76 South Kraken Mare	0.17 - 0.19	0.000 - 0.005
	T93 Müggel Lacus	0.20 - 0.22	0.012 - 0.016
	T93 Kivu Lacus	0.17 - 0.18	0.000 - 0.004
	T93 Punga Mare	0.15 - 0.17	0.000 - 0.006
	T97 Pair	0.20 - 0.23	0.026 - 0.029

Table 4.2: This table summarizes the model derived surface albedos for each candidate region.

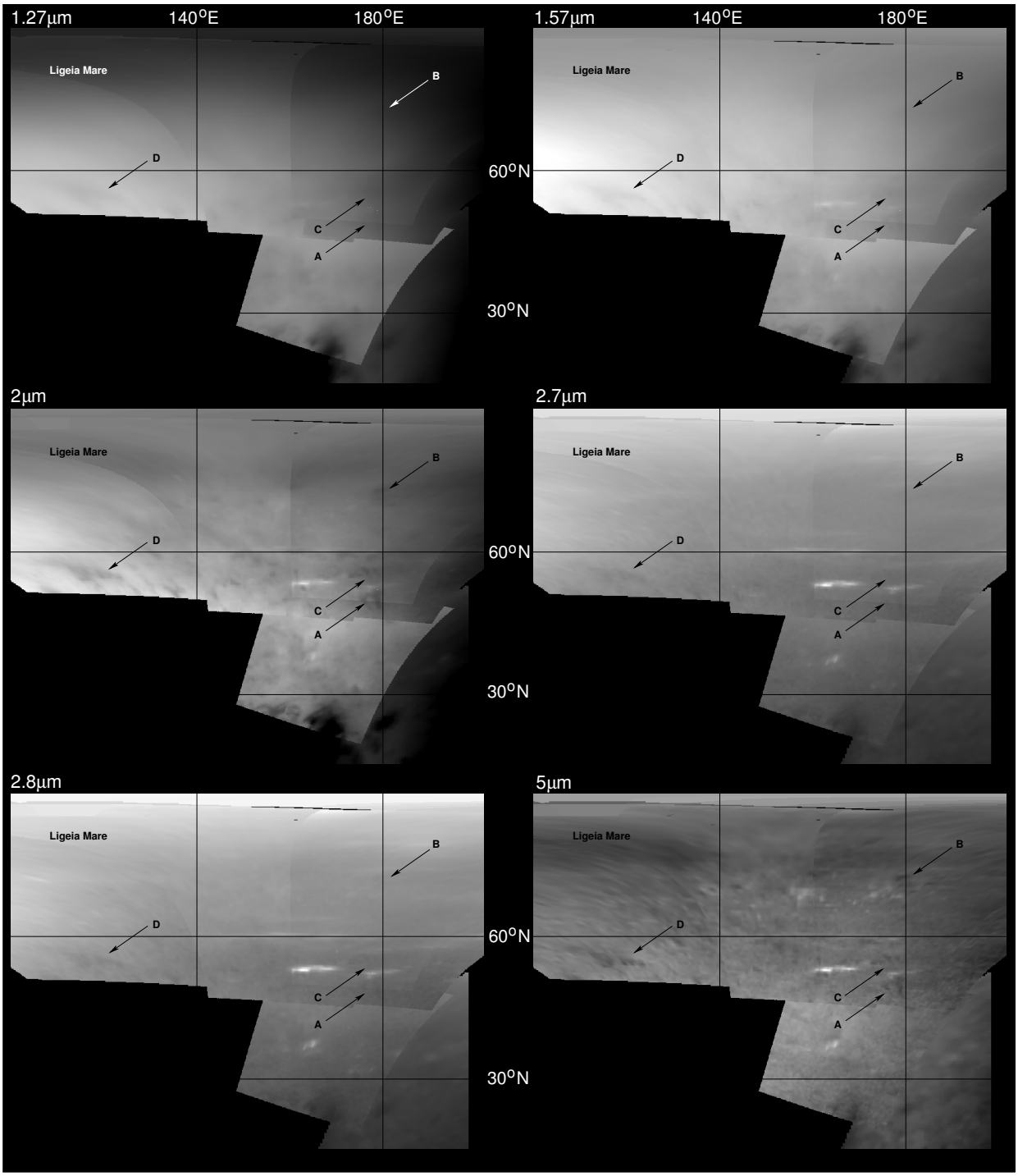

Figure 4.1: The images here show the North Dilmun area from T69 in the majority of Titan's methane IR windows. The dark regions labeled A-D here represent our lake candidates. Candidate A in the southernmost region bears possible lacustrine morphology. Candidates A-D appear dark relative to their respective surroundings and yield surface albedo values in the range of 0.016 and 0.018, for a 5 micron correction. The bright white features, like those just south of the 60° latitude line, are clouds alluding to the possibility of localized rainfall. Ligeia Mare, in the northwest corner of each image, provides an observational comparison for the expected darkness of lakes at each wavelength.

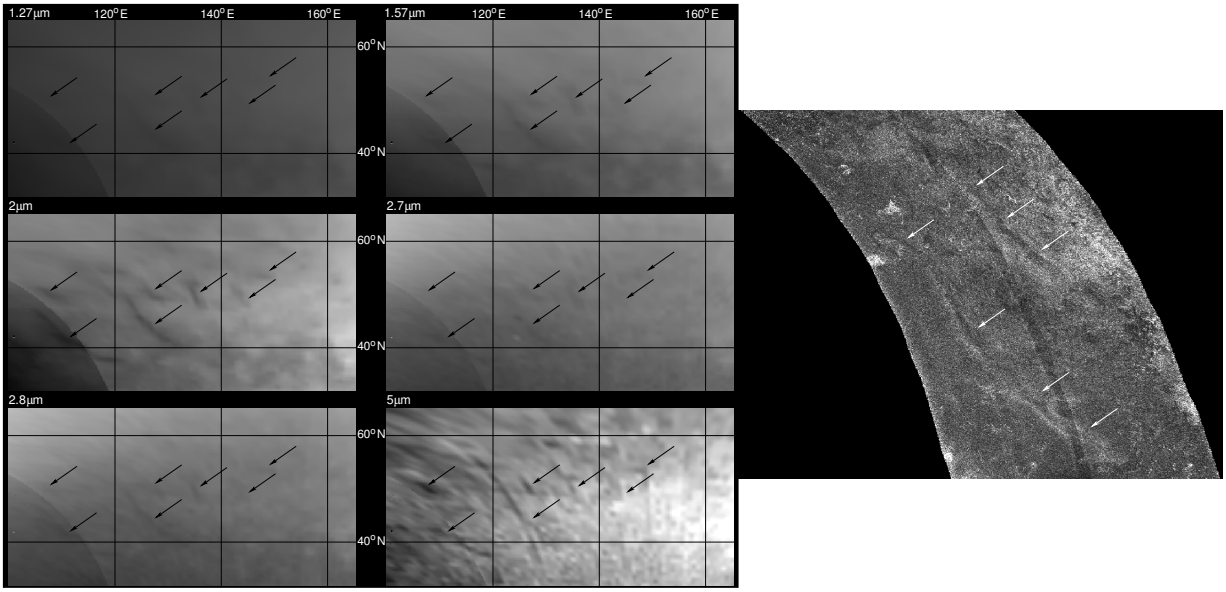

Figure 4.2: The six images here show a composite from T79 at several IR methane windows. The black arrows in each window point to virgae seen in VIMS north of the Huygens landing site. These features are considered lake candidates because of their consistent appearance in each IR window and relative darkness to their surroundings. The linear nature of these candidates alludes to significant albedo mixing or smearing within each single pixel. The RADAR image on the right, taken during T30, shows two of the virgae annotated with white arrows that correspond to the 3 central black arrows in the VIMS images. Here we see the center of these virgae is not RADAR dark, as would be expected in most cases of standing liquid.

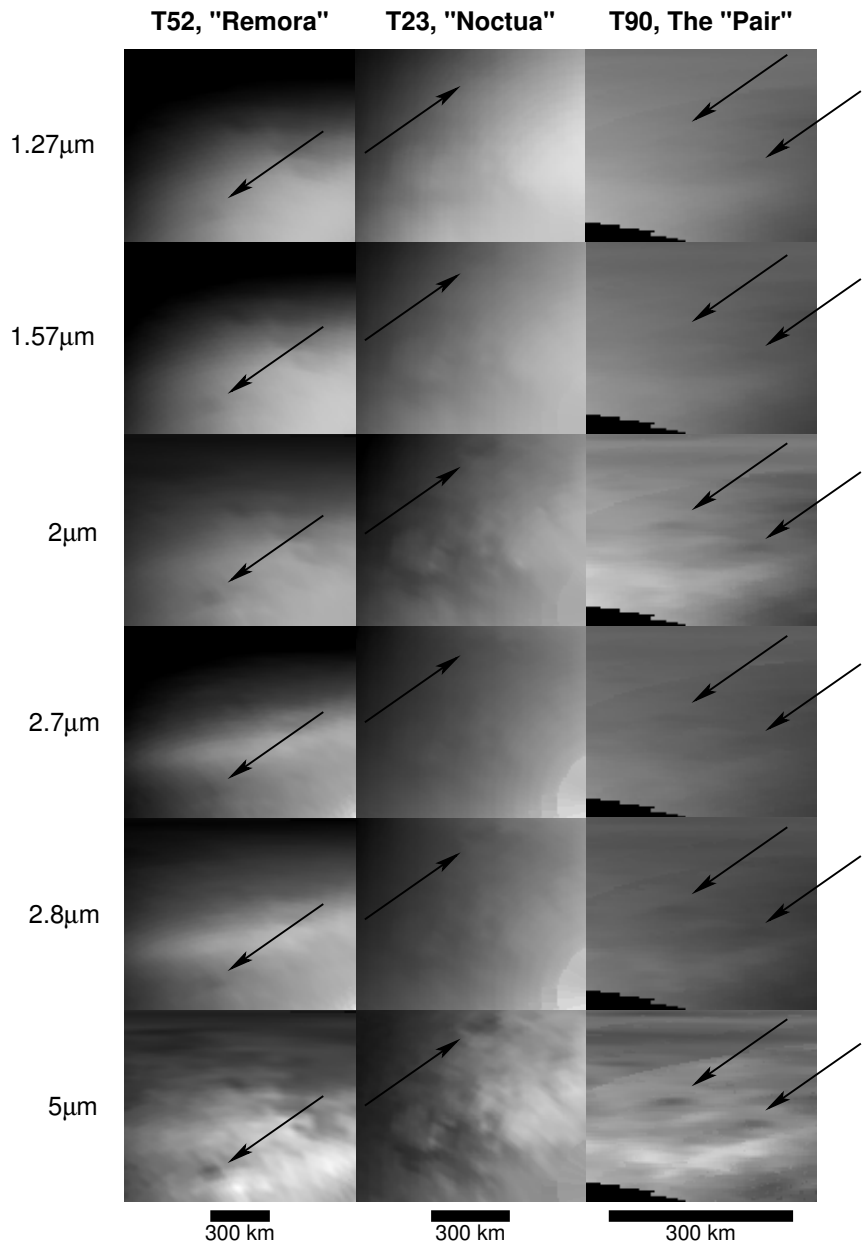

Figure 4.3: These images show candidates from T52, T23, and T90 at several of the IR methane windows. Each column shows the same image from each respective flyby at a different wavelength. The black arrows point to our candidates, named at the top of each column. In each flyby, the pointed-to feature(s) is dark relative to its surroundings and somewhat lacustrine, i.e. semi-lobate. "Remora" to the southwest of Kraken Mare allows for an observational comparison between the two. "Noctua" lies just northeast of Minerva and the surrounding dune fields. The "Pair" are on the fringe of the north polar area.

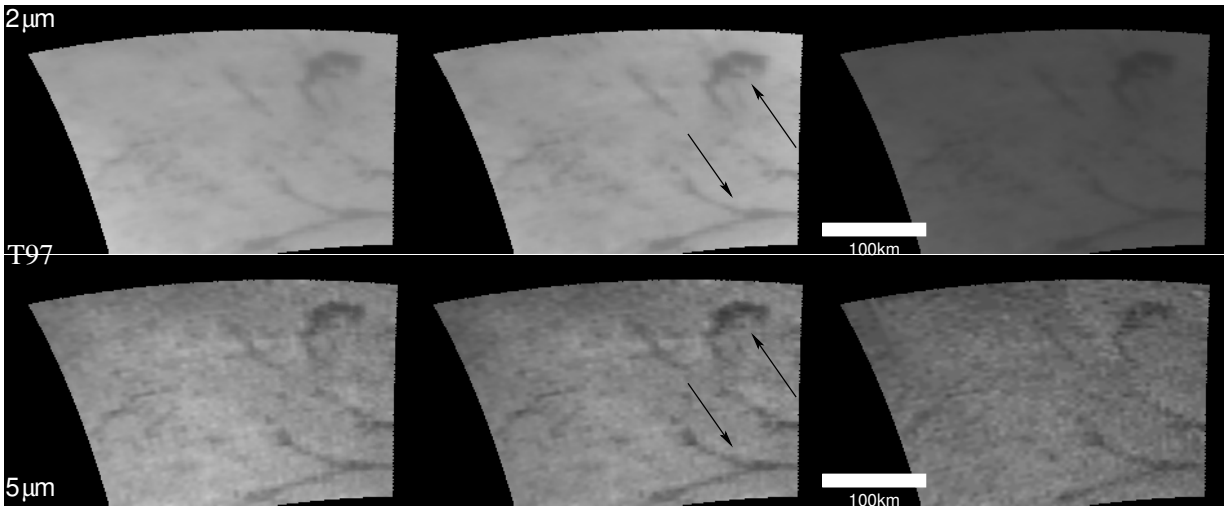

Figure 4.4: These images from T97 reveal two features of interest to our lake study. The top row shows the region in the 2 micron window while the bottom row has the same region in the 5 micron window. The first column shows an unannotated and uncorrected look at a claw-shaped dark feature in the upper right and a wishbone-shaped virgae similar to those in Figure 4.2. The same images, corrected by our model to remove some atmospheric effects and annotated with arrows indicating our lake candidates, make up the central column. These candidates are located at 52°N, 131°W (the Claw) and 42.6°N, 130°W (the Wishbone) with model-derived surface albedos at 5 microns of 0.025 and 0.037, respectively. At 2 microns, the derived surface albedos are 0.165 and 0.184. In the last column, the original VIMS images are stretched to the same degree as that of our corrected images (center column), highlighting the utility of our model in discerning these fainter surface features.

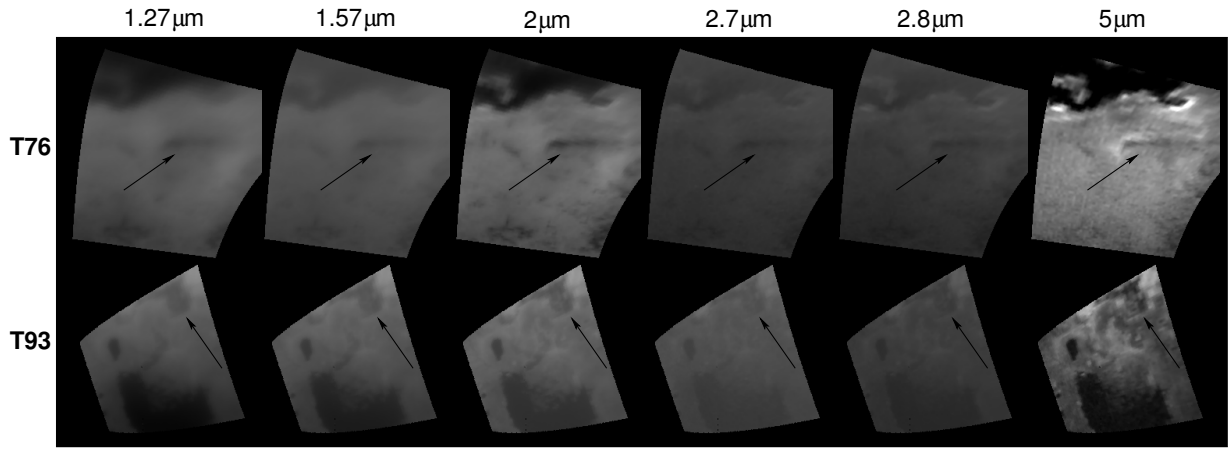

Figure 4.5: This figure shows the previously identified polar lakes indicated by black arrows that we use as controls: Hammar Lacus (top row, T76) and Müggel Lacus (bottom row, T93). The larger dark feature in the T76 image is Kraken Mare with evaporitic bright fringes visible at 5 microns. Hammar Lacus has a higher reported surface albedo than the dark seas, but still lower relative to its average surroundings. The T93 image shows Punga Mare (larger) and Kivu Lacus (smaller) near Müggel Lacus which is thought to be to either be mud flats or intermittently filled (MacKenzie et al., 2014).

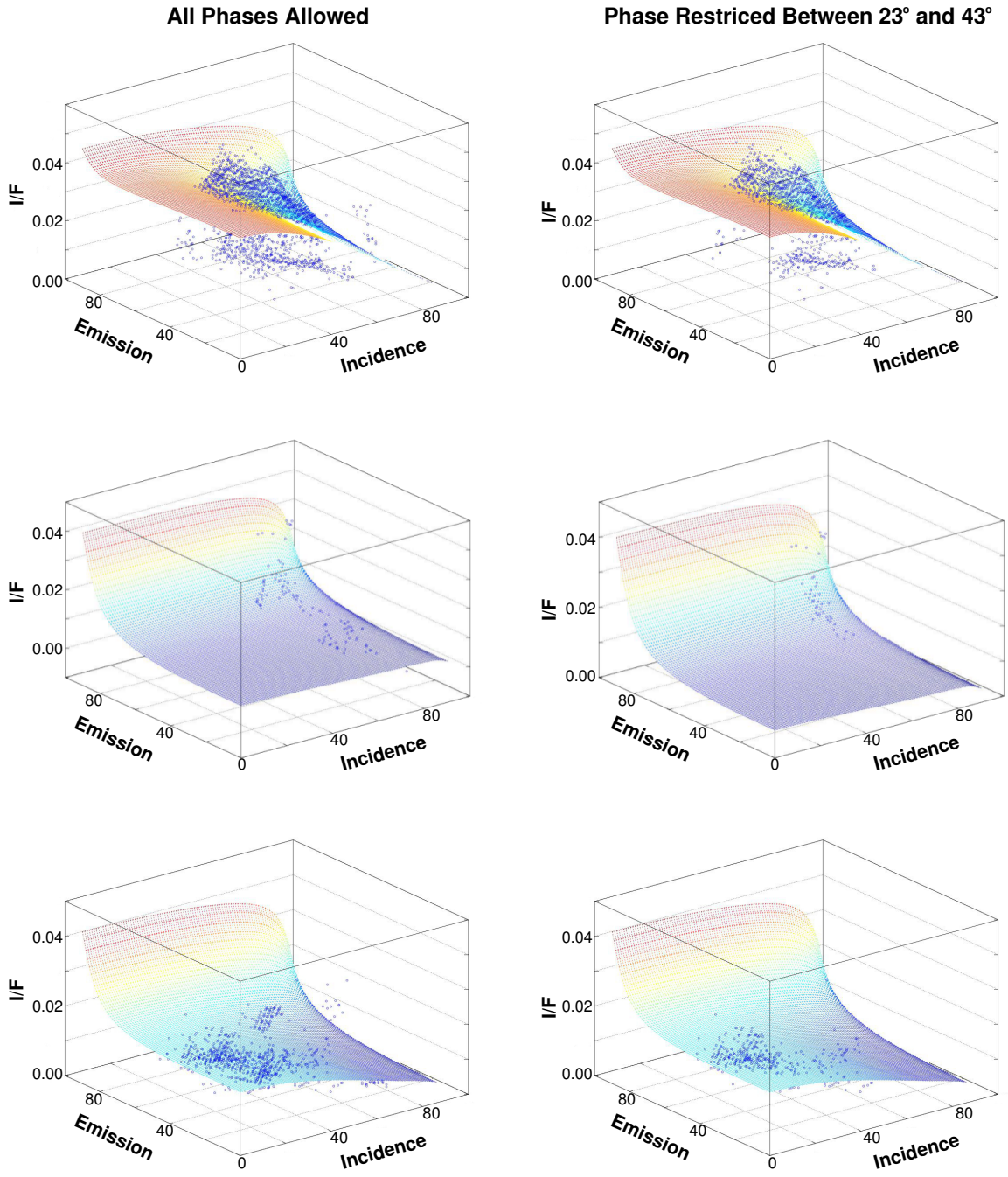

Figure 4.6: Each plot shows the model best fit surface drawn with the raw $\frac{I}{F}$ scatterplot versus incidence and emission. Each row represents a different region masked by the model: the top is equatorial bright, the middle is lake, and the bottom is dune. In the left column, the phase for each point in the surface is calculated to be the real value based on the other viewing angles and all phase values are allowed in the raw $\frac{I}{F}$. On the right, we only allow phase values between 23° and 43° to examine how phase may affect the each plot. The differences here between the columns are very minuscule, implying differences in phase have only minor effects.

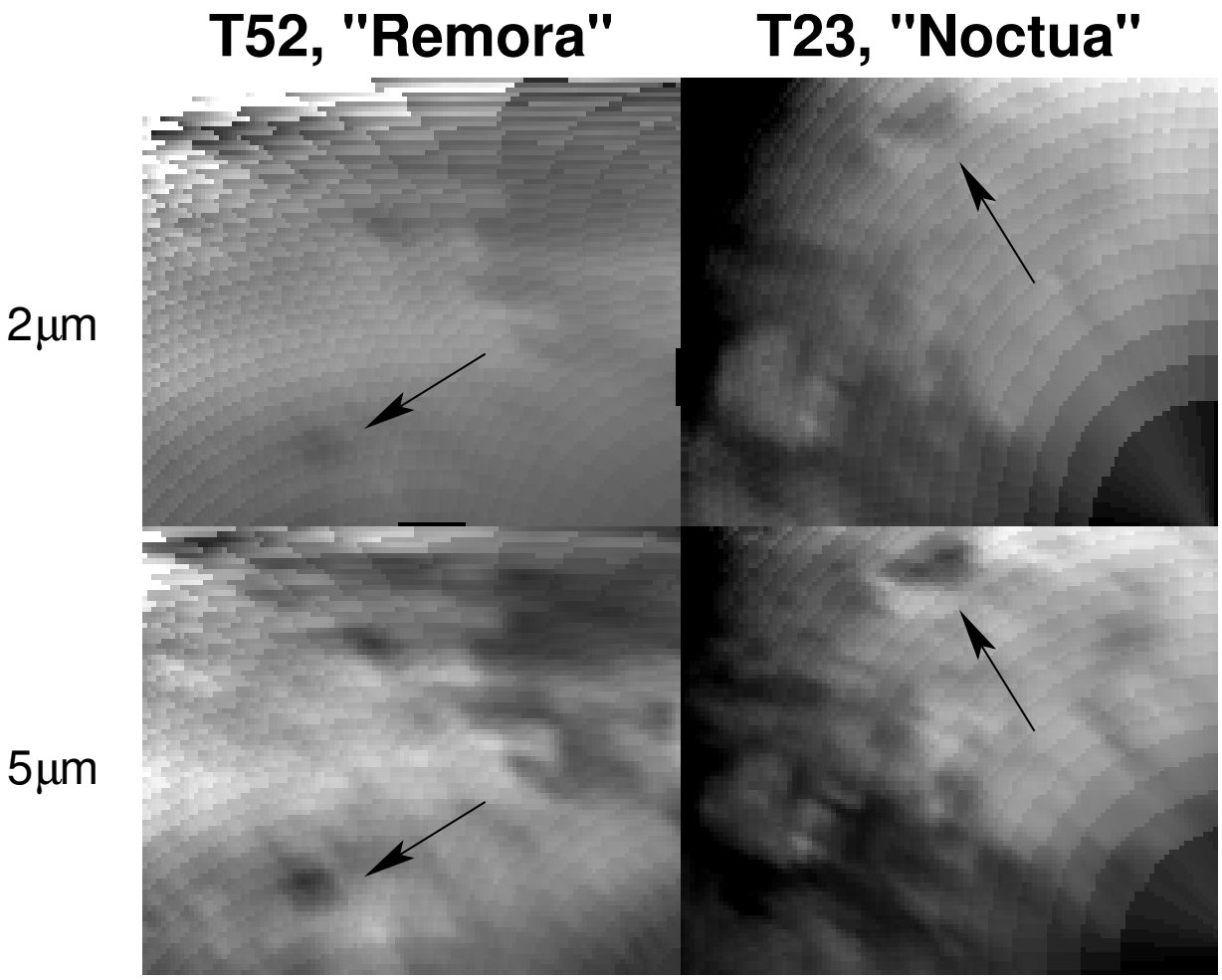

Figure 4.7: Here we show the 2 and 5 micron corrections to the T23 and T52 images, indicated by black arrows. "Remora" matches the northern part of Kraken Mare at 2 microns and 5 microns. In the 5 micron correction, the effect of increasing emission angle darkens Kraken moving north to the limb. In the 2 micron correction for T23, a dark feature to the west of "Noctua" appears more apparent than in the uncorrected image in Figure 4.3. This could possibly be an extension of the terrain surrounding Minerva crater to the south or an effect of the imminent terminator.

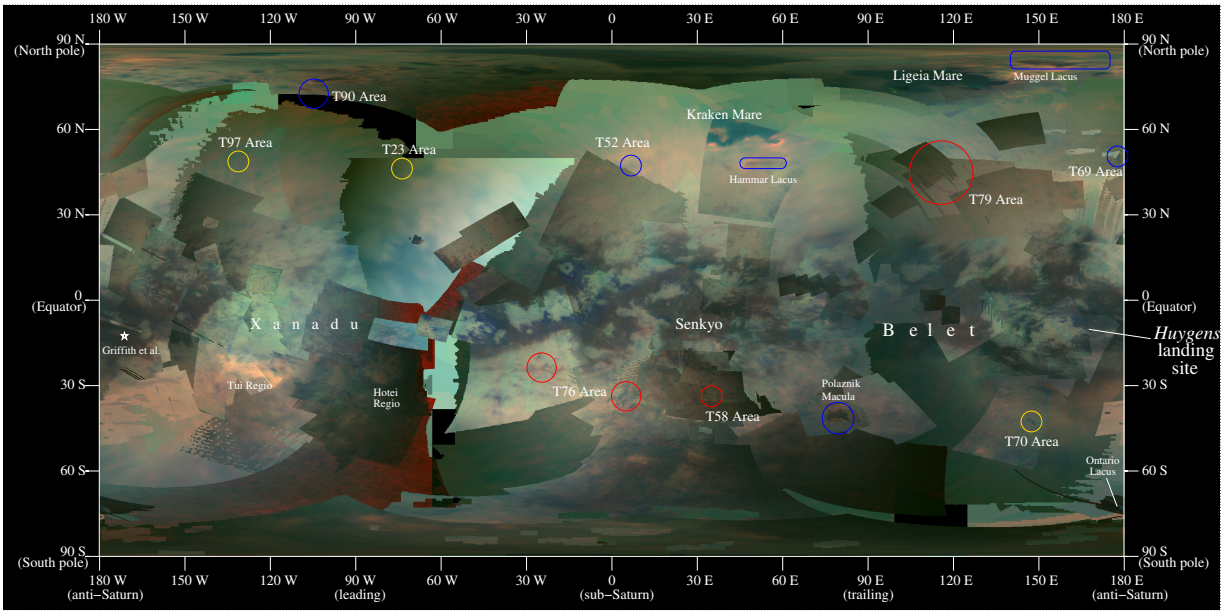

Figure 4.8: We present a global map of Titan made with VIMS data showing the locations of each of our candidates as well as the southern temperate survey performed in Vixie et al. (2014). The candidates are all ranked by color based on their likelihood of being a lake based on our albedo comparison and analysis: blue circles are either already known lakes or candidates we think are most likely lakes; yellow circles are candidates that do not have strong support one way or the other; red circles represent candidates we think are most likely not lakes, either due to albedo or morphology constraints.

Chapter 5

Summary and Conclusions

The *Cassini-Huygens* mission to Saturn and Titan has been very successful in following up observations from the *Voyager* spacecraft, HST (Hubble Space Telescope), and Earth-based telescopes. We now know the composition and photochemistry in Titan's upper atmosphere, researchers have mapped out all of Titan surface regions between VIMS (Visual and Infrared Mapping Spectrometer), ISS (Imaging Science Subsystem), and RADAR instruments, and have further characterized the climate via the clouds, lakes, and dunes. Titan flybys will continue until *Cassini*'s planned collision with Saturn in 2017.

The visible portion of the VIMS instrument shows two small peaks within the visible spectrum at 637 and 681 nm where we may distinguish Titan's surface through its atmosphere. Surface features active in these windows may contribute to surface composition constraints as well as approximating the Bond albedo. The visible wavelengths, when compared to the near-IR, do not provide nearly as much clarity for surface analysis.

Previous to the discovery of Sionascaig Lacus and Urmia Lacus (and one possible equatorial feature), all of the lakes on Titan were located near the poles. The existence of lakes in southern temperate latitudes coincides with clouds appearing in the same regions. We estimate an upper bound of 170 km^3 on the depth of Sionascaig Lacus, which falls within estimates of the total methane inventory of the clouds over the same region (10^{10} – 10^{14} kg), meaning Sionascaig could be completely filled by rainfall or could be driving cloud formation here. Alternatively, Sionascaig is in a moderate-low elevation area according to Lorenz et al. (2013), providing a scenario where percolation via a subsurface reservoir could fill Sionascaig and Urmia.

The question of the longevity of Sionascaig Lacus can be answered by future flybys and would make a great target for VIMS, RADAR, or ISS. Since lakes in the south polar region have been claimed to show temporal variation (Turtle et al., 2009; Hayes et al., 2011), we

may expect to see changes in Sionascaig and Urmia Lacus as well. Variations in southern hemisphere lakes may be indicative of seasonal effects, insolation, or other climate effect and would provide more constraints for GCMs.

Our survey of the northern temperate latitudes identifies three lake candidates. We see no obvious patterns in lake location and no longitudinal dependencies. In comparison to our southern temperate survey, I find more lake candidates in the north fitting with the north pole/south pole dichotomy. Our analysis of the dark, linear virgae show these features are likely not liquid filled based on albedo and size comparisons.

The existence of lakes within the temperate latitudes may mean that the colloquially named "blandlands" are not so bland at higher spatial resolution. While the low contrast of the mid-latitudes already shows a lack of larger features, several smaller regions of interest may be obscured by coarse coverage. Our survey of the temperate latitudes shows all candidate features with a diameter of 140 km or larger.

Many questions still linger for Titan. How much of Titan's climate does seasonal change control? As the seasons move towards winter solstice after the end of the *Cassini* mission, will Titan return to a similar state as when *Cassini* arrived? If *Cassini* or another spacecraft were to monitor clouds and lakes on Titan for the duration of a Titan year, GCMs (Global Circulation Models) could more accurately describe Titan's annual cycle. Are lakes outside the polar regions a result of or contributing factor to the climate? Revisiting Sionascaig Lacus and north temperate candidate locations would show whether these features evaporate quickly, like the rain events previously seen on Titan, or remain and are replenished. The latter case plays into a larger mystery on Titan as to how the lakes were originally formed and filled.

We still do not know how Titan's lakes fill, or replenish in the case of evaporation. *Cassini* has seen several rain events on Titan near the equator and south pole while the north pole remained covered by a hood of clouds for the observable northern winter. More RADAR coverage and stereo imaging to get a better idea of topography and elevation

over lakes especially could bolster the subsurface reservoir idea if all lakes below a certain elevation were filled while those above were not.

While smaller resolution changes and the winter hemisphere may not be visible to Earth-based observations, Titan's cloud activity and atmosphere may still provide insight to the surface with continued monitoring. Any detailed post-*Cassini* observations of Titan are left in the hands of future outer solar system missions. If Titan were monitored over several years, the average observed climate and any longer time scale changes might be constrained. Titan's active liquid cycle and greenhouse gas atmosphere may prove a useful analog to Earth's climate due to each body having similar surface pressure and dynamics with differing surface compositions.

Bibliography

Ádámkovics, M., de Pater, I., Roe, H. G., Gibbard, S. G., & Griffith, C. A. 2004, Geophysical Research Letters, 31, 17

Ádámkovics, M., Wong, M. H., Laver, C., & de Pater, I. 2007, Science, 318, 962

Ádámkovics, M., de Pater, I., Hartung, M., & Barnes, J. W. 2009, Planetary & Space Science, 57, 1586

Ádámkovics, M., Barnes, J. W., Hartung, M., & de Pater, I. 2010, Icarus, 208, 868

Aharonson, O., Hayes, A. G., Lunine, J. I., Lorenz, R. D., Allison, M. D., & Elachi, C. 2009, Nature Geoscience, 2, 851

Atreya, S. K., Adams, E. Y., Niemann, H. B., Demick-Montelara, J. E., Owen, T. C., Fulchignoni, M., Ferri, F., & Wilson, E. H. 2006, Planetary and Space Science, 54, 1177

Bailey, J., Ahlsved, L., & Meadows, V. S. 2011, Icarus, 213, 218

Baines, K. H., Drossart, P., Momary, T. W., Formisano, V., Griffith, C., Bellucci, G., Bibring, J. P., Brown, R. H., Buratti, B. J., Capaccioni, F., Cerroni, P., Clark, R. N., Coradini, A., Combes, M., Cruikshank, D. P., Jaumann, R., Langevin, Y., Matson, D. L., McCord, T. B., Mennella, V., Nelson, R. M., Nicholson, P. D., Sicardy, B., & Sotin, C. 2005, Earth Moon and Planets, 96, 119

Barnes, J. W., Brown, R. H., Turtle, E. P., McEwen, A. S., Lorenz, R. D., Janssen, M., Schaller, E. L., Brown, M. E., Buratti, B. J., Sotin, C., Griffith, C., Clark, R., Perry, J., Fussner, S., Barbara, J., West, R., Elachi, C., Bouchez, A. H., Roe, H. G., Baines, K. H., Bellucci, G., Bibring, J.-P., Capaccioni, F., Cerroni, P., Combes, M., Coradini, A., Cruikshank, D. P., Drossart, P., Formisano, V., Jaumann, R., Langevin, Y., Matson, D. L., McCord, T. B., Nicholson, P. D., & Sicardy, B. 2005, Science, 310, 92

Barnes, J.W., Brown, R.H., Radebaugh, J., Buratti, B.J., Sotin, C., Le Mouelic, S., Rodriguez, S., Turtle, E.P., Perry, J., Clark, R., Baines, K.H., Nicholson, P.D., 2006. Cassini observations of flow-like features in western Tui Regio, Titan. Geophysical Research Letters 33, 16204–+.

Barnes, J. W., Brown, R. H., Soderblom, L., Buratti, B. J., Sotin, C., Rodriguez, S., Le Mouèlic, S., Baines, K. H., Clark, R., & Nicholson, P. 2007, Icarus, 186, 242

Barnes, J. W., Brown, R. H., Soderblom, L., Sotin, C., Le Mouèlic, S., Rodriguez, S., Jaumann, R., Beyer, R. A., Buratti, B. J., Pitman, K., Baines, K. H., Clark, R., & Nicholson, P. 2008, Icarus, 195, 400

Barnes, J. W., Brown, R. H., Soderblom, J. M., Soderblom, L. A., Jaumann, R., Jackson, B., Le Mouélic, S., Sotin, C., Buratti, B. J., Pitman, K. M., Baines, K. H., Clark, R. N., Nicholson, P. D., Turtle, E. P., & Perry, J. 2009a, Icarus, 201, 217

Barnes, J.W., Soderblom, J.M., Brown, R.H., Buratti, B.J., Sotin, C., Baines, K.H., Clark, R.N., Jaumann, R., McCord, T.B., Nelson, R., Le Mouèlic, S., Rodriguez, S., Griffith, C., Penteado, P., Tosi, F., Pitman, K.M., Soderblom, L., Stephan, K., Hayne, P., Vixie, G., Bibring, J., Bellucci, G., Capaccioni, F., Cerroni, P., Coradini, A., Cruikshank, D.P., Drossart, P., Formisano, V., Langevin, Y., Matson, D.L., Nicholson, P.D., Sicardy, B., 2009b. Planetary and Space Science 57, 1950–1962.

Barnes, J. W., Soderblom, J. M., Brown, R. H., Soderblom, L. A., Stephan, K., Jaumann, R., Mouélic, S. L., Rodriguez, S., Sotin, C., Buratti, B. J., Baines, K. H., Clark, R. N., & Nicholson, P. D. 2011a, Icarus, 211, 722

Barnes, J. W., Bow, J., Schwartz, J., Brown, R. H., Soderblom, J. M., Hayes, A. G., Vixie, G., Le Mouélic, S., Rodriguez, S., Sotin, C., Jaumann, R., Stephan, K., Soderblom, L. A., Clark, R. N., Buratti, B. J., Baines, K. H., & Nicholson, P. D. 2011b, Icarus, 216, 136

Barnes, J. W., Buratti, B. J., Turtle, E. P., Bow, J., Dalba, P. A., Perry, J., Brown, R. H., Rodriguez, S., Le Mouèlic, S., Baines, K. H., Sotin, C., Lorenz, R. D., Malaska, M. J., McCord, T. B., Clark, R. N., Jaumann, R., Hayne, P. O., Nicholson, P. D., Soderblom, J. M., & Soderblom, L. A. 2013a, Planetary Science, 2, 1

Barnes, J. W., Clark, R. N., Sotin, C., Ádámkovics, M., Appéré, T., Rodriguez, S., Soderblom, J. M., Brown, R. H., Buratti, B. J., Baines, K. H., Le Mouélic, S., & Nicholson, P. D. 2013b, Astrophysical Journal, 777, 161

Bellucci, A., Sicardy, B., Drossart, P., Rannou, P., Nicholson, P. D., Hedman, M., Baines, K. H., & Burrati, B. 2009, Icarus, 201, 198

Brown, M. E., Bouchez, A. H., & Griffith, C. A. 2002, Nature, 420, 795

Brown, R. H., Baines, K. H., Bellucci, G., Bibring, J.-P., Buratti, B. J., Capaccioni, F., Cerroni, P., Clark, R. N., Coradini, A., Cruikshank, D. P., Drossart, P., Formisano, V., Jaumann, R., Langevin, Y., Matson, D. L., McCord, T. B., Mennella, V., Miller, E., Nelson, R. M., Nicholson, P. D., Sicardy, B., & Sotin, C. 2004, Space Science Reviews, 115, 111

Brown, R. H., Soderblom, L. A., Soderblom, J. M., Clark, R. N., Jaumann, R., Barnes, J. W., Sotin, C., Buratti, B., Baines, K. H., & Nicholson, P. D. 2008, Nature, 454, 607

Brown, M. E., Roberts, J. E., & Schaller, E. L. 2010, Icarus, 205, 571

Capaccioni, F., Coradini, A., Cerroni, P., Amici, S., 1998. Planetary and Space Science 46, 1263–1276.

Clark, R. N., Curchin, J. M., Barnes, J. W., Jaumann, R., Soderblom, L., Cruikshank, D. P., Brown, R. H., Rodriguez, S., Lunine, J., Stephan, K., Hoefen, T. M., Le Mouélic, S., Sotin, C., Baines, K. H., Buratti, B. J., & Nicholson, P. D. 2010, Journal of Geophysical Research (Planets), 115, 10005

Combe, J.-P., McCord, T. B., Hayne, P., & Hansen, G. B. 2007, in Bulletin of the American Astronomical Society, Vol. 39, AAS/Division for Planetary Sciences Meeting Abstracts #39, 500

Cornet, T., Bourgeois, O., Le Mouélic, S., Rodriguez, S., Lopez Gonzalez, T., Sotin, C., Tobie, G., Fleurant, C., Barnes, J. W., Brown, R. H., Baines, K. H., Buratti, B. J., Clark, R. N., & Nicholson, P. D. 2012a, Icarus, 218, 788

Cornet, T., Bourgeois, O., Le Mouélic, S., Rodriguez, S., Sotin, C., Barnes, J. W., Brown, R. H., Baines, K. H., Buratti, B. J., Clark, R. N., & Nicholson, P. D. 2012b, Journal of Geophysical Research (Planets), 117, 7005

Cours, T., Burgalat, J., Rannou, P., Rodriguez, S., Brahic, A., & West, R. A. 2011, Astrophysical Journal Letters, 741, L32

Cours, T., Rannou, P., Coustenis, A., & Hamdouni, A. 2010, Planetary & Space Science, 58, 1708

Coustenis, A., Negrão, A., Salama, A., Schulz, B., Lellouch, E., Rannou, P., Drossart, P., Encrenaz, T., Schmitt, B., Boudon, V., & Nikitin, A. 2006, Icarus, 180, 176

de Bergh, C., Courtin, R., Bézard, B., Coustenis, A., Lellouch, E., Hirtzig, M., Rannou, P., Drossart, P., Campargue, A., Kassi, S., Wang, L., Boudon, V., Nikitin, A., & Tyuterev, V. 2012, Planetary & Space Science, 61, 85

Dermott, S. F. & Sagan, C. 1995, Nature, 374, 238

Elachi, C., Allison, M. D., Borgarelli, L., Encrenaz, P., Im, E., Janssen, M. A., Johnson, W. T. K., Kirk, R. L., Lorenz, R. D., Lunine, J. I., Muhleman, D. O., Ostro, S. J., Picardi, G., Posa, F., Rapley, C. G., Roth, L. E., Seu, R., Soderblom, L. A., Vetrella, S., Wall, S. D., Wood, C. A., & Zebker, H. A. 2004, Space Science Reviews, 115, 71

Elachi, C., Wall, S., Allison, M., Anderson, Y., Boehmer, R., Callahan, P., Encrenaz, P., Flamini, E., Franceschetti, G., Gim, Y., Hamilton, G., Hensley, S., Janssen, M., Johnson, W., Kelleher, K., Kirk, R., Lopes, R., Lorenz, R., Lunine, J., Muhleman, D., Ostro, S., Paganelli, F., Picardi, G., Posa, F., Roth, L., Seu, R., Shaffer, S., Soderblom, L., Stiles, B., Stofan, E., Vetrella, S., West, R., Wood, C., Wye, L., & Zebker, H. 2005, Science, 308, 970

Eshleman, V. R., Lindal, G. F., & Tyler, G. L. 1983, Science, 221, 53

Flasar, F. M. 1983, Science, 221, 55

Fussner, S. 2006, MS Thesis, The University of Arizona, Arizona, USA

Griffith, C. A., Owen, T., & Wagener, R. 1991, Icarus, 93, 362

Griffith, C. A., Owen, T., Miller, G. A., & Geballe, T. 1998, Nature, 395, 575

Griffith, C. A., Owen, T., Geballe, T. R., Rayner, J., & Rannou, P. 2003, Science, 300, 628

Griffith, C. A., Penteado, P., Baines, K., Drossart, P., Barnes, J., Bellucci, G., Bibring, J., Brown, R., Buratti, B., Capaccioni, F., Cerroni, P., Clark, R., Combes, M., Coradini, A., Cruikshank, D., Formisano, V., Jaumann, R., Langevin, Y., Matson, D., McCord, T., Mennella, V., Nelson, R., Nicholson, P., Sicardy, B., Sotin, C., Soderblom, L. A., & Kursinski, R. 2005, Science, 310, 474

Griffith, C. A., Penteado, P., Rannou, P., Brown, R., Boudon, V., Baines, K. H., Clark, R., Drossart, P., Buratti, B., Nicholson, P., McKay, C. P., Coustenis, A., Negrao, A., & Jaumann, R. 2006, Science, 313, 1620

Griffith, C. A., Doose, L., Tomasko, M. G., Penteado, P. F., & See, C. 2012a, Icarus, 218, 975

Griffith, C. A., Lora, J. M., Turner, J., Penteado, P. F., Brown, R. H., Tomasko, M. G., Doose, L., & See, C. 2012b, Nature, 486, 237

Hayes, A., Aharonson, O., Callahan, P., Elachi, C., Gim, Y., Kirk, R., Lewis, K., Lopes, R., Lorenz, R., Lunine, J., Mitchell, K., Mitri, G., Stofan, E., & Wall, S. 2008, Geophysical Research Letters, 35, 9204

Hayes, A. G., Wolf, A. S., Aharonson, O., Zebker, H., Lorenz, R., Kirk, R. L., Paillou, P., Lunine, J., Wye, L., Callahan, P., Wall, S., & Elachi, C. 2010, Journal of Geophysical Research (Planets), 115, 9009

Hayes, A. G., Aharonson, O., Lunine, J. I., Kirk, R. L., Zebker, H. A., Wye, L. C., Lorenz, R. D., Turtle, E. P., Paillou, P., Mitri, G., Wall, S. D., Stofan, E. R., Mitchell, K. L., Elachi, C., & Cassini Radar Team. 2011, Icarus, 211, 655

Hayes, A. G., Dietrich, W. E., Kirk, R. L., Turtle, E. P., Barnes, J. W., Lucas, A., Aharonson, O., & Mitchell, K. L. 2013, LPI Contributions, 1719, 2000

Hirtzig, M., Bézard, B., Lellouch, E., Coustenis, A., deBergh, C., Drossart, P., Campargue, A., Boudon, V., Tyuterev, V., Rannou, P., Cours, T., Kassi, S., Nikitin, A., Mondelain, D., Rodriguez, S., & Le Mouélic, S. 2013, Icarus, In Press

Huygens C. 1655

Karkoschka, E., 1994. Icarus, September 111, 174-192

Keller, H. U., Grieger, B., Küppers, M., Schröder, S. E., Skorov, Y. V., & Tomasko, M. G. 2008, Planetary & Space Science, 56, 728

Langhans, M. H., Jaumann, R., Stephan, K., Brown, R. H., Buratti, B. J., Clark, R. N., Baines, K. H., Nicholson, P. D., Lorenz, R. D., Soderblom, L. A., Soderblom, J. M., Sotin, C., Barnes, J. W., & Nelson, R. 2012, Planetary and Space Science, 60, 34

Le Gall, A., Janssen, M. A., Wye, L. C., Hayes, A. G., Radebaugh, J., Savage, C., Zebker, H., Lorenz, R. D., Lunine, J. I., Kirk, R. L., Lopes, R. M. C., Wall, S., Callahan, P., Stofan, E. R., Farr, T., & Cassini RADAR Team 2011, Icarus, 213, 608

Le Gall, A., Hayes, A. G., Ewing, R., Janssen, M. A., Radebaugh, J., Savage, C., Encrenaz, P., & Cassini RADAR Team. 2012, Icarus, 217, 231

Le Mouélic, S., Paillou, P., Janssen, M.A., Barnes, J.W., Rodriguez, S., Sotin, C., Brown, R.H., Baines, K.H., Buratti, B.J., Clark, R.N., Crapeau, M., Encrenaz, P.J., Jaumann, R., Geudtner, D., Paganelli, F., Soderblom, L., Tobie, G., Wall, S., 2008. Journal of Geophysical Research 113, 4003–+.

Le Mouélic, S., Rannou, P., Rodriguez, S., Sotin, C., Griffith, C. A., Le Corre, L., Barnes, J. W., Brown, R. H., Baines, K. H., Buratti, B. J., Clark, R. N., Nicholson, P. D., & Tobie, G. 2012a, Planetary and Space Science, 60, 86

Le Mouélic, S., Cornet, T., Rodriguez, S., Sotin, C., Barnes, J. W., Baines, K. H., Brown, R. H., Lefèvre, A., Buratti, B. J., Clark, R. N., & Nicholson, P. D. 2012b, Planetary & Space Science, 73, 178

Lemmon, M. T., Smith, P. H., Lorenz, R. D., 2002. Icarus, December, 160, 375–385.

Lockwood, G. W., Lutz, B. L., Thompson, D. T., Bus, E. S.. 1986. Astrophysical Journal, April, 303, 511–520.

Lora, J. M., Lunine, J. I., Russell, J. L., & Hayes, A. G. 2014, in Titan Through Time; Unlocking Titan's Past, Present and Future, ed. C. Nixon & R. Lorenz

Lorenz, R. D. 1994, Planetary & Space Science, 42, 1

Lorenz, R. D. & Lunine, J. I. 2005, Planetary and Space Science, 53, 557

Lorenz, R. D., Wall, S., Radebaugh, J., Boubin, G., Reffet, E., Janssen, M., Stofan, E., Lopes, R., Kirk, R., Elachi, C., Lunine, J., Mitchell, K., Paganelli, F., Soderblom,

L., Wood, C., Wye, L., Zebker, H., Anderson, Y., Ostro, S., Allison, M., Boehmer, R., Callahan, P., Encrenaz, P., Ori, G. G., Francescetti, G., Gim, Y., Hamilton, G., Hensley, S., Johnson, W., Kelleher, K., Muhleman, D., Picardi, G., Posa, F., Roth, L., Seu, R., Shaffer, S., Stiles, B., Vetrella, S., Flamini, E., & West, R. 2006, Science, 312, 724

Lorenz, R. D. & Radebaugh, J. 2009, Geophysical Research Letters, 36, 3202

Lorenz, R. D., Turtle, E. P., Stiles, B., Le Gall, A., Hayes, A., Aharonson, O., Wood, C. A., Stofan, E., & Kirk, R. 2011, Icarus, 211, 699

Lorenz, R. D., Stiles, B. W., Aharonson, O., Lucas, A., Hayes, A. G., Kirk, R. L., Zebker, H. A., Turtle, E. P., Neish, C. D., Stofan, E. R., & Barnes, J. W. 2013, Icarus, 225, 367

Lunine, J. I., Stevenson, D. J., & Yung, Y. L. 1983, Science, 222, 1229

Luspay-Kuti, A., Chevrier, V. F., Singh, S., Rivera-Valentin, E. G., Wagner, A., & Wasiak, F. C. 2014, in Lunar and Planetary Science Conference, Vol. 45, Lunar and Planetary Science Conference, 1882

MacKenzie, S., Barnes, J. W., Sotin, C., Le Mouelic, S., Rodriguez, S. R., Baines, Buratti, B. J., Clark, K. H., Nicholson, P. D., & McCord, T. 2014, Icarus, Submitted

McCord, T. B., Hayne, P., Combe, J.-P., Hansen, G. B., Barnes, J. W., Rodriguez, S., Le Mouélic, S., Baines, E. K. H., Buratti, B. J., Sotin, C., Nicholson, P., Jaumann, R., Nelson, R., & The Cassini Vims Team. 2008, Icarus, 194, 212

McKay, C.P., Pollack, J.B., Courtin, R., 1989a. Icarus 80, 23–53.

McKay, C. P., Pollack, J. B., Zent, A. P., Cruikshank, D. P., & Courtin, R. 1989b, Geophysical Research Letters, 16, 973

Mitri, G., Showman, A. P., Lunine, J. I., & Lorenz, R. D. 2007, Icarus, 186, 385

Neff, J. S., Humm, D. C., Bergstralh, J. T., Cochran, A. L., Cochran, W. D., Barker, E. S., Tull, R. G., 1984. Icarus, November, 60, 221–235.

Paillou, P., Mitchell, K., Wall, S., Ruffié, G., Wood, C., Lorenz, R., Stofan, E., Lunine, J., Lopes, R., & Encrenaz, P. 2008, Geophysical Research Letters, 35, 5202

Perry, J.E., McEwen, A.S., Fussner, S., Turtle, E.P., West, R.A., Porco, C.C., Knowles, B., Dawson, D.D., The Cassini Iss Team, 2005. S. Mackwell & E. Stansbery (Ed.), 36th Annual Lunar and Planetary Science Conference, pp. 2312–+.

Porco, C. C., West, R. A., Squyres, S., McEwen, A., Thomas, P., Murray, C. D., Delgenio, A., Ingersoll, A. P., Johnson, T. V., Neukum, G., Veverka, J., Dones, L., Brahic, A., Burns, J. A., Haemmerle, V., Knowles, B., Dawson, D., Roatsch, T., Beurle, K., & Owen, W. 2004, Space Science Reviews, 115, 363

Porco, C.C., Baker, E., Barbara, J., Beurle, K., Brahic, A., Burns, J.A., Charnoz, S., Cooper, N., Dawson, D.D., Del Genio, A.D., Denk, T., Dones, L., Dyudina, U., Evans, M.W., Fussner, S., Giese, B., Grazier, K., Helfenstein, P., Ingersoll, A.P., Jacobson, R.A., Johnson, T.V., McEwen, A., Murray, C.D., Neukum, G., Owen, W.M., Perry, J., Roatsch, T., Spitale, J., Squyres, S., Thomas, P., Tiscareno, M., Turtle, E.P., Vasavada, A.R., Veverka, J., Wagner, R., West, R., 2005. Nature 434, 159–168.

Radebaugh, J., Lorenz, R. D., Lunine, J. I., Wall, S. D., Boubin, G., Reffet, E., Kirk, R. L., Lopes, R. M., Stofan, E. R., Soderblom, L., Allison, M., Janssen, M., Paillou, P., Callahan, P., Spencer, C., & the Cassini Radar Team. 2008, Icarus, 194, 690

Radebaugh, J., Lorenz, R. D., Lunine, J. I., Kirk, R. L., Ori, G. G., Farr, T. G., Malaska, M., Le Gall, A., Liu, Z. Y. C., Encrenaz, P. J., Paillou, P., Hayes, A., Lopes, R. M. C., Turtle, E. P., Wall, S. D., Stofan, E. R., Wood, C. A., & Cassini RADAR Team. 2012, in AAS/Division for Planetary Sciences Meeting Abstracts, Vol. 44, AAS/Division for Planetary Sciences Meeting Abstracts, #201.07

Rannou, P., Cabane, M., Chassefiere, E., Botet, R., McKay, C. P., & Courtin, R. 1995, Icarus, 118, 355

Rannou, P., Cabane, M., Botet, R., & Chassefière, E. 1997, Journal of Geophysical Research, 102, 10997

Rannou, P., McKay, C. P., Botet, R., & Cabane, M. 1999, Planetary & Space Science, 47, 385

Rannou, P., Ferrari, C., Rages, K., Roos-Serote, M., & Cabane, M. 2000, Icarus, 147, 267

Rannou, P., McKay, C. P., & Lorenz, R. D. 2003, Planetary & Space Science, 51, 963

Rannou, P., Montmessin, F., Hourdin, F., & Lebonnois, S. 2006, Science, 311, 201

Rannou, P., Cours, T., Le Mouélic, S., Rodriguez, S., Sotin, C., Drossart, P., & Brown, R. 2010, Icarus, 208, 850

Rannou, P., Le Mouélic, S., Sotin, C., & Brown, R. H. 2012, Astrophysical Journal, 748, 4

Richardson, J., Lorenz, R. D., & McEwen, A. 2004, Icarus, 170, 113

Rodriguez, S., Le Mouélic, S., Sotin, C., Clénet, H., Clark, R. N., Buratti, B., Brown, R. H., McCord, T. B., Nicholson, P. D., Baines, K. H., & the VIMS Science Team. 2006, Planetary & Space Science, 54, 1510

Rodriguez, S., Le Mouélic, S., Rannou, P., Tobie, G., Baines, K. H., Barnes, J. W., Griffith, C. A., Hirtzig, M., Pitman, K. M., Sotin, C., Brown, R. H., Buratti, B. J., Clark, R. N., & Nicholson, P. D. 2009, Nature, 459, 678

Rodriguez, S., Le Mouélic, S., Rannou, P., Sotin, C., Brown, R. H., Barnes, J. W., Griffith, C. A., Burgalat, J., Baines, K. H., Buratti, B. J., Clark, R. N., & Nicholson, P. D. 2011, Icarus, 216, 89

Rodriguez, S., Le Mouélic, S., Barnes, J. W., Hirtzig, M., Rannou, P., Sotin, C., Brown, R. H., Bow, J., Vixie, G., Cornet, T., Bourgeois, O., Narteau, C., Courrech du Pont, S., Le Gall, A., Reffet, E., Griffith, C. A., Jaumann, R., Stephan, K., Buratti, B. J., Clark, R. N., Baines, K. H., Nicholson, P. D., & Coustenis, A. 2013, Icarus, In Press

Rodriguez, S., Garcia, A., Lucas, A., Appéré, T., Le Gall, A., Reffet, E., Le Corre, L., Le Mouélic, S., Cornet, T., Courrech du Pont, S., Narteau, C., Bourgeois, O., Radebaugh, J., Arnold, K., Barnes, J. W., Stephan, K., Jaumann, R., Sotin, C., Brown, R. H., Lorenz, R. D., & Turtle, E. P. 2014, Icarus, 230, 168

Roe, H. G., de Pater, I., Macintosh, B. A., & McKay, C. P. 2002, Astrophysical Journal, 581, 1399

Roe, H. G., Bouchez, A. H., Trujillo, C. A., Schaller, E. L., & Brown, M. E. 2005a, Astrophysical Journal Letters, 618, L49

Roe, H. G., Brown, M. E., Schaller, E. L., Bouchez, A. H., & Trujillo, C. A. 2005b, Science, 310, 477

Sagan, C. & Dermott, S. F. 1982, Nature, 300, 731

Schröder, S. E. & Keller, H. U. 2008, Planetary & Space Science, 56, 753

Schröder, S. E. & Keller, H. U. 2009, Planetary & Space Science, 57, 1963

Smith, P.H., Lemmon, M.T., Lorenz, R.D., Sromovsky, L.A., Caldwell, J.J., Allison, M.D., 1996. Icarus 119, 336–349.

Soderblom, J. M., Barnes, J. W., Soderblom, L. A., Brown, R. H., Griffith, C. A., Nicholson, P. D., Stephan, K., Jaumann, R., Sotin, C., Baines, K. H., Buratti, B. J., & Clark, R. N. 2012, Icarus, 220, 744

Soderblom, L. A., Kirk, R. L., Lunine, J. I., Anderson, J. A., Baines, K. H., Barnes, J. W., Barrett, J. M., Brown, R. H., Buratti, B. J., Clark, R. N., Cruikshank, D. P., Elachi,

C., Janssen, M. A., Jaumann, R., Karkoschka, E., Mouélic, S. L., Lopes, R. M., Lorenz, R. D., McCord, T. B., Nicholson, P. D., Radebaugh, J., Rizk, B., Sotin, C., Stofan, E. R., Sucharski, T. L., Tomasko, M. G., & Wall, S. D. 2007, Planetary and Space Science, 55, 2025

Soderblom, L.A., Brown, R.H., Soderblom, J.M., Barnes, J.W., Kirk, R.L., Sotin, C., Jaumann, R., MacKinnon, D.J., Mackowski, D.W., Baines, K.H., Buratti, B.J., Clark, R.N., Nicholson, P.D., 2009. Icarus 204, 610–618.

Sotin, C., Lawrence, K. J., Reinhardt, B., Barnes, J. W., Brown, R. H., Hayes, A. G., Le Mouélic, S., Rodriguez, S., Soderblom, J. M., Soderblom, L. A., Baines, K. H., Buratti, B. J., Clark, R. N., Jaumann, R., Nicholson, P. D., & Stephan, K. 2012, Icarus, 221, 768

Stephan, K., Jaumann, R., Karkoschka, E., Barnes, J.W., Kirk, R., Tomasko, M.G., Turtle, E.P., Le Corre, L., Langshans, M., Le Mouèlic, S., Lorenz, R., Perry, J., 2009. R. H. Brown and J. Lebreton and J. H. Waite (Ed.), Titan from Cassini-Huygens, pp. 489–510.

Stephan, K., Jaumann, R., Brown, R. H., Soderblom, J. M., Soderblom, L. A., Barnes, J. W., Sotin, C., Griffith, C. A., Kirk, R. L., Baines, K. H., Buratti, B. J., Clark, R. N., Lytle, D. M., Nelson, R. M., & Nicholson, P. D. 2010, Geophysical Research Letters, 37, 7104

Stofan, E. R., Lunine, J. I., Lopes, R., Paganelli, F., Lorenz, R. D., Wood, C. A., Kirk, R., Wall, S., Elachi, C., Soderblom, L. A., Ostro, S., Janssen, M., Radebaugh, J., Wye, L., Zebker, H., Anderson, Y., Allison, M., Boehmer, R., Callahan, P., Encrenaz, P., Flamini, E., Francescetti, G., Gim, Y., Hamilton, G., Hensley, S., Johnson, W. T. K., Kelleher, K., Muhleman, D., Picardi, G., Posa, F., Roth, L., Seu, R., Shaffer, S., Stiles, B., Vetrella, S., & West, R. 2006, Icarus, 185, 443

Stofan, E. R., Elachi, C., Lunine, J. I., Lorenz, R. D., Stiles, B., Mitchell, K. L., Ostro, S., Soderblom, L., Wood, C., Zebker, H., Wall, S., Janssen, M., Kirk, R., Lopes, R., Paganelli, F., Radebaugh, J., Wye, L., Anderson, Y., Allison, M., Boehmer, R., Callahan, P., Encrenaz, P., Flamini, E., Francescetti, G., Gim, Y., Hamilton, G., Hensley, S., Johnson, W. T. K., Kelleher, K., Muhleman, D., Paillou, P., Picardi, G., Posa, F., Roth, L., Seu, R., Shaffer, S., Vetrella, S., & West, R. 2007, Nature, 445, 61

Thompson, W. R. & Sagan, C. 1984, Icarus, 60, 236

Tokano, T. 2009, Icarus, 204, 619

Tomasko, M. G., Buchhauser, D., Bushroe, M., Dafoe, L. E., Doose, L. R., Eibl, A., Fellows, C., Farlane, E. M., Prout, G. M., Pringle, M. J., Rizk, B., See, C., Smith, P. H., & Tsetsenekos, K. 2002, Space Science Reviews, 104, 467

Tomasko, M. G., Archinal, B., Becker, T., Bézard, B., Bushroe, M., Combes, M., Cook, D., Coustenis, A., de Bergh, C., Dafoe, L. E., Doose, L., Douté, S., Eibl, A., Engel, S., Gliem, F., Grieger, B., Holso, K., Howington-Kraus, E., Karkoschka, E., Keller, H. U., Kirk, R., Kramm, R., Küppers, M., Lanagan, P., Lellouch, E., Lemmon, M., Lunine, J., McFarlane, E., Moores, J., Prout, G. M., Rizk, B., Rosiek, M., Rueffer, P., Schröder, S. E., Schmitt, B., See, C., Smith, P., Soderblom, L., Thomas, N., & West, R. 2005, Nature, 438, 765

Tomasko, M. G., Bézard, B., Doose, L., Engel, S., & Karkoschka, E. 2008a, Planetary & Space Science, 56, 624

Tomasko, M. G., Doose, L., Engel, S., Dafoe, L. E., West, R., Lemmon, M., Karkoschka, E., & See, C. 2008b, Planetary & Space Science, 56, 669

Toon, O. B., McKay, C. P., Courtin, R., & Ackerman, T. P. 1988, Icarus, 75, 255

Turtle, E. P., Perry, J. E., McEwen, A. S., Del Genio, A. D., Barbara, J., West, R. A., Dawson, D. D., & Porco, C. C. 2009, Geophysical Research Letters, 36, L02204

Turtle, E. P., Del Genio, A. D., Barbara, J. M., Perry, J. E., Schaller, E. L., McEwen, A. S., West, R. A., & Ray, T. L. 2011a, Geophysical Research Letters, 38, 3203

Turtle, E. P., Perry, J. E., Hayes, A. G., Lorenz, R. D., Barnes, J. W., McEwen, A. S., West, R. A., Del Genio, A. D., Barbara, J. M., Lunine, J. I., Schaller, E. L., Ray, T. L., Lopes, R. M. C., & Stofan, E. R. 2011b, Science, 331, 1414

Turtle, E. P., Perry, J. E., Hayes, A. G., & McEwen, A. S. 2011c, Icarus, 212, 957

Tyler, G. L., Eshleman, V. R., Anderson, J. D., Levy, G. S., Lindal, G. F., Wood, G. E., & Croft, T. A. 1981, Science, 212, 201

Vincendon, M. & Langevin, Y. 2010, Icarus, 207, 923

Vixie, G., Barnes, J. W., Jackson, B., Rodriguez, S., Le Mouélic, S., Sotin, C., & Wilson, P. 2014, Icarus, Submitted

Wall, S., Hayes, A., Bristow, C., Lorenz, R., Stofan, E., Lunine, J., Le Gall, A., Janssen, M., Lopes, R., Wye, L., Soderblom, L., Paillou, P., Aharonson, O., Zebker, H., Farr, T., Mitri, G., Kirk, R., Mitchell, K., Notarnicola, C., Casarano, D., & Ventura, B. 2010, Geophysical Research Letters, 37, 5202

Wye, L. C., Zebker, H. A., & Lorenz, R. D. 2009, Geophysical Research Letters, 36, 16201

Young, E. F., Rannou, P., McKay, C. P., Griffith, C. A., & Noll, K. 2002, Astronomical Journal, 123, 3473